

Molecular Dynamics Investigations of Clusters and Solids

Vom Fachbereich Chemie
der Universität Hannover
zur Erlangung des Grades

Doktor der Naturwissenschaften

Dr. rer. nat.
genehmigte Dissertation
von

M.Sc. Nisanth N. Nair

geboren am 05.05.1979
in Kallara, Kerala, Indien

2004

Referent: Prof. Dr. K. Jug
Theoretische Chemie, Universität Hannover
Am Kleinen Felde 30, 30167 Hannover

Korreferent: Priv.-Doz. Dr. T. Bredow
Theoretische Chemie, Universität Hannover
Am Kleinen Felde 30, 30167 Hannover

Tag der Promotion: 20.12.2004

I am grateful to Prof. Dr. K. Jug for giving me an opportunity to work in his research group. I thank him for his enthusiastic guidance and enlightening discussion.

I am obliged to Priv.-Doz. Dr. T. Bredow for his invaluable help and for being a constant source of motivation throughout the work.

I thank all my colleagues for their help and encouragement.

I am thankful to Prof. Dr. Parrinello, ETH Zürich, for his gracious hospitality and Dr. M. Krack, ETH Zürich, for his motivation and fruitful discussion.

I thank for a Georg-Lichtenberg fellowship provided by the state of Niedersachsen.

Abstract

The Born-Oppenheimer molecular dynamics (MD) technique has been implemented in the semiempirical self consistent field molecular orbital method MSINDO. With MD in conjunction with MSINDO it is possible to study large systems in the picosecond time scale. Results of simulated annealing of Si_n ($n = 5 - 7$) clusters are presented to demonstrate the reliability of the present parameters for silicon compounds. Structural changes of a Si_7 cluster at high temperatures are investigated. Energy minimum structures of Si_{45} and Si_{60} clusters are obtained by extensive simulated annealing. The stabilities of various structures are compared with available literature data. The MSINDO-MD implementation is combined with the cyclic cluster model (CCM) in order to investigate complex solid state problems. To understand the structure of the vanadia-titania catalysts, which are important in the partial oxidation of hydrocarbons and the selective catalytic reduction of nitric oxides with NH_3 to N_2 , reactions between hydrated vanadia species with various TiO_2 anatase surfaces are analyzed. The reaction of the surface hydroxyl groups with the adsorbed vanadia species is also investigated. Oxygen vacancy diffusion from the (110) surface to the bulk of rutile is simulated and the activation barriers for the diffusion processes are estimated. In addition, the adsorption of water in monolayer and double layer coverages on the rutile (110) and (100) surfaces is analyzed and the vibrational density of states is obtained. The results are compared with available literature data. MSINDO-MD is used for estimating the thermodynamic properties of zinc chalcogenides. The thermal-entropic contributions to the free energy of mixing for $\text{ZnO}_{1-x}\text{S}_x$ systems are evaluated.

Keywords: anatase, cyclic cluster model, metal oxides, molecular dynamics, MSINDO, rutile, semiempirical method, silicon clusters, titanium dioxide, zinc oxide, zinc sulphide

Kurzzusammenfassung

Die Born-Oppenheimer Molekulardynamik (MD) wird in der semiempirischen Molekülorbitalmethode MSINDO implementiert. Die Kombination von MD mit MSINDO erlaubt die Betrachtung großer Systeme im Pikosekundenbereich. Ergebnisse mit der Technik der simulierten Abkühlung (simulated annealing) an Si_n -Clustern ($n = 5 - 7$) werden präsentiert, um die Verlässlichkeit der Parameter für Siliciumverbindungen zu demonstrieren. Für einen Si_7 -Cluster werden Strukturänderungen bei hohen Temperaturen untersucht. Durch umfangreiche simulierte Abkühlung werden die Energieminimumstrukturen von Si_{45} - und Si_{60} -Clustern ermittelt. Die Stabilitäten verschiedener Strukturen werden mit verfügbaren Daten aus der Literatur verglichen. Zur Untersuchung komplexer Probleme in der Festkörperchemie wird die MSINDO-MD Implementierung mit dem zyklischen Clustermodell (CCM) kombiniert. Zum Verständnis der Struktur von V_2O_5 /Anatas-Katalysatoren, die eine wichtige Rolle bei der partiellen Oxidation von Kohlenwasserstoffen und der selektiven katalytischen Reduktion von NO mit NH_3 zu N_2 spielen, werden Reaktionen zwischen hydratisierten VO_x -Spezies mit verschiedenen Anatasoberflächen analysiert. Ferner ist auch der Einfluß von Oberflächenhydroxylgruppen auf die Struktur des adsorbierten VO_x Gegenstand dieser Arbeit. Die Diffusion von Sauerstoffleerstellen von der (110)-Oberfläche in den Rutil-Festkörper wird simuliert und die Aktivierungsenergien für diesen Diffusionsprozeß berechnet. Darüberhinaus erfolgt eine Untersuchung der Monolagen- und Doppellagenadsorption von Wasser auf Rutil (110) und (100). Die vibronische Zustandsdichte wird berechnet und mit der Literatur verglichen. MSINDO-MD wird zur Berechnung thermodynamischer Eigenschaften von Zinkchalkogeniden verwendet. Hierbei werden die thermischen Entropiebeiträge zur freien Energie der Mischung von $\text{ZnO}_{1-x}\text{S}_x$ -Systemen bestimmt.

Keywords: Anatas, zyklisches Clustermodell, Metalloxide, Molekulardynamik, MSINDO, Rutil, semiempirische Methode, Silizium-Cluster, Titansioxid, Zinkoxid, Zinksulfid

Contents

1	Introduction	1
2	Quantum Chemical Methods and Models	3
2.1	The Hartree-Fock Approximation	4
2.2	The Semiempirical Method MSINDO	8
2.3	Cyclic Cluster Model	11
3	Molecular Dynamics	15
3.1	Fundamentals	15
3.1.1	Equations of Motion	15
3.1.2	Types of Molecular Dynamics	16
3.1.3	Integration of the Equations of Motion	17
3.1.4	Property Calculation with Molecular Dynamics	18
3.1.5	Controlling Temperature in Molecular Dynamics	23
3.1.6	Simulated Annealing	23
3.2	Advanced Methods	24
3.2.1	Nosé-Hoover Chain Thermostats	24
3.2.2	Metadynamics	26
4	Implementation of Molecular Dynamics in MSINDO	29
4.1	Algorithm for Born-Oppenheimer Molecular Dynamics	29
4.2	Test Calculations	32
4.2.1	Total Energy Conservation	32
4.2.2	Simulated Annealing of Simple Molecules	33
4.2.3	Canonical Ensemble Simulation using the Nosé-Hoover Chain Thermostat	34
4.2.4	Exploration of Free Energy Surface using Metadynamics	35
5	Applications of Molecular Dynamics Techniques	38
5.1	Structure and Melting Behavior of Silicon Clusters	38
5.1.1	Introduction	38
5.1.2	Simple Silicon Clusters	39

5.1.3	Solid-Liquid Transition of the Si ₇ Cluster	42
5.1.4	Simulated Annealing of Medium Size Silicon Clusters	46
5.2	Formation of Vanadia-Titania Catalysts	52
5.2.1	Introduction	52
5.2.2	Bulk Properties of Anatase	54
5.2.3	Surface Properties of Anatase	55
5.2.4	Models of VO _x /TiO ₂ Catalysts	59
5.2.5	Adsorption of VO ₄ H ₃ on Anatase Surfaces	60
5.2.6	Adsorption of V ₂ O ₇ H ₄ on Anatase Surfaces	67
5.2.7	Reaction of the Surface Hydroxyl Groups with VO ₄ H ₃	73
5.3	Oxygen Vacancy Diffusion in Rutile	80
5.3.1	Introduction	80
5.3.2	Bulk Properties of Rutile	81
5.3.3	Surface Properties of Rutile	83
5.3.4	Diffusion of Surface Oxygen Vacancy	86
5.4	Water Adsorption on Rutile Surfaces	95
5.4.1	Introduction	95
5.4.2	Models	96
5.4.3	Adsorption of an Isolated Water Molecule	97
5.4.4	Monolayer Water Coverage	98
5.4.5	Double Layer Water Coverage	107
5.5	Mixing of Zinc Oxide and Zinc Sulfide	114
5.5.1	Introduction	114
5.5.2	Bulk Properties	115
5.5.3	Entropy and Free Energy of Mixing	116
6	Summary	121
A	Analytical Derivatives of Collective Coordinates	125
	References	130

1 Introduction

Molecular dynamics (MD) is a suitable method for generating classical trajectories [1]. MD simulations using empirical potentials can treat large systems via long trajectories, because the estimate of forces and energies is computationally inexpensive. But it is difficult to describe situations like bond formation, bond breaking and charge transfer during the dynamics by such predefined potentials. Parametrization of model potentials and their accuracy is always a problem with these methods. Quantum chemical MD simulations consider the motion of the nuclei on a Born-Oppenheimer surface. Because the electronic structure calculation has to be performed along the trajectory, such an approach is computationally expensive for high-level quantum chemical methods. The semiempirical molecular orbital method MSINDO [2] is computationally faster than high-level methods in evaluating the forces and energies. Thus MD simulations using MSINDO can be used to generate classical trajectories of large and complex systems for picosecond time scales.

MD techniques are implemented in MSINDO. Details of the implementation are presented. Different parts of the MSINDO-MD procedure are explicitly tested.

MD techniques are widely used to explore the free energy hypersurface, to study melting and diffusion processes, to estimate the vibrational density of states and to calculate thermodynamic properties of a system. All these applications of MD techniques are performed using MSINDO.

Structure and melting behaviour of silicon clusters are studied using MSINDO-MD. Global minimum structures of medium size silicon clusters are extremely difficult to determine due to their complex potential energy surface. Traditional optimization methods will fail to find the global minimum structure as they generally find the minimum closest to the starting structure. Simulated annealing, which is a particular application of MD approach, is a way to overcome the energy barriers. To demonstrate the accuracy of the present parameters for silicon compounds, the energy minimum structures of Si_n ($n = 5 - 7$) clusters are calculated using the simulated annealing technique and the results are compared with the literature. The melting behavior of the Si_7 cluster is also studied using MSINDO-MD. With the simulated annealing technique, energy minimum structures of Si_{45} and Si_{60} clusters are determined.

Vanadia-titania catalysts are used in the selective catalytic reduction reaction of nitric oxides with ammonia. Understanding the structure and reactivity of these catalysts will help to improve their applications. Even though many experimental studies have been performed in this direction, the structure of these catalysts is not completely understood. The adsorption of hydrated vanadia species on the anatase (101), (001), and (100) surfaces is studied using MSINDO-MD. Surfaces of solids are simulated using the two-dimensional cyclic cluster model (CCM). Constant temperature MD simulations are performed to find the stability of various adsorption structures at room temperature. The reactions of the surface hydroxyl groups with the hydrated vanadia species are also investigated. The results of these calculations are used to explain various experimental observations from the literature.

TiO₂-rutile is used as a catalyst and for the designing of electrical and electronic appliances. Point defects are always present in the rutile bulk and on the surface. In order to understand the reactivity of rutile at high temperature, it is important to investigate the stability and diffusion of the point defects. With the MD techniques implemented in MSINDO, diffusion of oxygen vacancies in rutile is simulated and the activation barriers for such processes are estimated. Various experimental observations are explained using the results of these calculations.

Water adsorption on the rutile (110) and (100) surfaces is studied. The vibrational density of states of water molecules in monolayer and double layer coverages is estimated from constant temperature MD simulations. The results are compared with the available literature data.

MSINDO-MD implementation is also used for the determination of thermodynamic properties of zinc chalcogenides. The contribution of the thermal entropy to the free energy of mixing of ZnO and ZnS is estimated.

2 Quantum Chemical Methods and Models

The basis of most quantum chemical approaches is the time-independent Schrödinger equation [3, 4]

$$\hat{H}\Psi = E\Psi \quad (2.1)$$

where \hat{H} is the Hamilton operator, Ψ is the wavefunction and E is the energy of the system. The wavefunction Ψ contains all information about the quantum system. \hat{H} is an operator representing the total energy of the system. It can be expressed (in atomic units) for a system of N nuclei and n electrons as,

$$\hat{H} = -\sum_I^N \frac{1}{2M_I} \nabla_I^2 - \sum_i^n \frac{1}{2} \nabla_i^2 - \sum_I^N \sum_i^n \frac{Z_I}{r_{Ii}} + \sum_{j>i}^n \frac{1}{r_{ij}} + \sum_{J>I}^N \frac{Z_I Z_J}{R_{IJ}} \quad (2.2)$$

Here M_I is the mass and Z_I is the atomic number of a nucleus I . The first two terms describe the kinetic energy of the nuclei and the electrons, respectively. The remaining three terms define the potential part of the Hamiltonian and represent the attractive electrostatic interaction between the nuclei and the electrons and the repulsive potential due to the electron-electron and nucleus-nucleus interactions, respectively. r_{ij} is the distance between the electrons i and j , r_{Ii} is the distance between nucleus I and electron i , and R_{IJ} is the distance between the nuclei I and J .

The Schrödinger equation (2.1) can be further simplified by the Born-Oppenheimer approximation. Its basic assumption is that the kinetic energy of the nuclei can be neglected. Therefore the potential energy due to nucleus-nucleus repulsion is a constant. It is therefore convenient to reduce the Hamiltonian (2.2) to the electronic Hamiltonian

$$\hat{H}_{\text{el}} = -\sum_i^n \frac{1}{2} \nabla_i^2 - \sum_I^N \sum_i^n \frac{Z_I}{r_{Ii}} + \sum_{j>i}^n \frac{1}{r_{ij}} \quad (2.3)$$

The electronic Schrödinger equation with \hat{H}_{el} , replacing \hat{H} in (2.1) is

$$\hat{H}_{\text{el}}\Psi_{\text{el}} = E_{\text{el}}\Psi_{\text{el}} \quad (2.4)$$

The solutions of this equation are the electronic wavefunction Ψ_{el} and the electronic energy E_{el} . The total energy E_{tot} of the system is the sum of the electronic energy E_{el} and the constant nuclear repulsion term.

$$E_{\text{tot}} = E_{\text{el}} + E_{\text{nuc}} \quad (2.5)$$

where

$$E_{\text{nuc}} = \sum_{J>I}^N \frac{Z_I Z_J}{R_{IJ}} \quad (2.6)$$

2.1 The Hartree-Fock Approximation

The Schrödinger equation has only been solved exactly for simple model systems. Except hydrogen all elements in the periodic table and all neutral molecules are many-electron systems where the motion of each electron is coupled to the motion of all other electrons. To study these systems approximations are necessary.

One possibility is represented by the Hartree-Fock method [4]. It is based on the assumption that every electron moves in a potential created by the nuclei and the average potential of all the other electrons. In this method the n -electron wavefunction is an antisymmetrized product of n one-electron wavefunctions $\phi_i(\mathbf{q}_i)$. This product is referred to as a Slater determinant, Φ_0 .

$$\Psi_{\text{el}} \approx \Phi_0 = \frac{1}{\sqrt{n!}} \begin{vmatrix} \phi_1(\mathbf{q}_1) & \phi_2(\mathbf{q}_1) & \cdots & \phi_n(\mathbf{q}_1) \\ \phi_1(\mathbf{q}_2) & \phi_2(\mathbf{q}_2) & \cdots & \phi_n(\mathbf{q}_2) \\ \vdots & \vdots & \ddots & \vdots \\ \phi_1(\mathbf{q}_n) & \phi_2(\mathbf{q}_n) & \cdots & \phi_n(\mathbf{q}_n) \end{vmatrix} \quad (2.7)$$

The one-electron functions $\phi_i(\mathbf{q}_i)$ are called spin orbitals, and are composed of a spatial orbital $\psi_i(\mathbf{r})$ and one of the two spin functions, α (+1/2 spin) or β (-1/2 spin).

$$\phi(\mathbf{q}) = \psi(\mathbf{r})\sigma(s) \quad (2.8)$$

with

$$\sigma\left(\frac{1}{2}\right) = \alpha, \quad \sigma\left(-\frac{1}{2}\right) = \beta$$

The spin functions are orthonormal.

$$\langle \alpha | \alpha \rangle = \langle \beta | \beta \rangle = 1$$

$$\langle \alpha | \beta \rangle = \langle \beta | \alpha \rangle = 0$$

Spatial orbitals are usually assumed to form an orthonormal set, $\langle \psi_i | \psi_j \rangle = \delta_{ij}$. The pre-factor $1/\sqrt{n!}$ is necessary for the normalization of the wavefunction. $|\psi(\mathbf{r})|^2 d\mathbf{r}$ represents the probability of finding the electron within the volume element $d\mathbf{r}$.

The exact wavefunction Ψ_{el} is approximated by a Slater determinant Φ_0 . Within the Hartree-Fock approximation the spin orbitals $\{\phi_i\}$ are varied, under the orthonormality

constraint, until a Slater determinant Φ_0 is obtained, which yields the lowest energy. After expansion of the determinant, one can express the electronic Hartree-Fock energy for a closed-shell system as

$$\begin{aligned} E_{\text{HF}} &= \langle \Phi_0 | \hat{H}_{\text{el}} | \Phi_0 \rangle \\ &= 2 \sum_i^{n/2} h_{ii} + \sum_i^{n/2} \sum_j^{n/2} (2J_{ij} - K_{ij}) \end{aligned} \quad (2.9)$$

where

$$\begin{aligned} h_{ii} &= \int \psi_i^*(1) \left\{ -\frac{1}{2} \nabla_1^2 - \sum_I^N \frac{Z_I}{r_{1I}} \right\} \psi_i(1) d\mathbf{r}_1 \\ J_{ij} &= \int \int \psi_i^*(1) \psi_j^*(2) \frac{1}{r_{12}} \psi_i(1) \psi_j(2) d\mathbf{r}_1 d\mathbf{r}_2 \\ K_{ij} &= \int \int \psi_i^*(1) \psi_j^*(2) \frac{1}{r_{12}} \psi_j(1) \psi_i(2) d\mathbf{r}_1 d\mathbf{r}_2 \end{aligned}$$

J_{ij} and K_{ij} are called Coulomb and exchange integrals, respectively. These terms represent the interaction between two electrons.

The orthonormality constraints which must be satisfied during the minimization of the E_{HF} by variation of the $\{\psi_i\}$ introduce the Lagrangian multipliers ϵ_i in the resulting equations. The Hartree-Fock equations, which determine the $\{\psi_i\}$ for which E_{HF} attains its lowest value, are given by

$$\hat{F}\psi_i = \epsilon_i \psi_i \quad (2.10)$$

The Lagrangian multipliers ϵ_i are the eigenvalues of the operator \hat{F} and they have the physical interpretation of orbital energies. The Fock operator \hat{F} is a one-electron operator defined as

$$\hat{F} = \hat{h} + \sum_j^{n/2} [2\hat{J}_j - \hat{K}_j] \quad (2.11)$$

where

$$\begin{aligned} \hat{h} &= -\frac{1}{2} \nabla_1^2 - \sum_I^N \frac{Z_I}{r_{1I}} \\ \hat{J}_j(1)\psi_i(1) &= \int \psi_j^*(2) \frac{1}{r_{12}} \psi_j(2) d\mathbf{r}_2 \psi_i(1) \end{aligned}$$

and

$$\hat{K}_j(1)\psi_i(1) = \int \psi_j^*(2) \frac{1}{r_{12}} \psi_i(2) d\mathbf{r}_2 \psi_j(1)$$

A numerical solution of the Hartree-Fock equations is practicable only in atomic calculations, but not for molecules. Roothaan showed that by expanding the molecular orbitals ψ_i in atomic orbitals $\{\chi_\mu\}$,

$$\psi_i = \sum_{\mu}^m c_{\mu i} \chi_{\mu} \quad (2.12)$$

the differential equation can be converted into a set of algebraic equations [4]. These are then solved by standard matrix algebra techniques. The atomic orbitals are generally chosen as Slater-type orbitals [3]. Slater-type orbitals have the form

$$\frac{[2\zeta]^{n+1/2}}{[(2n)!]^{1/2}} r^{n-1} \exp(-\zeta r) Y_l^m(\theta, \psi)$$

where ζ is the orbital exponent, $Y_l^m(\theta, \psi)$ is a spherical harmonic function, and n , l , and m are quantum numbers. More recently Gaussian functions are used in the expansion of molecular orbitals. Gaussian-type orbitals are defined as

$$\left(\frac{2\alpha}{\pi}\right)^{3/4} \left[\frac{(8\alpha)^{i+j+k} i! j! k!}{(2i)! (2j)! (2k)!}\right]^{1/2} x^i y^j z^k \exp(-\alpha r^2)$$

Here i , j and k are integers, x , y , and z are Cartesian coordinates and α is the orbital exponent of the Gaussian-type function.

A matrix equation for $c_{\mu i}$ is obtained by substituting (2.12) in (2.10).

$$\sum_{\nu}^m F_{\mu\nu} c_{\nu i} = \epsilon_i \sum_{\nu}^m S_{\mu\nu} c_{\nu i} ; \mu = 1, 2, \dots, m \quad (2.13)$$

$$\mathbf{FC} = \mathbf{SC}\epsilon$$

The overlap matrix \mathbf{S} has elements

$$S_{\mu\nu} = \int \chi_{\mu}^*(1) \chi_{\nu}(1) d\mathbf{r}_1 \quad (2.14)$$

The Fock matrix \mathbf{F} has elements

$$F_{\mu\nu} = \int \chi_{\mu}^*(1) \hat{F}(1) \chi_{\nu}(1) d\mathbf{r}_1 \quad (2.15)$$

$$= H_{\mu\nu} + \sum_{\rho}^m \sum_{\sigma}^m P_{\rho\sigma} \left[(\mu\nu | \rho\sigma) - \frac{1}{2} (\mu\sigma | \rho\nu) \right]$$

The electronic Hartree-Fock energy, E_{HF} , is obtained as

$$E_{\text{HF}} = \frac{1}{2} \sum_{\mu}^m \sum_{\nu}^m P_{\mu\nu} (H_{\mu\nu} + F_{\mu\nu})$$

where

$$H_{\mu\nu} = \int \chi_{\mu}^*(1) \left\{ -\frac{1}{2} \nabla_1^2 - \sum_I^N \frac{Z_I}{r_{1I}} \right\} \chi_{\nu}(1) d\mathbf{r}_1$$

$$\begin{aligned}
 (\mu\nu | \rho\sigma) &= \iint \chi_\mu^*(1) \chi_\rho^*(2) \frac{1}{r_{12}} \chi_\nu(1) \chi_\sigma(2) d\mathbf{r}_1 d\mathbf{r}_2 \\
 P_{\mu\nu} &= 2 \sum_i^{n/2} c_{\mu i} c_{\nu i}
 \end{aligned}$$

Here $H_{\mu\nu}$ and $P_{\mu\nu}$ are the elements of the core matrix \mathbf{H} and the density matrix \mathbf{P} , respectively.

An orthonormal set of basis functions is obtained as

$$\lambda_\nu = \sum_{\mu}^m a_{\mu\nu} \chi_\mu \quad (2.16)$$

Here the coefficients $a_{\mu i}$ are the elements of transformation matrix $\mathbf{S}^{-1/2}$. In this orthonormal set the overlap matrix will be the unit matrix.

$$S_{\mu\nu}^\lambda = \langle \lambda_\mu | \lambda_\nu \rangle = \delta_{\mu\nu} \quad (2.17)$$

The Hartree-Fock-Roothaan equations (2.13) will thus have a simpler form as

$$\mathbf{F}^\lambda \mathbf{C}^\lambda = \mathbf{C}^\lambda \boldsymbol{\epsilon} \quad (2.18)$$

The elements of the matrix \mathbf{C}^λ are the coefficients in the linear expansion of the molecular orbitals $\{\psi_i\}$ in terms of the orthonormal basis functions $\{\lambda_\mu\}$.

$$\psi_i = \sum_{\mu}^m c_{\mu i}^\lambda \lambda_\mu \quad (2.19)$$

The \mathbf{F}^λ and \mathbf{F} matrices and \mathbf{C}^λ and \mathbf{C} matrices are related in the following way.

$$\mathbf{F}^\lambda = \mathbf{S}^{-1/2} \mathbf{F} \mathbf{S}^{-1/2} \quad \text{and} \quad \mathbf{C}^\lambda = \mathbf{S}^{1/2} \mathbf{C} \quad (2.20)$$

The Hartree-Fock-Roothaan equations are solved by an iterative procedure called self-consistent field (SCF) procedure [3]. In this iterative method, an initial guess is made for the coefficients $\mathbf{C}^{(0)}$ and a first density matrix $\mathbf{P}^{(0)}$ is obtained. The molecular integrals are calculated for a given nuclear configuration $\{\mathbf{R}\}$. The Fock matrix $\mathbf{F}^{(0)}$ is then evaluated. Then the matrix $\mathbf{F}^{\lambda(0)}$ is obtained using (2.20). Diagonalization of $\mathbf{F}^{\lambda(0)}$ gives $\mathbf{C}^{\lambda(1)}$ and $\boldsymbol{\epsilon}$. Using (2.20) a new coefficient matrix $\mathbf{C}^{(1)}$ and thus the density matrix $\mathbf{P}^{(1)}$ can be obtained from $\mathbf{C}^{\lambda(1)}$. This procedure will be continued, with the evaluation of the new $\mathbf{F}^{(1)}$, $\mathbf{F}^{\lambda(1)}$, its eigenvalues and eigenvectors $\mathbf{C}^{\lambda(2)}$ until the density matrix elements of the new step differ by a predefined convergence factor from the previous step.

For closed-shell systems, electrons of opposite spins occupy pairwise the same spatial orbital. The corresponding Hartree-Fock wavefunction is called restricted Hartree-Fock (RHF) wavefunction. There are two methods available for the treatment of open-shell systems, the restricted open-shell Hartree-Fock (ROHF) method and the unrestricted Hartree-Fock (UHF) method. In the ROHF approach the wavefunction is divided into a closed-shell and an open-shell part. In the closed-shell part the paired electrons are given the same spatial orbital function [5]. In a UHF wavefunction, the electrons of α and β spin are allowed to have different spatial orbitals [6]. But the problem with the UHF method is that there is usually a spin contamination in its wavefunction.

Approaches that are based on the Hartree-Fock SCF procedure without additional approximation are called *ab initio* methods. But *ab initio* methods are computationally costly due to the calculation of multi-center integrals, whose number increases with m^4 , where m is the number of basis functions. Thus they are restricted to systems with less than 100 atoms. For treating larger systems, a more approximate treatment is necessary, e.g. by applying semiempirical methods. Semiempirical methods neglect a large part of the integrals by using justifiable approximations. Thus they are computationally more efficient compared to *ab initio* methods. In order to compensate the neglect of the integrals, some of the remaining two-center integrals and the core integrals are replaced by empirical expressions that contain adjustable parameters. These parameters are optimized to reproduce experimental properties. In many cases semiempirical methods are able to reproduce experimental data with similar accuracy as *ab initio* methods at much lower computational cost. In the present work large and complex systems are investigated. For this reason the semiempirical method MSINDO was used for the calculations. Details of this method is described in the next section.

2.2 The Semiempirical Method MSINDO

MSINDO (Modified Symmetrically Orthogonalized Intermediate Neglect of Differential Overlap) [2] is a modified version of the semiempirical SCF molecular orbital method SINDO1 [7] based on the INDO formalism by Pople et al. [8]. The underlying assumption on which the semiempirical methods are based on, is the ZDO (Zero Differential Overlap) approximation. This assumption leads to the neglect of integrals which de-

pend on the overlap of different orbitals.

$$\chi_\mu^*(1)\chi_\nu(1) d\mathbf{r}_1 = 0 \quad \text{for } \mu \neq \nu \quad (2.21)$$

By using the ZDO approximation, three- and four-center integrals vanish. The two-electron integrals of the form $(\mu_A\nu_B|\rho_C\sigma_D)$ will become $(\mu_A\mu_A|\rho_C\rho_C)\delta_{\mu_A\nu_B}\delta_{\rho_C\sigma_D}$. At the INDO level one-center integrals of the form $(\mu_A\mu_A|\mu_A\mu_A)$, $(\mu_A\mu_A|\nu_A\nu_A)$ and $(\mu_A\nu_A|\mu_A\nu_A)$ are retained. The ZDO approximation is also applied to potential terms of the one-electron integrals.

In MSINDO, the ZDO approximation is justified by an approximate Löwdin transformation to the orthogonalized basis [9]. For the atoms in the second and the third row with $3d$ orbitals, additional one-center hybrid integrals of the form $(\mu_A\mu_A|\rho_A\sigma_A)$, $(\mu_A\rho_A|\mu_A\sigma_A)$ and $(\mu_A\nu_A|\rho_A\sigma_A)$ are taken into account in order to preserve rotational invariance [10]. MSINDO uses a pseudominimal basis set of Slater-type valence atomic orbitals and takes into account the core electrons by Zerner's pseudopotential [11]. Thus $\{1s\}$ orbitals for H, $\{2s, 2p\}$ for first row elements, $\{3s, 3p\}$ for Na and Mg, $\{3s, 3p, 3d\}$ for Al-Cl, $\{4s, 4p\}$ for K and Ca, $\{3d, 4s, 4p\}$ for Sc to Zn and $\{4s, 4p, 4d\}$ for Ga to Br, are considered explicitly. In order to describe hydrogen bonding, an additional set of $2p$ orbitals can be introduced on hydrogen.

Using nonorthogonal basis functions, one-center elements of the core matrix \mathbf{H} are given by,

$$H_{\mu_A\mu_A} = U_{\mu_A} + \sum_{B \neq A} (V_{\mu_A\mu_A}^B + V_{\mu_A\mu_A}^{B,\text{corr}}) - \sum_{B \neq A} \sum_{\rho_B} S_{\mu_A\rho_B}^2 \epsilon_{\rho_B} \quad (2.22)$$

$$H_{\mu_A\nu_A} = \sum_{B \neq A} (V_{\mu_A\nu_A}^B + V_{\mu_A\nu_A}^{B,\text{corr}}) - \sum_{B \neq A} \sum_{\rho_B} S_{\mu_A\rho_B} S_{\nu_A\rho_B} \epsilon_{\rho_B}$$

where
$$U_{\mu_A} = \left\langle \mu_A \left| -\frac{1}{2}\nabla^2 - \frac{Z_A}{r_A} \right| \mu_A \right\rangle$$

$$V_{\mu_A\nu_A}^B = \left\langle \mu_A \left| -\frac{Z_B}{r_B} \right| \nu_A \right\rangle$$

$$\begin{aligned} V_{\mu_A\mu_A}^{B,\text{corr}} &= \sum_{\nu_B} n_{\nu_B} \left\langle \mu_A \left| \hat{J}_{\nu_B} - \hat{J}_{\nu_B}^s \right| \mu_A \right\rangle \\ &= \sum_{\nu_B} n_{\nu_B} [(\mu_A\mu_A|\nu_B^s\nu_B^s) - (\mu_A^s\mu_A^s|\nu_B^s\nu_B^s)] \end{aligned} \quad (2.23)$$

Here U_{μ_A} are determined from average energies of atomic configurations. $V_{\mu_A\mu_A}^{B,\text{corr}}$ is a directional correction term for $V_{\mu_A\mu_A}^B$, which partially compensates the neglect of

directional effects in the two-center Coulomb integrals. ν_B is a valence orbital at center B and n_{ν_B} is its atomic occupation number. μ_A^s and ν_B^s are treated like s orbitals. \hat{J}_{ν_B} and $\hat{J}_{\nu_B}^s$ are Coulomb operators. The atomic orbital ν_B is taken as an s orbital in \hat{J}_{ν_B} , while all orbitals are taken as s orbitals for the evaluation of $\hat{J}_{\nu_B}^s$. The last term in (2.22) is a pseudopotential which takes care of the inner orbitals ρ_B . ϵ_{ρ_B} is the diagonal Fock matrix element of the core orbital, ρ_B . The Mulliken approximation is used for calculating the two-center core integrals along with a correction term, $L_{\mu_A\nu_B}$ [12].

$$H_{\mu_A\nu_B} = \frac{1}{2}S_{\mu_A\nu_B} (H_{\mu_A\mu_A} + H_{\nu_B\nu_B}) + L_{\mu_A\nu_B} \quad (2.24)$$

The correction term $L_{\mu_A\nu_B}$ has the form

$$L_{\mu_A\nu_B} = -\frac{1}{2}(\zeta_{\mu_A}^2 + \zeta_{\nu_B}^2) \frac{S_{\mu_A\nu_B} (1 - |S_{\mu_A\nu_B}|)}{1 + \rho} \quad (2.25)$$

$$\text{where } \rho = \frac{1}{2}(\zeta_{\mu_A} + \zeta_{\nu_B}) R_{AB}$$

Here the ζ 's are the orbital exponents. Two center two-electron integrals are evaluated analytically over s -functions. The Fock-matrix elements are given by

$$\begin{aligned} F_{\mu_A\mu_A} &= H_{\mu_A\mu_A} + \sum_{\rho_A} \sum_{\sigma_A} P_{\rho_A\sigma_A} \left[(\mu_A\mu_A|\rho_A\sigma_A) - \frac{1}{2}(\mu_A\sigma_A|\rho_A\mu_A) \right] \\ &\quad + \sum_{B \neq A} \sum_{\rho_B} P_{\rho_B\rho_B} (\mu_A\mu_A|\rho_B\rho_B) \\ F_{\mu_A\nu_A} &= H_{\mu_A\nu_A} + \sum_{\rho_A} \sum_{\sigma_A} P_{\rho_A\sigma_A} \left[(\mu_A\nu_A|\rho_A\sigma_A) - \frac{1}{2}(\mu_A\sigma_A|\rho_A\nu_A) \right] \\ F_{\mu_A\nu_B} &= H_{\mu_A\nu_B} + \frac{1}{2}P_{\mu_A\nu_B} (\mu_A\mu_A|\nu_B\nu_B) \end{aligned} \quad (2.26)$$

The core matrix is transformed to the Löwdin orthogonalized basis as below.

$$\mathbf{H}^\lambda = \mathbf{S}^{-1/2} \mathbf{H} \mathbf{S}^{-1/2} \quad (2.27)$$

$\mathbf{S}^{-1/2}$ can be expanded in a Taylor series.

$$\begin{aligned} \mathbf{S}^{-1/2} &= (\mathbf{1} + \bar{\mathbf{S}})^{-1/2} \\ &= \mathbf{1} - \frac{1}{2}\bar{\mathbf{S}} + \frac{3}{8}\bar{\mathbf{S}}^2 - \frac{5}{16}\bar{\mathbf{S}}^3 + \dots \end{aligned} \quad (2.28)$$

Here $\bar{\mathbf{S}}$ is the overlap matrix with zero diagonal elements. \mathbf{H}^λ is usually approximated in the overlap expansion, to second order in SINDO1, but only to first order in MSINDO.

The latter avoids the problems connected with large overlap. The core matrix elements will take the following form [2].

$$\begin{aligned}
 H_{\mu_A\mu_A}^\lambda &= H_{\mu_A\mu_A} - f^{B,\text{orth}} \sum_{B \neq A} \sum_{\rho_B} S_{\mu_A\rho_B} L_{\mu_A\rho_B} \\
 H_{\mu_A\nu_A}^\lambda &= H_{\mu_A\nu_A} - \frac{1}{2} f^{B,\text{orth}} \sum_{B \neq A} \sum_{\rho_B} (L_{\mu_A\rho_B} S_{\rho_B\nu_A} + S_{\mu_A\rho_B} L_{\rho_B\nu_A}) \\
 H_{\mu_A\nu_B}^\lambda &= L_{\mu_A\nu_B} + H_{\mu_A\nu_B}^{\text{corr}}
 \end{aligned} \tag{2.29}$$

Here $f^{B,\text{orth}}$ is a correction factor which compensates the different numbers of basis functions used for the elements and (partially) the neglect of higher order terms in (2.27). $H_{\mu_A\nu_B}^{\text{corr}}$ is an empirical correction term given by

$$\begin{aligned}
 H_{\mu_A\nu_B}^{\text{corr}} &= \frac{1}{4} (K_A + K_B) S_{\mu_A\nu_B} (f_A h_{\mu_A\mu_A} + f_B h_{\nu_B\nu_B}) \\
 \text{with } f_A &= 1 - \exp(-\kappa_{P_B}(A)R_{AB}) \\
 f_B &= 1 - \exp(-\kappa_{P_A}(B)R_{AB})
 \end{aligned} \tag{2.30}$$

The K 's here in this equation are adjustable parameters dependent only on the type of the elements and the orbital symmetry. The κ 's are atomic parameters of interperiodic nature. MSINDO has been parametrized for the elements H, Li-F, Na-Cl and K-Br [13–15].

Special techniques like an embedding procedure [16] and the cyclic cluster model [17] for the description of solids and surfaces have been developed and incorporated in MSINDO. The method has been successfully applied to various solid state problems such as properties of bulk solids [18], adsorptions [19] and surface reactions [20].

2.3 Cyclic Cluster Model

Quantum chemical methods are widely used for investigating bulk and surface properties of crystalline systems. Two quantum chemical models frequently used to describe crystals are periodic supercells and clusters.

In the cluster model [21] a small portion of a crystal or a surface is used as representative for the whole system. This quasi-molecular system can be treated by all quantum chemical methods. The cluster model has the advantage that it can describe local effects. A disadvantage is the existence of boundary effects due to the atoms at the

border with incomplete coordination. The local symmetry of the crystal is not preserved in this approach. Moreover, the long-range Coulomb interactions are completely neglected. This problem can be solved to some extent by systematically increasing the cluster size and extrapolating the results to the infinite limit [22]. The problems due to the lack of saturation at the cluster boundary can be overcome by saturating atoms with hydrogen. Long-range Coulomb interactions can be accounted for embedding in point charges [16]. But these schemes do not entirely solve the problems of free cluster models.

The deficiencies of the cluster approach can be overcome by generating periodic boundary conditions for the cluster model. By this approach every local part of the cluster that is translationally equivalent will have identical environment and thus the local symmetry is preserved throughout the cluster. Such an approach is called cyclic cluster model (CCM) [17]. In the CCM a conceptually cyclic arrangement is created for every atom in the cluster by translations of the neighboring atoms. In the following example, an infinite one-dimensional (AB) chain is modelled by a cyclic (AB)₃ cluster



In order to define the interaction region \mathcal{R} for every atom of the cyclic cluster, the cluster atoms are translated as follows.

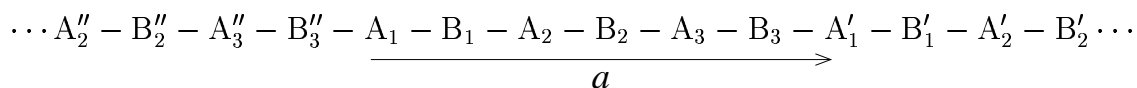


Figure 2.1: Translation of the one dimensional chain in CCM

Here a is the length of the translational vector. The atoms with primes (') and double primes (") are the translated images of the real cluster (2.31) in positive and negative x directions, respectively. Only interactions within the distance $r \leq |a|/2$ are taken into account. Thus the interactions of each atom in (2.31) in the CCM can be represented as in Table 2.1. The interaction region means the region around an atom in which all the multi-center integrals containing the central atom are evaluated.

Table 2.1: CCM interaction matrix for the linear chain (2.31). Here I is a central atom and $\mathcal{R}(I)$ is its interaction region.

$\mathcal{R}(I)$			I	$\mathcal{R}(I)$		
B_2''	A_3''	B_3''	A_1	B_1	A_2	B_2
A_3''	B_3''	A_1	B_1	A_2	B_2	A_3
B_3''	A_1	B_1	A_2	B_2	A_3	B_3
A_1	B_1	A_2	B_2	A_3	B_3	A_1'
B_1	A_2	B_2	A_3	B_3	A_1'	B_1'
A_2	B_2	A_3	B_3	A_1'	B_1'	A_2'

In MSINDO the atoms at the border of the interaction sphere are treated in a different way as in previous implementations of this approach [17]. If an atom J is located at the border of the interaction region for a central atom I , a weighting factor ω_{IJ} is introduced for the calculation of interaction integrals between atoms I and J . The weighting factor is evaluated as the reciprocal of the total number of such atoms on the border. In the above example of a one-dimensional chain, there are two neighbors at the border of the interaction region of every atom in the cluster at $\pm|a|/2$. Thus ω_{IJ} will be $1/2$ for the integrals involving the border atoms. The modified interaction matrix for this case is given in Table 2.2.

Table 2.2: Weighted CCM interaction matrix for the linear chain (2.31). Here I is a central atom and $\mathcal{R}(I)$ is its interaction region.

$\mathcal{R}(I)$			I	$\mathcal{R}(I)$		
$\frac{1}{2}B_2''$	A_3''	B_3''	A_1	B_1	A_2	$\frac{1}{2}B_2$
$\frac{1}{2}A_3''$	B_3''	A_1	B_1	A_2	B_2	$\frac{1}{2}A_3$
$\frac{1}{2}B_3''$	A_1	B_1	A_2	B_2	A_3	$\frac{1}{2}B_3$
$\frac{1}{2}A_1$	B_1	A_2	B_2	A_3	B_3	$\frac{1}{2}A_1'$
$\frac{1}{2}B_1$	A_2	B_2	A_3	B_3	A_1'	$\frac{1}{2}B_1'$
$\frac{1}{2}A_2$	B_2	A_3	B_3	A_1'	B_1'	$\frac{1}{2}A_2'$

Within the CCM, the one-center core Hamiltonian elements (2.22) are modified as

$$\begin{aligned}
 H_{\mu_A\mu_A} &= U_{\mu_A} + \sum_{B \neq A}^{\mathcal{R}(A)} \omega_{AB} (V_{\mu_A\mu_A}^B + V_{\mu_A\mu_A}^{B,\text{corr}}) - \sum_{B \neq A}^{\mathcal{R}(A)} \sum_{\rho_B} S_{\mu_A\rho_B}^2 \epsilon_{\rho_B} \\
 H_{\mu_A\nu_A} &= \sum_{B \neq A}^{\mathcal{R}(A)} \omega_{AB} (V_{\mu_A\nu_A}^B + V_{\mu_A\nu_A}^{B,\text{corr}}) - \sum_{B \neq A}^{\mathcal{R}(A)} \sum_{\rho_B} S_{\mu_A\rho_B} S_{\nu_A\rho_B} \epsilon_{\rho_B}
 \end{aligned} \tag{2.32}$$

where $\mathcal{R}(A)$ is the interaction region for an atom A of the cluster and ω_{AB} is the weighting factor. If ν belongs to an atom B which is not a border atom, the two-center terms $H_{\mu_A\nu_B}$ and Coulomb matrix elements $G_{\mu_A\nu_B}$ consist of single terms [17]. If ν is centered at atom B which is a border atom, $H_{\mu_A\nu_B}$ and $G_{\mu_A\nu_B}$ are calculated as sums over all equivalent border atoms B' , including the reference atom B as,

$$\begin{aligned}
 H_{\mu_A\nu_B} &= \sum_{B'}^{\text{equiv}} \omega_{AB'} H_{\mu_A\nu_{B'}} \\
 G_{\mu_A\nu_B} &= \sum_{B'}^{\text{equiv}} \omega_{AB'} G_{\mu_A\nu_{B'}}
 \end{aligned}$$

CCM calculations are performed in real space. Long-range electrostatic interactions can be approximately taken into account in CCM calculations by embedding in point charges. But it is preferable to exactly calculate interactions between the point charges and the atoms of the cyclic cluster using the Ewald summation technique [23].

Analytical energy gradients for the atomic coordinates, in the framework of CCM, are also implemented in MSINDO [17,23]. Numerical gradients are used for the cell vectors during the cell optimization.

3 Molecular Dynamics

Molecular dynamics (MD) is a technique to investigate the equilibrium and dynamic properties of many-body systems [1,24,25]. It is widely used to obtain the microscopic dynamic and structural properties of different types of systems in chemistry, physics and biology [26]. The main ingredient of MD is the classical law that describes the nuclear motion of the particles of the system. Particles are given initial positions and momenta, and their subsequent trajectories are mapped out by integration of the classical equations of motion. Macroscopic properties are obtained by applying statistical mechanics [1].

3.1 Fundamentals

3.1.1 Equations of Motion

In traditional MD approaches the nuclear motion of the particles is governed by the laws of classical mechanics [1,24–26]. This is a good approximation for a wide range of molecular systems where quantum effects such as tunneling do not play a significant role.

Consider a system of N particles with positions \mathbf{R} and momenta \mathbf{P} . The set of all positions $\{\mathbf{R}_1, \mathbf{R}_2, \dots, \mathbf{R}_N\}$ (or momenta $\{\mathbf{P}_1, \mathbf{P}_2, \dots, \mathbf{P}_N\}$) will be called \mathbf{R}^N (\mathbf{P}^N). Let $U(\mathbf{R}^N)$ define the total potential energy of the particles in the system. The Hamiltonian function H of this system is defined as

$$H(\mathbf{R}^N, \mathbf{P}^N) = \sum_{I=1}^N \frac{\mathbf{P}_I^2}{2M_I} + U(\mathbf{R}^N) \quad (3.33)$$

where M_I is the mass of particle I . The momentum \mathbf{P}_I of a particle I is

$$\mathbf{P}_I = M_I \dot{\mathbf{R}}_I \quad (3.34)$$

For an isolated system the value of the Hamiltonian function does not change with time and is equal to the total energy E of the system.

$$H(\mathbf{R}^N, \mathbf{P}^N) = E \quad (3.35)$$

Equations of motion according to Hamilton's equation [24] are

$$\nabla_{\mathbf{P}_I} H = \frac{\mathbf{P}_I}{M_I} = \dot{\mathbf{R}}_I \quad (3.36)$$

$$\nabla_{\mathbf{R}_I} H = -\dot{\mathbf{P}}_I \quad (3.37)$$

Using (3.33) and (3.34) in (3.37), the following relation can be obtained.

$$\nabla_{\mathbf{R}_I} H = -M_I \ddot{\mathbf{R}}_I = \nabla_{\mathbf{R}_I} U = -\mathbf{F}_I \quad (3.38)$$

The equations of motion can also be derived from the Lagrange formalism. The Lagrange function is

$$L(\mathbf{R}^N, \mathbf{P}^N) = \sum_{I=1}^N \frac{\mathbf{P}_I^2}{2M_I} - U(\mathbf{R}^N) \quad (3.39)$$

The equation of motion can be obtained by using the Euler-Lagrange equation

$$\frac{d}{dt} \nabla_{\dot{\mathbf{R}}_I} L = \nabla_{\mathbf{R}_I} L \quad (3.40)$$

3.1.2 Types of Molecular Dynamics

The popular MD approaches which are used to generate classical trajectories are

- (a) Classical MD
- (b) Born-Oppenheimer MD
- (c) Car-Parrinello MD

Classical MD uses simple analytical empirical potentials to generate U . MD simulations using empirical potentials can treat large systems and generate long trajectories, because the calculation of forces and energies is computationally inexpensive. But it is difficult to describe situations like bond formation, bond breaking and charge transfer by such predefined potentials. Parametrization of model potentials and their accuracy is always a problem with these methods.

Quantum chemical MD simulations consider the motion of the nuclei on a Born-Oppenheimer surface and are thus called Born-Oppenheimer MD (BOMD) [27]. In this approach, the forces on the particles are calculated quantum-chemically and lead to a classical movement of the nuclear positions. Since a self-consistent electronic structure calculation has to be performed for every point of a trajectory, such an approach is computationally demanding for high-level quantum chemical methods.

Car and Parrinello could circumvent this problem to a great extent by treating the orbitals that are used to build up the electronic wavefunction as classically moving

dynamic variables together with the nuclear motion [28]. This mapping of a quantum-classical problem to a two-component purely classical problem was possible because of the adiabatic energy separation of the fast electrons and the slow nuclei [26]. At the beginning of a Car-Parrinello MD simulation, the wave function is initialized from a preliminary self-consistent procedure and a small kinetic energy is attributed to the orbitals. The forces on the orbitals are calculated and the coefficients are varied by integrating classical equations of motion for the orbitals. The kinetic energy related to the time dependence of the orbitals is kept close to zero, so that the system will remain close to the Born-Oppenheimer surface. This approach eliminates the computationally expensive self-consistent electronic structural calculations. But there are two problems connected with this approach. Computationally demanding iterative methods or orthogonalization procedures are necessary to maintain the orthonormality of the orbitals and their velocities during the dynamics simulation. Compared to BOMD simulation, a smaller step size has to be used for the integration of the equations of motion to retain the adiabatic separation between the motion of the nuclei and the electrons.

3.1.3 Integration of the Equations of Motion

An important task in an MD procedure is to generate the trajectory for a set of initial positions and momenta. As the integration of the equations of motion can only be performed numerically, it is impossible to generate an exact trajectory in a computer simulation. The integration is performed by discretization of time and repeated calculation of the forces on the particles. Accurate approaches must have a long term energy conservation and short term reversibility.

The velocity Verlet algorithm [1] is the best choice for this purpose. It is a truncated Taylor series expansion of the trajectory in time. The new positions of the particles at time $t + \Delta t$ are calculated from the positions, forces and velocities at time t .

$$\begin{aligned} \mathbf{R}_I(t + \Delta t) &= \mathbf{R}_I(t) + \dot{\mathbf{R}}_I(t)\Delta t + \frac{1}{2}\ddot{\mathbf{R}}_I(t)\Delta t^2 \\ &= \mathbf{R}_I(t) + \dot{\mathbf{R}}_I(t)\Delta t + \frac{\mathbf{F}_I(t)}{2M_I}\Delta t^2 \end{aligned} \quad (3.41)$$

The velocities at time t are first updated to a time $t + \frac{\Delta t}{2}$.

$$\begin{aligned}\dot{\mathbf{R}}_I(t + \frac{\Delta t}{2}) &= \dot{\mathbf{R}}_I(t) + \frac{1}{2}\ddot{\mathbf{R}}_I(t)\Delta t \\ &= \dot{\mathbf{R}}_I(t) + \frac{\mathbf{F}_I(t)}{2M_I}\Delta t\end{aligned}\quad (3.42)$$

As the positions are already updated to $t + \Delta t$ by (3.41), forces at $t + \Delta t$ can be calculated. The velocities are then further updated to $t + \Delta t$ as

$$\begin{aligned}\dot{\mathbf{R}}_I(t + \Delta t) &= \dot{\mathbf{R}}_I(t + \frac{\Delta t}{2}) + \frac{1}{2}\ddot{\mathbf{R}}_I(t + \Delta t)\Delta t \\ &= \dot{\mathbf{R}}_I(t + \frac{\Delta t}{2}) + \frac{\mathbf{F}_I(t + \Delta t)}{2M_I}\Delta t\end{aligned}\quad (3.43)$$

A proper selection of the time step Δt is very important as it determines the accuracy of the trajectory. For Verlet type algorithms a time step of 1 fs or smaller is used.

There are higher order integrators available for the integration in MD simulations. Such an algorithm enables to use longer time steps without loss of accuracy or even with higher accuracy for a given time step compared to the Verlet algorithm. But higher order algorithms are computationally expensive, require more storage and are not time-reversible. Predictor-corrector algorithms are a popular class of higher order algorithms used in MD simulations [29].

3.1.4 Property Calculation with Molecular Dynamics

Statistical analysis of trajectories obtained from MD simulations can be used to determine a variety of properties of a system [30]. An ensemble is the assembly of all possible microscopic states of a system. All microscopic states have the same constraints that define the system macroscopically. An assembly of all states with fixed total energy E and fixed size (number of particles N and volume V), is called microcanonical (NVE) ensemble. This ensemble is appropriate for a closed isolated system. In a canonical (NVT) ensemble, the number of particles, the volume and the temperature are constant, but the energy can vary. This is appropriate for a closed system in contact with a heat bath. The average of an instantaneous property sampled over a long time is equivalent to the ensemble average. Dynamical systems that obey this equivalence are said to be ergodic.

The temperature T is calculated by making use of the equipartition principle [30].

$$\left\langle \frac{1}{N_f} \sum_{I=1}^N \frac{1}{2} M_I \dot{\mathbf{R}}_I^2 \right\rangle = \frac{1}{2} k_B T \quad (3.44)$$

Here k_B is the Boltzmann constant, and N_f is the number of degrees of freedom of the system. $\langle \rangle$ denotes the ensemble average. For convenience, an instantaneous kinetic temperature $T(t)$ is defined.

$$T(t) = \frac{1}{k_B N_f} \sum_{I=1}^N M_I \dot{\mathbf{R}}_I^2(t) \quad (3.45)$$

Thus,

$$\langle T(t) \rangle = T$$

Two dynamical functions which can be calculated in different ensembles are the velocity autocorrelation function (VACF) and the mean square displacement (MSD) [25]. If the velocities at time t_0 and $t_0 + t$ are similar, their values are said to be correlated. The VACF $G(t)$ gives a quantitative measure of this correlation. It is given by,

$$\begin{aligned} G(t) &= \frac{1}{N} \left\langle \sum_{I=1}^N \dot{\mathbf{R}}_I(t_0) \cdot \dot{\mathbf{R}}_I(t_0 + t) \right\rangle \\ &= \frac{1}{N} \sum_{I=1}^N \frac{1}{t_{\max}} \sum_{t_0}^{t_{\max}} \dot{\mathbf{R}}_I(t_0) \cdot \dot{\mathbf{R}}_I(t_0 + t) \end{aligned} \quad (3.46)$$

In the calculation of $G(t)$, averaging over the starting points t_0 and over the trajectories of all the atoms are performed. The length of the trajectory which is used for the calculation of VACF should be t_{\max} plus the correlation time length needed for $G(t)$. The correlation function $G(t)$ has the same period of oscillations as the velocities. The decay of the correlation function shows the decay in the correlations in atomic motion along the trajectories of the atoms. Vibrational density of states (DOS) can be obtained by taking the Fourier transform $G(\nu)$ of the normalized VACF $G'(t)$.

$$G(\nu) = \lim_{\tau \rightarrow \infty} \frac{1}{\tau} \int_0^\tau G'(t) W(t) \cos(2\pi\nu t) dt \quad (3.47)$$

where

$$G'(t) = \frac{\left\langle \sum_{I=1}^N \dot{\mathbf{R}}_I(t_0) \cdot \dot{\mathbf{R}}_I(t_0 + t) \right\rangle}{\left\langle \sum_{I=1}^N \dot{\mathbf{R}}_I(t_0) \cdot \dot{\mathbf{R}}_I(t_0) \right\rangle} \quad (3.48)$$

Here $W(t)$ is a windowing function [24] which is used for smoothing the spectrum by removing random statistical errors. Different windowing functions are discussed in

Ref. [31]. The vibrational spectrum thus obtained can be related to the data from spectroscopic experiments.

The diffusion coefficient D can be obtained from the VACF by using the Green-Kubo equation [24].

$$D = \frac{1}{3} \int_0^\infty G(t) dt \quad (3.49)$$

The MSD evaluates the mean-squared distance over which the particles have moved in a time interval t . The MSD $\Delta R^2(t)$ is evaluated by

$$\begin{aligned} \Delta R^2(t) &= \frac{1}{N} \left\langle \sum_{I=1}^N [\mathbf{R}_I(t_0 + t) - \mathbf{R}_I(t_0)]^2 \right\rangle \\ &= \frac{1}{N} \sum_{I=1}^N \frac{1}{t_{\max}} \sum_{t_0}^{t_{\max}} [\mathbf{R}_I(t_0 + t) - \mathbf{R}_I(t_0)]^2 \end{aligned} \quad (3.50)$$

Alternatively to (3.49), the diffusion coefficient can be calculated from the MSD using Einstein relations [24].

$$D = \lim_{t \rightarrow \infty} \frac{1}{6t} \Delta R^2(t) \quad (3.51)$$

The MSD is used to identify whether a system behaves like a solid or a fluid. As the self-diffusion coefficient of fluids is much larger than that of solids, the function $\Delta R^2(t)$ increases almost linearly for fluids and remains nearly constant for solids with time [25]. Structural details of the system under consideration can be obtained by calculating the root mean square bond length fluctuation (BLF) δ .

$$\delta = \frac{2}{N(N-1)} \sum_{I < J} \frac{[\langle R_{IJ}^2 \rangle - \langle R_{IJ} \rangle^2]^{\frac{1}{2}}}{\langle R_{IJ} \rangle} \quad (3.52)$$

where R_{IJ} denotes the distance between atoms I and J . The BLF is very sensitive to structural transitions. When a ‘‘melting’’ type of transition occurs, BLF will increase rapidly. Thus a plot of BLF as a function of the temperature gives an idea about the melting temperature. Evaluation of bond length and, similarly, bond angle distribution is also helpful to receive information about the structural details during the simulation. Usually the thermodynamic properties are calculated from the fluctuations of total energy [25]. The molar heat capacity at constant volume C_V is given by

$$C_V = \left(\frac{\partial E}{\partial T} \right)_{NV} \quad (3.53)$$

C_V can be estimated by numerical differentiation of (3.53) after performing a number of canonical ensemble simulations at different temperatures. The following analytical expression can also be used to obtain C_V from a single NVT simulation at a certain temperature T [25].

$$C_V = \frac{1}{k_B T^2} (\langle E^2 \rangle - \langle E \rangle^2) \quad (3.54)$$

As C_V is obtained from fluctuations rather than from a quantity directly obtained from the ensemble average, it is difficult to obtain accurate values for C_V from an MD simulation.

The entropy S is related to other thermodynamic properties as,

$$dS = \frac{dE}{T} + \frac{P}{T} dV - \frac{\mu}{T} dN \quad (3.55)$$

Here P is the pressure, $\mu = G/N$ is the chemical potential and G is the Gibbs free energy. For a canonical ensemble we have

$$\Delta S = S(T_2) - S(T_1) = \int_{T_1}^{T_2} \frac{1}{T} \left(\frac{\partial E}{\partial T} \right)_{NV} dT = \int_{T_1}^{T_2} \frac{C_V}{T} dT \quad (3.56)$$

The integration in (3.56) is evaluated numerically by performing several canonical ensemble simulations at different temperatures between T_1 and T_2 .

A quantum-classical approach can be used for the calculation of thermodynamic properties of crystals. For crystals the vibrational modes can be approximately considered as harmonic [32]. The system is then viewed as a set of $3N$ harmonic oscillators [33, 34]. The total canonical partition function Q can be expressed in terms of the partition functions of the individual modes q_j as

$$Q = \prod_{j=1}^{3N} q_j$$

Therefore,

$$\ln Q = \sum_{j=1}^{3N} \ln q_j \quad (3.57)$$

If the normal frequencies are continuously distributed, (3.57) can be written as

$$\ln Q = \int_0^\infty d\nu G(\nu) \ln q(\nu) \quad (3.58)$$

Here $G(\nu)$ is the distribution of vibrational normal modes of the system. The effective vibrational intensity at frequency ν can be calculated as

$$G(\nu) = \frac{2}{k_B T} \sum_{J=1}^N \sum_{K=1}^3 M_J g_J^K(\nu) \quad (3.59)$$

The spectral density $g_J^K(\nu)$ of an atom J in the K th coordinate ($K = x, y,$ and z in the Cartesian coordinate system) is estimated from the square of the Fourier transform of the velocities as

$$g_J^K(\nu) = \lim_{\tau \rightarrow \infty} \frac{\left| \int_{-\tau}^{\tau} \dot{R}_J^K(t) \exp(-i2\pi\nu t) dt \right|^2}{2\tau}$$

Partition function $q(\nu)$ is given by

$$q(\nu) = \frac{\exp(-\beta h\nu/2)}{1 - \exp(-\beta h\nu)} \quad \text{where} \quad \beta = \frac{1}{k_B T}$$

The entropy S can then be expressed as

$$S = k_B \ln Q + \beta^{-1} \left(\frac{\partial \ln Q}{\partial T} \right)_{N,V} = k_B \int_0^{\infty} d\nu G(\nu) W_s(\nu) \quad (3.60)$$

where

$$W_s(\nu) = \frac{\beta h\nu}{\exp(\beta h\nu) - 1} - \ln [1 - \exp(-\beta h\nu)]$$

Similarly, the heat capacity at constant volume C_V is given by

$$C_V = k_B \int_0^{\infty} d\nu G(\nu) W_c(\nu) \quad (3.61)$$

with

$$W_c(\nu) = (\beta h\nu)^2 \frac{\exp(\beta h\nu)}{(\exp(\beta h\nu) - 1)^2}$$

In this approach the entropy is obtained from a single NVT simulation, while the previous method which uses the thermodynamic integration (3.56) needs several NVT simulations. The quantum-classical method is applicable only in the temperature range in which the harmonic approximation is valid. It can thus be used for crystals in a wide range of temperatures, while for molecular systems it is applicable only at very low temperatures.

3.1.5 Controlling Temperature in Molecular Dynamics

From (3.45) it is clear that

$$T(t) \propto \dot{\mathbf{R}}^2(t) \quad (3.62)$$

This relationship is used for controlling the temperature by linear scaling of the velocities. If $T_{\text{tar}}(t)$ is the target temperature and $T(t)$ is the instantaneous temperature at a time t , the velocities of all the particles are scaled by a factor $\eta(t)$ where

$$\eta(t) = \sqrt{\frac{T_{\text{tar}}(t)}{T(t)}}$$

Therefore the velocities $\dot{\mathbf{R}}^N$ are modified to $\dot{\mathbf{R}}_{\text{tar}}^N$ as

$$\dot{\mathbf{R}}_{\text{tar}}^N(t) = \eta \dot{\mathbf{R}}^N(t) \quad (3.63)$$

This linear scaling method is useful for heating, cooling or equilibrating the system. If the scaling is applied in every n_s steps (called scaling frequency) of the simulation, T_{tar} at a step n_t , where n_t is a multiple of the scaling frequency n_s , is given by

$$T_{\text{tar}}(t) = T_{\text{initial}} + \frac{(T_{\text{final}} - T_{\text{initial}})}{t_{\text{tot}}} n_t \Delta t \quad (3.64)$$

where t_{tot} is the total time of the simulation, T_{final} the final temperature at the end of the simulation, $t = t_{\text{tot}}$, and T_{initial} is the initial temperature of the simulation.

Berendsen et al. [35] proposed a weak coupling of the system to an external temperature bath. This is realized by modifying the equations of motion by inserting stochastic and frictional terms. This scales the particle velocities by a factor $\lambda(t)$.

$$\lambda(t) = \left[1 + \frac{\Delta t}{\tau_T} \left(\frac{T_0}{T(t)} - 1 \right) \right]^{1/2} \quad (3.65)$$

where T_0 is the temperature of the bath and τ_T is the coupling constant. But this method can not produce a canonical ensemble. For performing canonical ensemble simulations, it is preferred to use the Nosé-Hoover chain thermostat. The details of the Nosé-Hoover chain thermostat are described in Section 3.2.1.

3.1.6 Simulated Annealing

With standard methods like steepest descent or Newton-Raphson optimization techniques it is difficult to search for the global minimum structure of systems with a large

number of local minima. In general, gradient based optimization methods will find the minimum that is closest to the initial starting structure. Therefore in order to find the global minimum a large number of initial configurations has to be taken into account. Simulated annealing [36], which is a particular application of the MD approach, is a way to overcome this problem. Starting from an arbitrary configuration the system is heated to a high temperature and then cooled very slowly to 0 K. Heating to a very high temperature will help to overcome the energy barriers. However, there is no general proof that even an infinitely slow cooling leads to the energetically lowest structure. Application of the simulated annealing procedure are described in Section 5.1.

3.2 Advanced Methods

3.2.1 Nosé-Hoover Chain Thermostats

In 1984 Nosé demonstrated that a rigorous canonical distribution in both coordinate and momentum space can be achieved by using the extended system approach [37,38]. In an extended system approach, additional degrees of freedom are introduced to the Hamiltonian of the physical system. The extended system Hamiltonian will generate a microcanonical ensemble, while the physical system is forced to generate a canonical ensemble. The additional degrees of freedom are unitless and have no physical meaning. This approach was shown to be useful for generating other ensembles as well. The Extended Hamiltonian H_{nose} proposed by Nosé is

$$H_{\text{nose}} = \sum_I^N \frac{1}{2 M_I s^2} \mathbf{P}_I^2 + U(\mathbf{R}^N) + \frac{1}{2Q} p_s^2 + g k_B T \ln s \quad (3.66)$$

where s is the additional degree of freedom of the system, Q (dimension energy·[time]²) is the effective mass associated with s , p_s is the momentum of s and g is a parameter which is essentially equal to the number of degrees of freedom of the physical system. A logarithmic dependence of the potential on the variable s , $g k_B T \ln s$, is crucial for producing the canonical ensemble [38]. Equations of motion for this extended system

can be derived from (3.66) as,

$$\begin{aligned}\dot{\mathbf{R}}_I &= \nabla_{\mathbf{P}_I} H_{\text{nose}} = \frac{\mathbf{P}_I}{M_I s^2} \\ \dot{\mathbf{P}}_I &= -\nabla_{\mathbf{R}_I} H_{\text{nose}} = -\nabla_{\mathbf{R}_I} U(\mathbf{R}^N) \\ \dot{s} &= \frac{\partial H_{\text{nose}}}{\partial p_s} = \frac{p_s}{Q} \\ \dot{p}_s &= -\frac{\partial H_{\text{nose}}}{\partial s} = \frac{1}{s} \left(\sum_I \frac{\mathbf{P}_I^2}{M_I} - g k_B T \right)\end{aligned}$$

It is common to use the Nosé scheme in the formulation of Hoover [39]. It is then called Nosé-Hoover thermostat.

In some cases the Nosé-Hoover thermostat runs into ergodicity problems and the desired distribution is not achieved [39]. It is found that for small systems or for high-frequency vibrational modes, the Nosé-Hoover thermostat may fail to generate a canonical distribution [1]. This problem was solved by Martyna et al. [40] by coupling the Nosé-Hoover thermostat with a chain of thermostats. This is called Nosé-Hoover chain (NHC) thermostat. The coupling allows the thermostats to fluctuate. Equations of motion of NHC are given by,

$$\dot{\mathbf{R}}_I = \frac{\mathbf{P}_I}{M_I} \quad (3.67)$$

$$\dot{\mathbf{P}}_I = \mathbf{F}_I - \mathbf{P}_I \frac{p_{\zeta_1}}{Q_1} \quad (3.68)$$

$$\dot{\zeta}_I = \frac{p_{\zeta_i}}{Q_I} \quad (3.69)$$

$$\dot{p}_{\zeta_1} = \left[\sum_{I=1}^N \frac{\mathbf{P}_I^2}{M_I} - N_f k_B T \right] - p_{\zeta_1} \frac{p_{\zeta_2}}{Q_2} \quad (3.70)$$

$$\dot{p}_{\zeta_j} = \left[\frac{p_{\zeta_{j-1}}^2}{Q_{j-1}} - k_B T \right] - p_{\zeta_j} \frac{p_{\zeta_{j+1}}}{Q_{j+1}} \quad \text{for } j = 2, \dots, M-1 \quad (3.71)$$

$$\dot{p}_{\zeta_M} = \left[\frac{p_{\zeta_{M-1}}^2}{Q_{M-1}} - k_B T \right] \quad (3.72)$$

There are M chain variables ζ_j with masses Q_j and momenta p_{ζ_j} in the NHC thermostat. Here $\mathbf{F}_I = -\nabla_{\mathbf{R}_I} U(\mathbf{R}^N)$. The conserved quantity for the NHC is

$$H_{\text{NHC}} = \sum_{I=1}^N \frac{\mathbf{P}_I^2}{2M_I} + \sum_{i=1}^M \frac{p_{\zeta_i}^2}{2Q_i} + U(\mathbf{R}^N) + N_f k_B T \zeta_1 + k_B T \sum_{i=2}^M \zeta_i \quad (3.73)$$

Masses for the extended system variables are taken as

$$\begin{aligned} Q_1 &= N_f k_B T / \omega^2 \\ Q_j &= k_B T / \omega^2 \text{ for } j > 1 \end{aligned} \tag{3.74}$$

where ω is the frequency at which the thermostat particles fluctuate. To make the thermostats oscillate with the particles of the physical system, ω is taken as the characteristic frequency of the real system. But it is not necessary to have accurate masses for the thermostat variables.

Integration of the equations of motion of Nosé-Hoover and NHC thermostat can not be performed directly by using the velocity Verlet algorithm because the forces on the particles at time t are directly dependent on the particle velocities at time t . There are many ways to solve this problem. One way is to use an iterative velocity Verlet algorithm [1]. But this approach does not preserve the reversibility of the equations of motion. An alternative way is to use a multiple time step reversible integrator for the extended system dynamics [41, 42]. The latter approach is used in MSINDO for solving the equations of motion for the NHC thermostat.

3.2.2 Metadynamics

MD methods derived from quantum-chemical methods can be used to investigate complex chemical reactions. Reactions occur when the system migrates from one local minimum to the other, by surmounting energy barriers. The time needed for such reactions to take place depends exponentially on the height of these barriers. In most cases the barriers are large and the reactions occur within a time scale of microseconds or more. With the present day computer technology quantum chemical MD methods can only afford few pico-seconds of simulation.

For a fast and efficient exploration of the free energy surface, Laio and Parrinello [43] devised a method where the free energy surface is filled with Gaussians of appropriate size. This accelerates the movement between the free energy minima on the hypersurface. The basic assumption of this method is that certain reaction coordinates can be defined for a particular reaction, which discriminate reactants and products. These reaction coordinates are functions of the nuclear coordinates. Instead of a coarse-grained approach as used in Ref. [43], a continuous-metadynamics approach was proposed by

Iannuzzi et al. [44]. In this approach an extended system Hamiltonian H_{Meta} is used. Extended system variables $\{s\}$ are introduced to generate a restraining force on the reaction coordinates and a history-dependent potential $V(t, \mathbf{s})$.

$$H_{\text{Meta}} = H_0 + \sum_{\alpha}^{N_s} \frac{1}{2} M_{\alpha} \dot{s}_{\alpha}^2 + \sum_{\alpha}^{N_s} \frac{1}{2} k_{\alpha} [S_{\alpha}(\mathbf{R}_I) - s_{\alpha}]^2 - V(t, \mathbf{s}) \quad (3.75)$$

Here H_0 is the Hamiltonian of the physical system, which is given by (3.33). The second and third terms are the kinetic energy of the collective variables $\{s\}$ and the potential energy from the restrained force on the collective coordinates S_{α} , respectively. N_s is the number of reaction coordinates and M_{α} is the mass of a collective variable s_{α} . The coupling constant k_{α} determines how fast the s_{α} evolve in time with respect to the nuclear motion. $S_{\alpha}(\mathbf{R}_I)$ is the scaled reaction coordinate. S_{α} can be any function of nuclear coordinates, which can define the chemical reaction to be simulated, for e.g. a bond length, a bond angle, a dihedral angle, or a coordination number. Each S_{α} is scaled in such a way that the maximum amplitude of its fluctuations, $\max(|S_{\alpha} - \langle S_{\alpha} \rangle|)$, is equal to 1 in a constant-temperature MD simulation which is performed prior to a metadynamics simulation. S_{α} 's are thus dimensionless and k_{α} is having the dimension of energy. $V(t, \mathbf{s})$ is defined as,

$$V(t, \mathbf{s}) = \sum_{t_i < t} W \exp \left\{ -\frac{[\mathbf{s}(t) - \mathbf{s}(t_i)]^2}{2(\Delta s^{\perp})^2} \right\} \quad (3.76)$$

where $\mathbf{s}(t_i) = \{s_{\alpha}(t_i)\}$, W is the prefactor of the Gaussian and Δs^{\perp} is a parameter which determines the size of the Gaussian. The equations of motion are

$$\dot{\mathbf{P}}_I = -\nabla_{\mathbf{R}_I} H_{\text{Meta}} = -\nabla_{\mathbf{R}_I} U(\mathbf{R}^N) - \sum_{\alpha} k_{\alpha} [S_{\alpha}(\mathbf{R}_I) - s_{\alpha}] (\nabla_{\mathbf{R}_I} S_{\alpha}(\mathbf{R}_I)) \quad (3.77)$$

$$\dot{\mathbf{R}}_I = \nabla_{\mathbf{P}_I} H_{\text{Meta}} = \frac{\mathbf{P}_I}{M_I} \quad (3.78)$$

$$\dot{p}_{s_{\alpha}} = -\frac{\partial H_{\text{Meta}}}{\partial s_{\alpha}} = k_{\alpha} [S_{\alpha}(\mathbf{R}_I) - s_{\alpha}] + \frac{\partial V(t, \mathbf{s})}{\partial s_{\alpha}} \quad (3.79)$$

$$\dot{s}_{\alpha} = \frac{\partial H_{\text{Meta}}}{\partial p_{s_{\alpha}}} = \frac{p_{s_{\alpha}}}{M_{\alpha}} \quad (3.80)$$

where $p_{s_{\alpha}}$ is the momentum of the collective variable s_{α} and

$$\frac{\partial V(t, \mathbf{s})}{\partial s_{\alpha}} = \sum_{t_i < t} -W \frac{[\mathbf{s}(t) - \mathbf{s}(t_i)]}{(\Delta s^{\perp})^2} \exp \left\{ -\frac{[\mathbf{s}(t) - \mathbf{s}(t_i)]^2}{2(\Delta s^{\perp})^2} \right\} \quad (3.81)$$

Metadynamics simulations are performed at a certain temperature using the Nosé-Hoover chain thermostat. The collective variables are updated at every time step of

the simulation. The potential $V(t, \mathbf{s})$ is updated at certain time interval Δt_{Meta} , which is an integer multiple of the MD time step Δt . The parameters $k_\alpha, M_\alpha, \Delta s^\perp$ and W are system dependent. k_α and M_α are chosen in such a way that the dynamics of $\{s\}$ are adiabatically separated from the nuclear motion. The values of these parameters should allow the collective variables to complete at least 3-5 oscillations per picosecond. A large value of Δs^\perp forces a fast escape from free energy minimum. Usually a value between 0.1 and 0.3 is used for Δs^\perp . W must have a value lower than the free energy barrier.

4 Implementation of Molecular Dynamics in MSINDO

4.1 Algorithm for Born-Oppenheimer Molecular Dynamics

The first part in an algorithm for MD based on the velocity-Verlet integrator is the initialization of velocities. Initial velocities $\dot{\mathbf{R}}_0^N$ are assigned from a Maxwell-Boltzmann distribution at a predefined temperature. Such a distribution is usually obtained by scaling a uniform distribution of random numbers \mathbf{u}^N . Random numbers obeys the following condition.

$$\frac{1}{3N} \sum_{I=1}^N \mathbf{u}_I^2 = 1$$

These are produced from a random number generator [24,31] and are scaled by $\sqrt{k_B T_0 / M_I}$, where T_0 is the initial temperature and M_I is the mass of particle I ,

$$\dot{\mathbf{R}}_{I_0} = \sqrt{\frac{k_B T_0}{M_I}} \mathbf{u}_I$$

The forces are calculated analytically [45] for the initial structure. Positions and velocities are updated using (3.41), (3.42). For the updated positions the new forces are evaluated. Using (3.43), velocities are further updated.

The instantaneous temperature is calculated at this point using (3.45). If the present time step is an integer multiple of a defined scaling frequency, the velocities are scaled. The target temperature is estimated using (3.64) and the velocities are scaled using (3.63).

The whole process is repeated for a predefined number of steps. Instantaneous properties like temperature, kinetic energy, potential energy and total energy will be accumulated to calculate the averages and root mean square deviations. Thus a simple algorithm for BOMD is as follows :

- (a) Assign initial positions \mathbf{R}^N and velocities $\dot{\mathbf{R}}^N$
- (b) Calculate energy and forces on the nuclei
- (c) Update the nuclear positions to $t + \Delta t$
- (d) Update the nuclear velocities to a half time step $t + \Delta t/2$
- (f) Calculate energy and forces on the nuclei at $t + \Delta t$

- (g) Update the velocities to $t + \Delta t$
- (h) Estimate the instantaneous temperature $T(t + \Delta t)$
- (i) Modify the velocities, if needed
- (j) Accumulate the instantaneous properties
- (k) Go to step c

The same MD code can be used with the CCM without modification. The computationally expensive part of BOMD is the SCF process and the estimation of the forces. In order to reduce the computational effort, the converged density matrix of the previous time step is taken as the initial guess for the next step.

If the Berendsen's temperature bath is used, the velocities are scaled at every time step of the simulation using (3.65). An alternative way for controlling the temperature is by using the Nosé-Hoover chain (NHC) thermostat. Integration of the equations of motion of the NHC thermostat ((3.67)-(3.72)) is performed by using a reversible multiple time step (MTS) approach [41]. The MTS integration scheme is implemented as described by Martyna et al. [42]. Masses of the thermostat particles are calculated from a predefined thermostat frequency (ω in (3.74)). The initial thermostat variables $\{\zeta\}$ are taken as zero and the initial velocities of the thermostat variables $\{\dot{\zeta}\}$ are assigned from a Maxwell-Boltzmann distribution for the initial temperature (of the physical system). In MSINDO, the NHC thermostat is implemented in such a way that thermostating of the whole system or each particle of the system is possible.

The BOMD algorithm described above has to be modified for the incorporation of metadynamics technique. The collective variables $\{s\}$ are updated at every time step of the simulation using the velocity Verlet algorithm. Initially the $\{s\}$ are set equal to the scaled collective coordinates and their initial velocities are taken as zero. The history-dependent potential (3.76) is updated in every time interval Δt_{Meta} . It is always an integer multiple of MD time step Δt . To have a control on the dynamics of the collective variables, their velocities are scaled. Analytical derivatives of the collective variables with respect to the nuclear coordinates $\nabla_{\mathbf{R}_I} S_\alpha(\mathbf{R}_I)$ are required for metadynamics. At the moment analytical derivatives are implemented for bond lengths, bond angles,

dihedral angles and coordination numbers as reaction coordinates. The corresponding formulas are given in Appendix A.

The algorithm for metadynamics which is implemented in MSINDO is as follows.

- (a) Initialization:
 - Assign the nuclear positions \mathbf{R}^N , velocities $\dot{\mathbf{R}}^N$ and evaluate $\{S(t = 0)\}$
 - Assign initial values for the collective variables $\{s\}$ ($s_\alpha(t = 0) = S_\alpha(t = 0)$)
 - Assign velocities for collective variables $\{\dot{s}\}$
- (b) Calculate energy and forces on the nuclei $[\mathbf{F}^N(t = 0)]$
- (c) Evaluate the analytical derivatives of collective coordinates $\nabla_{\mathbf{R}_I} S_\alpha(\mathbf{R}_I)$
- (d) Correct $\mathbf{F}^N(t = 0)$ by the forces from $\{s\}$ on the nuclei as in (3.77)
- (e) Update the nuclear positions to $t + \Delta t$
- (f) Evaluate new collective coordinates
- (g) Evaluate the forces on $\{s\}$ as in (3.79)
- (h) Update the collective variables $\{s\}$ to $t + \Delta t$
- (i) Update the nuclear velocities to a half time step $t + \Delta t/2$
- (j) Update the velocities of the collective variables to a half time step $t + \Delta t/2$
- (k) Calculate the new energy and the forces on the nuclei $[\mathbf{F}^N(t + \Delta t)]$
- (l) Evaluate $\nabla_{\mathbf{R}_I} S_\alpha(\mathbf{R}_I)$ at $t + \Delta t$
- (m) Correct $\mathbf{F}^N(t + \Delta t)$ by the forces from $\{s\}$
- (n) Update the nuclear velocities
- (o) Calculate the forces on $\{s\}$
- (p) Update the velocities of the collective variables to $t + \Delta t$
- (q) Estimate the instantaneous temperature $T(t)$
- (r) Modify the velocities, if needed

- (s) Estimate the temperature of the collective variables
- (t) Modify these velocities, if needed
- (u) Accumulate the instantaneous properties
- (v) Go to step e

4.2 Test Calculations

4.2.1 Total Energy Conservation

For a microcanonical ensemble simulation, the total energy (defined by the sum of the kinetic energy and the potential energy of all particles) of the system must be conserved. This can be used as a preliminary test of the implementation of MD [46]. A single water molecule was taken as the test case. The simulation was performed with an initial temperature of 300 K for 1 ps using different time steps and SCF convergence criteria. The maximum deviation of the instantaneous total energies from the initial total energy was used as a measure for the total energy conservation during a simulation. The dependence of the maximum energy deviation on the time step and the SCF convergence criteria is given in Table 4.3.

Table 4.3: Maximum energy deviation for different time steps Δt and SCF convergence.

SCF Conv.(a.u.)	Maximum energy deviation (a.u.)		
	$\Delta t = 1$ fs	$\Delta t = 0.5$ fs	$\Delta t = 0.1$ fs
1.0×10^{-4}	4.6×10^{-4}	4.2×10^{-4}	3.3×10^{-4}
1.0×10^{-6}	4.5×10^{-4}	4.1×10^{-4}	3.2×10^{-4}
1.0×10^{-8}	1.0×10^{-4}	7.1×10^{-5}	6.3×10^{-5}
1.0×10^{-10}	5.8×10^{-5}	2.0×10^{-5}	2.0×10^{-5}

For a time step of 1 fs, total energy conservation at every time step of the simulation is plotted for different SCF convergence criteria in Figure 4.2. A drift in total energy conservation is observed when the forces are calculated with lower accuracy (Figure 4.2 a-b). But for very accurate forces, the total energy conservation is in the range

of 10^{-5} a.u. (Figure 4.2 c-d). Usually the MD simulations are performed with a SCF convergence criteria of 10^{-8} a.u. corresponding to the curve c in Figure 4.2.

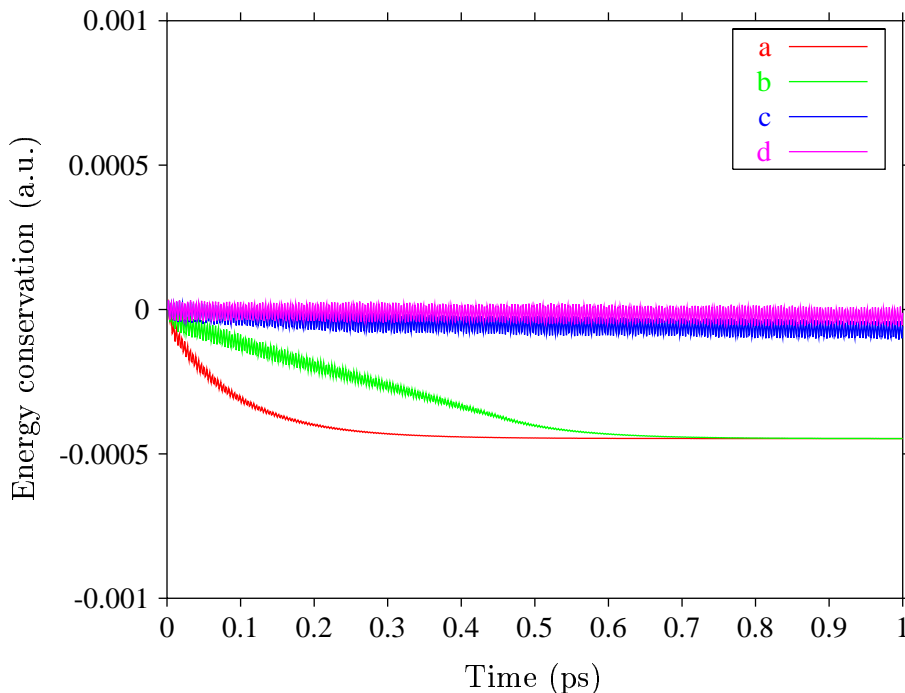


Figure 4.2: Total energy conservation for the following SCF convergence criteria: (a) 1.0×10^{-4} a.u. (b) 1.0×10^{-6} a.u. (c) 1.0×10^{-8} a.u. (d) 1.0×10^{-10} a.u.

4.2.2 Simulated Annealing of Simple Molecules

Capability of the simulated annealing technique using the present MD implementation to find the global minimum structures of simple molecules was tested. N_2 , H_2O , NH_3 , CH_4 , C_6H_6 molecules were taken as the test cases. Initial bond lengths and angles were taken arbitrarily. A time step of 1 fs is used. The systems are heated in 200 steps to 500 K and equilibrated for 1000 steps. This was followed by cooling to 0 K in 2000 steps. In all cases the final structures and energies were indistinguishable from those obtained from quasi Newton-Raphson optimization (Table 4.4). This demonstrates the numerical stability of the present implementation. Of course, a gradient-based optimization is computationally much more efficient than a simulated annealing procedure for finding the equilibrium structures of such simple systems where reasonable starting structures can be provided. But in more complex situation, simulated annealing can be the only way to find the energy minimum structure.

Table 4.4: Final energies and structures of simple molecules obtained by simulated annealing (SA) and quasi Newton-Raphson (QNR) optimization techniques. E_b is the binding energy in kJ/mol, bond lengths (r) are in Å and bond angles (θ) are in degrees.

Molecule	Properties	SA	QNR
N ₂	E_b	-264.4	-264.4
	$r_{\text{N-N}}$	1.096	1.096
H ₂ O	E_b	-268.2	-268.2
	$r_{\text{O-H}}$	0.960	0.960
	$\theta_{\text{H-O-H}}$	104.7	104.7
NH ₃	E_b	-347.8	-347.8
	$r_{\text{N-H}}$	1.009	1.009
	$\theta_{\text{H-N-H}}$	108.2	108.2
CH ₄	E_b	-494.7	-494.7
	$r_{\text{C-H}}$	1.076	1.076
	$\theta_{\text{H-C-H}}$	109.5	109.5
C ₆ H ₆	E_b	-1617.0	-1617.0
	$r_{\text{C-C}}$	1.396	1.393
	$r_{\text{C-H}}$	1.086	1.086
	$\theta_{\text{H-C-C}}$	120.0	120.0

4.2.3 Canonical Ensemble Simulation using the Nosé-Hoover Chain Thermostat

In this section, the accuracy of the implementation of the Nosé-Hoover chain thermostat is demonstrated. A canonical ensemble simulation was performed for ZnS bulk (cubic), using the Nosé-Hoover chain thermostat. A three-dimensional cyclic Zn₃₂S₃₂ cluster was used to define the bulk of ZnS. The cell parameter a was optimized before the MD simulation. An initial temperature of 300 K was assigned to the system and a time step of 0.5 fs was chosen. The whole system was thermostatted using 10 Nosé-Hoover chains. Thermostat frequency was taken as 750 cm⁻¹ which is close to the maximum frequency of vibration of the ZnS lattice. As mentioned in Ref. [42], the frequency of the thermostat is not a critical parameter for obtaining a better average

temperature. Instantaneous temperatures during this simulation for 8000 steps are plotted in Figure 4.3. Total energy conservation of the extended system (3.73) was 8×10^{-4} a.u. and average temperature after 8000 steps was 296 K. These clearly demonstrate the accuracy of the implementation. The average temperature is only 4 K lower than the required temperature of the system. Temperature fluctuations in the initial steps of the simulation were high because of the equilibration process. Thus first few steps can be skipped for the estimation of the properties of the system. When the first 1000 steps were neglected, the average temperature became 300 K, which was exactly the required temperature.

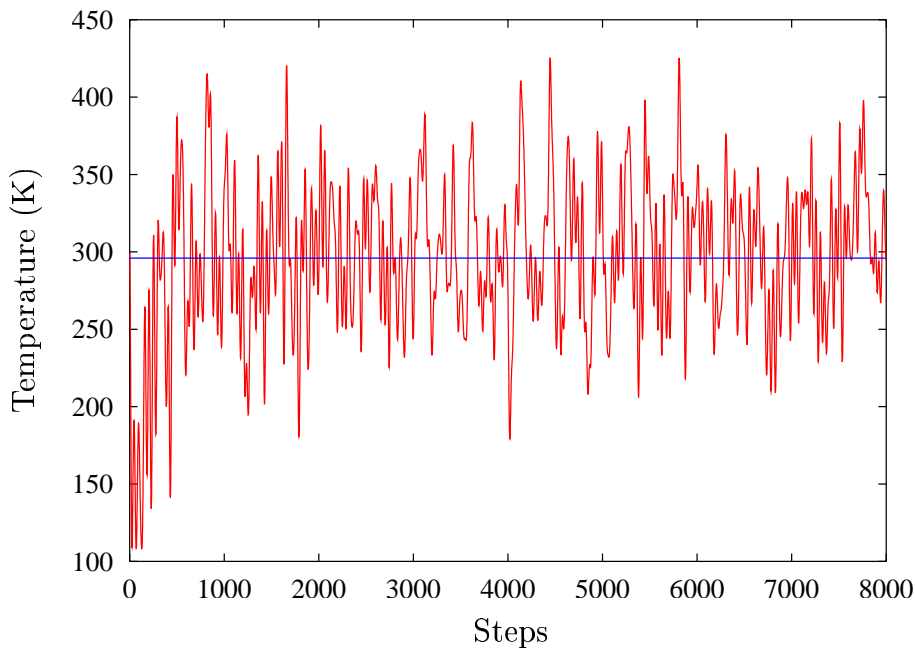


Figure 4.3: Instantaneous temperatures during the canonical ensemble simulation of ZnS bulk are plotted (red line). Average temperature (296 K) for 8000 steps is marked as a blue line.

4.2.4 Exploration of Free Energy Surface using Metadynamics

Si_7 cluster was chosen for testing the implementation of the metadynamics technique. The global minimum structure of Si_7 cluster is a pentagonal bipyramid structure (Figure 4.4a). Metadynamics is used here to explore the free energy surface of the Si_7 cluster. Collective coordinates were selected as the coordination number of each silicon atom. The coordination number is calculated using (A.5), as described in Appendix

A.4. The cutoff bond distance was chosen as 3.0 Å. Before starting the metadynamics simulation, an MD simulation at 300 K was performed for 2000 steps using the Nosé-Hoover chain thermostat with the pentagonal bipyramidal structure (Figure 4.4a). Maximum deviation of the collective coordinates from their average values were estimated and then used to scale the collective coordinates during the metadynamics simulation as mentioned in Section 3.2.2.

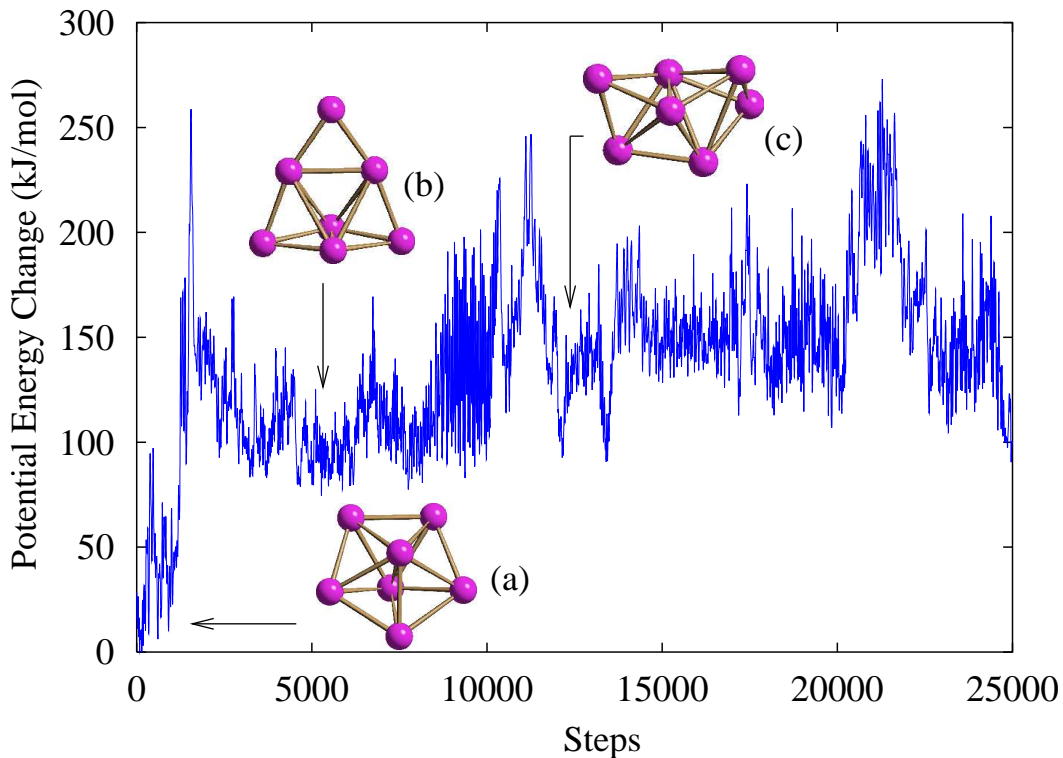


Figure 4.4: Change in the potential energy during the metadynamics simulation of Si_7 cluster. Different isomers of Si_7 cluster (a-c) observed during the simulation are also shown.

A time step of 1 fs was used for the metadynamics simulation. The Nosé-Hoover chain thermostat was used to control the temperature. The parameters Δs^\perp , k_α , M_α and W in (3.75) and (3.76) were 0.3, 1.0 kJ/mol, 40 a.m.u. and 8.0 kJ/mol respectively. The Gaussian functions in (3.76) were updated at every 50th step of the simulation. When the instantaneous temperature of the collective coordinates was increased by more than 0.6 a.u., their velocities were scaled to achieve their average temperature at that instant. The change in the potential energy during the metadynamics simulation is plotted in Figure 4.4. In 2000 steps of the simulation, the structure of Si_7 cluster

changed from that in Figure 4.4a to that in Figure 4.4b. After 12000 steps a new structure Figure 4.4c was observed. Structure in Figure 4.4b and Figure 4.4c were local minimum structures about 80 kJ/mol and 89 kJ/mol higher than the global minimum structure in Figure 4.4a, respectively.

Thus a fast escape of system from the free-energy minima was successfully simulated. This shows that the metadynamics technique is well implemented in MSINDO.

5 Applications of Molecular Dynamics Techniques

5.1 Structure and Melting Behavior of Silicon Clusters

5.1.1 Introduction

In the past two decades a great effort has been taken to understand the global minimum structures of silicon clusters. Gradient-based structural optimizations of small silicon clusters were performed at different levels of theory [47–57]. Kaxiras and Jackson reported that clusters in the range between 20 and 40 atoms prefer to have compact shapes [58]. They predicted that the cross-over from elongated to spherical shapes lies in the range of 24 to 28 silicon atoms. More compact structures with 29 and more Si atoms were investigated by Jug and Krack [59].

As there exists large number of local minima for medium size silicon clusters, gradient based optimization techniques fail to obtain their global minimum structures. MD techniques can be used to overcome the energy barriers and to find the global minimum structure. Dynamic properties and global minimum structures of silicon clusters were investigated using MD techniques [60–68].

A number of theoretical investigations focused on the possible structures of Si_{45} [48, 59, 69–74] after the small reactivity of this cluster has been established experimentally [75]. Kaxiras proposed a structure with a fourfold coordinated silicon atom surrounded by a cage with bonding patterns similar to a 2×1 reconstructed Si(111) surface [69]. Jelski et al. [70] suggested a modification for the structure proposed by Kaxiras. Their proposed structure also had a tetrahedrally coordinated central atom in a bulk environment similar to that suggested by Kaxiras, but the positions of the cage atoms were not similar to those of the reconstructed crystal surface. This structure consists of sixfold coordinated outer atoms and the cage was formed by six-membered rings. A Si_{44} cage with a tetrahedrally coordinated center Si atom weakly connected to the cage was suggested by Jug and Krack [59]. A Si_{40} cage with a Si_5 core was a suggestion from Pan and Ramakrishna [73]. From MD simulations a distorted structure for Si_{45} was derived from a Si_{38} cage with a Si_7 core [72, 74]. Patterson and Messmer reported a possibility of a 17 atom core where the outer atoms resemble the reconstructed surface [48].

The interest in Si_{60} was mainly due to its possible similarity with the analogue C_{60} .

Even though the structure and dynamics of C_{60} are well understood, Si_{60} is still under debate [76–87]. The possibility of Si_{60} having buckminsterfullerene structure with I_h symmetry has been discussed in the literature [76, 77]. With the semiempirical AM1 method an icosahedral geometry was obtained as energy minimum structure [78]. The relative population of I_h and C_{2v} cage structures has been studied using AM1 [79]. Some of the previous density functional (DFT) and HF studies have not investigated other possibilities than this high symmetry structure [80, 81]. In contrast, previous MD investigations report deviations from the ideal I_h symmetry [82–86]. Li and Luo [82] reported a distorted truncated icosahedron with T symmetry. Investigations using the full-potential linear-muffin-tin-orbital MD method reported a distorted cage with T_h symmetry for Si_{60} [83, 84]. But a stacked structure was found to be more stable than a distorted spherical structure using the same method [83]. Khan and Broughton [85] reported a relaxed I_h geometry as the global minimum structure. Chen et al. investigated possible Si_{60} energy minimum structures with the DFT-B3LYP (6-31G*) method [87]. They reported a distorted fullerene-type structure for Si_{60} with C_i symmetry. Menon and Subbaswamy [86] found that a network structure similar to the silicon bulk is more stable than a cage structure.

MD implementation in MSINDO was used to study the structure and melting behavior of silicon clusters. The reliability of the present parametrization for silicon compounds was tested by comparing the global minimum structure of Si_n ($n = 5$ to 7) clusters using simulated annealing and density functional calculations. Constant temperature MD simulations were performed to study the melting behavior of Si_7 cluster. Relative stability of various energy minimum structures of Si_{45} and Si_{60} were obtained using extensive simulated annealing.

5.1.2 Simple Silicon Clusters

In this section the results on the simulated annealing of Si_n ($n = 5$ to 7) clusters are presented. The structural and energetic properties of these clusters are compared to high-level calculations from the literature. In this way the accuracy of MSINDO for the determination of Si cluster properties was examined.

The Si_5 simulation was started with different structures having D_{3h} , C_{2v} and C_{4v} symmetry. Initial velocities were assigned to the system corresponding to 10 K. The systems

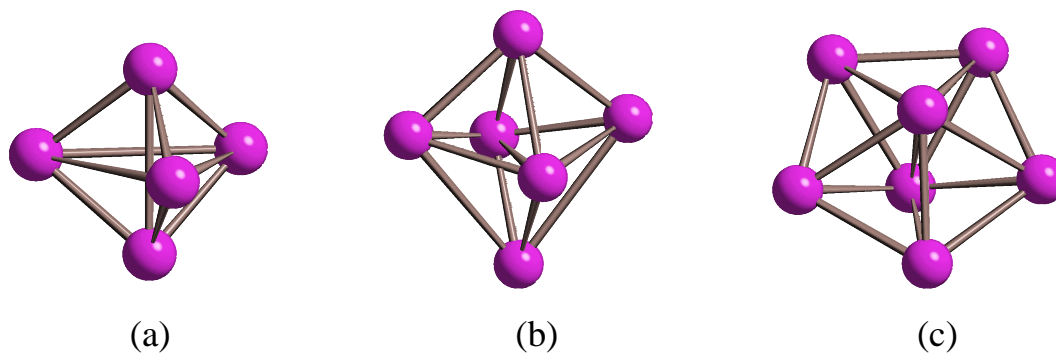


Figure 5.5: Global minimum structures of Si_n ($n = 5 - 7$) clusters.

were then heated to 1000 K in 500 steps and equilibrated for 1000 steps at this temperature. In 2000 steps the systems were cooled to 1 K and then to 0 K in another 1000 steps. Irrespective of the starting structure, the simulation gave a D_{3h} structure at the end of the simulation (Figure 5.5a). A vibrational analysis performed for the final structure confirmed the energy minimum structure. The present result is in agreement with earlier calculations at post-HF, DFT and semiempirical INDO levels of theory [49, 53, 54].

In a similar treatment as above it was found that the global minimum structure of Si_6 is an edge-capped trigonal-bipyramid having C_{2v} symmetry (Figure 5.5b). Simulated annealing runs starting with a D_{4h} structure and a face-capped trigonal-bipyramid both converged to the above C_{2v} structure. Previous SINDO1 calculations by Jug and Krack [54] obtained the same global minimum for this cluster. This result is also in accordance with other calculations at HF and DFT levels of theory [47, 53].

A face-capped octahedron (FCO) of C_{3v} symmetry was suggested as minimum structure for the Si_7 cluster in an earlier study [56]. But when this starting structure was used, the simulated annealing MD converged to a pentagonal bipyramid (PBP) with D_{5h} symmetry (Figure 5.5c). Previous calculations [50, 53, 54] and Raman spectra interpretation [88] of Si_7 are also in agreement with this result. According to MSINDO results the FCO structure was a local minimum lying 101 kJ/mol higher in energy than the global minimum. Simulations starting with a tricapped tetrahedron (TCT) (C_{3v} symmetry) and an edge-capped octahedron (ECO) (C_{2v} symmetry), respectively, also gave a PBP as the final structure. A FCO was found to be approximately 22 kJ/mol lower in energy than a TCT which in turn is 2 kJ/mol more stable than ECO.

Simulation was also started from a ring structure where the seven Si atoms were in a plane. A free run of 1000 steps was first used to relax the structure. Velocities were reset to zero during the free run when the kinetic temperature exceeded 3000 K to avoid dissociation. The final temperature after this free run was below 1000 K. The system was then heated to 1000 K and equilibrated. It was subsequently cooled to 1 K and then to 0 K in 2000 and 1000 steps, respectively. The structure converged again to the PBP. The convergence to the global minimum from different initial structures is shown in Figure 5.6.

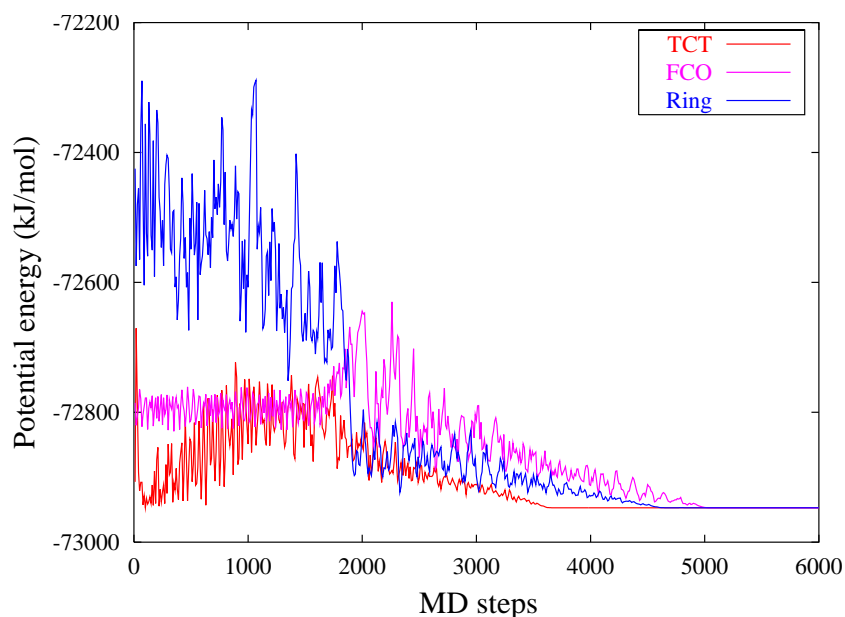


Figure 5.6: Potential energy convergence of the Si_7 cluster to the global minimum from different starting structures; FCO: face-capped octahedron, TCT: tricapped tetrahedron.

Calculated heats of formation for the global minimum structures of Si_n ($n = 5-7$) are in good agreement with the values obtained by experiments [89]. Binding energies of different isomers of Si_n ($n = 5-7$) clusters obtained with MSINDO and from DFT calculations using the Perdew-Wang GGA (PWGGA) exchange-correlation functional [90] are compared in Table 5.6. The DFT reference calculations were performed with Gaussian 98 [91]. It can be seen from this table that there is good agreement of the MSINDO energies with the PWGGA data.

Table 5.5: Calculated heats of formation (kJ/mol) at 298.15 K for Si_n ($n=5-7$) clusters and comparison with experimental results.

Cluster	MD-MSINDO	Exp. ^a
Si_5	707	700 ± 24
Si_6	770	733 ± 41
Si_7	789	743 ± 36

^a Ref. [89]

Table 5.6: Binding energies (kJ/mol) of various isomers of Si_n ($n=5-7$) clusters obtained with MSINDO and PWGGA/6-311G*.

Cluster	Structure	Binding energy	
		MSINDO	PWGGA
Si_5	D_{3h}	-1578	-1552
	C_{4v}	-1437	-1457
	C_{2v}	-1398	-1452
Si_6	C_{2v}	-1978	-1971
	D_{4h}	-1969	-1970
	O_h	-1850	-1750
Si_7	D_{5h}	-2412	-2388
	C_{3v}^a	-2311	-2229
	C_{2v}	-2296	-2193
	C_{3v}^b	-2294	-2188

^a Facecapped octahedron

^b Tricapped tetrahedron

5.1.3 Solid-Liquid Transition of the Si_7 Cluster

Solid-like or liquid-like behavior of a cluster is defined from its structural stability at different temperatures. At high temperatures, the system can cross the energy barriers separating the global minimum from local minima and can undergo a structural transition between these structures. This invokes extra modes of vibration in the

system [64].

Wang et al. [67] and Dinda et al. [65, 66] reported that Si_7 shows a “melting” type of structural transition within a temperature range of 1500 K and 1700 K. A melting temperature of 1680 K was reported in Ref. [65]. Simulation was started from a slight distortion of the equilibrium structure. The simulations were performed from 500 K to 2500 K at intervals of 100 K. The Nosé-Hoover chain thermostat was used for the constant temperature dynamics. For each starting temperature, an equilibration for 3000 steps was followed by the simulations for 32 ps using a time step of 0.4 fs (total of 80,000 steps). For an accurate picture of structural changes, the BLF (3.52) was estimated. Bond length and bond angle distributions at different temperatures were also obtained. The MSD (3.50) was sampled for 5000 time steps over the rest of the data points by shifting the time origin every 10 steps. In Figure 5.7 a sudden increase in BLF from 1600 K to 1800 K can be seen.

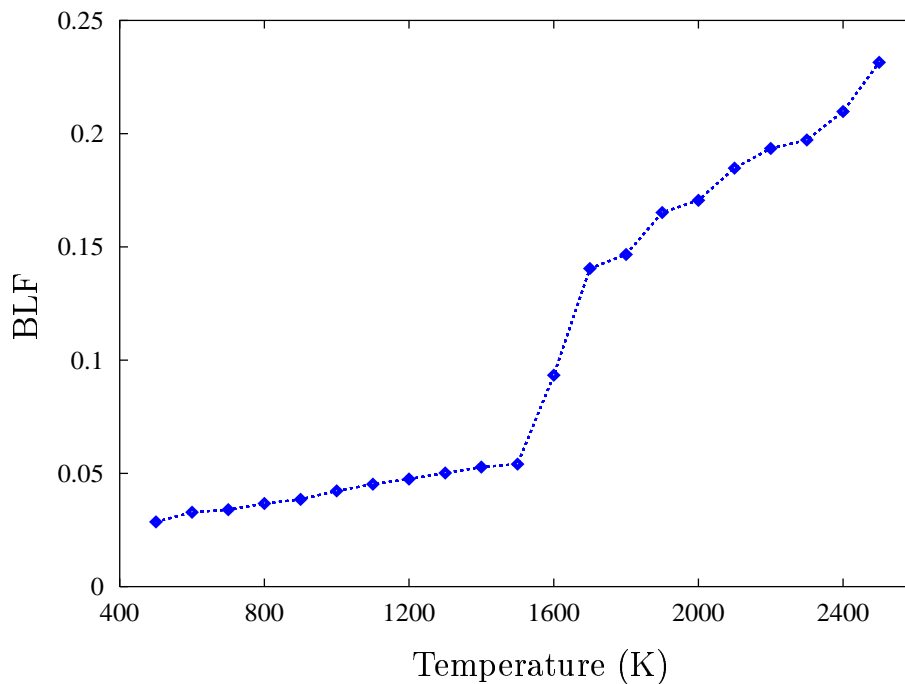


Figure 5.7: Bond length fluctuation (BLF) for Si_7 in dependence of the average temperature of different constant temperature simulations.

It clearly shows that the melting of the Si_7 cluster occurred within this temperature range. The MSD for four different temperatures is shown in Figure 5.8. The MSD curve has almost zero slope up to 1500 K indicating nearly zero diffusion of the silicon

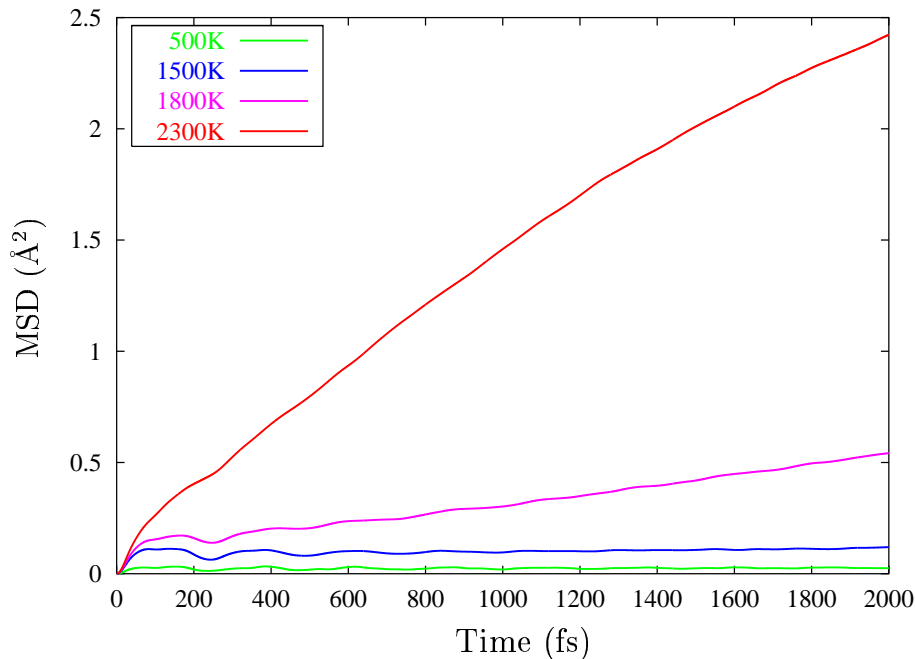


Figure 5.8: Time (fs) dependence of mean square displacement MSD (\AA^2) for a Si_7 cluster.

atoms during the dynamics simulation. MSD at 1800 K has a positive slope which means that structural changes occur in the system at this temperature.

The atomic distance distribution was calculated at different temperatures (Figure 5.9). The peaks around 2.5 \AA and 4 \AA at low temperature are corresponding to the distances of the neighboring atoms and next neighboring atoms, respectively, in the pentagonal-bipyramidal structure. At 1800 K peaks around 2.5 \AA have shifted to a lower value while the second peak spread to higher values. Thus it is clear that oscillations occur in the system by which the distance of next nearest neighbors increases together with a decrease of distances of their neighbor atoms. At high temperatures atomic distances between 2 \AA to 5 \AA can be found in the molecule, which demonstrates a “liquid-like” behavior. Additional atomic distances were appearing when the system starts melting. A similar trend was observed in the bond angle distribution (Figure 5.10). Cut-off bond distance used for evaluating the bond angle distribution was 3.0 \AA . The probability of angles around 50 degrees increased at high temperatures. Additional bond angles between 85 to 90 degrees appeared in the system from 1600 K. These distributions indicate that a structural transition starts in the system from 1600 K. From the snapshots (Figure 5.11) during the MD simulation at 1600 K it was found that the

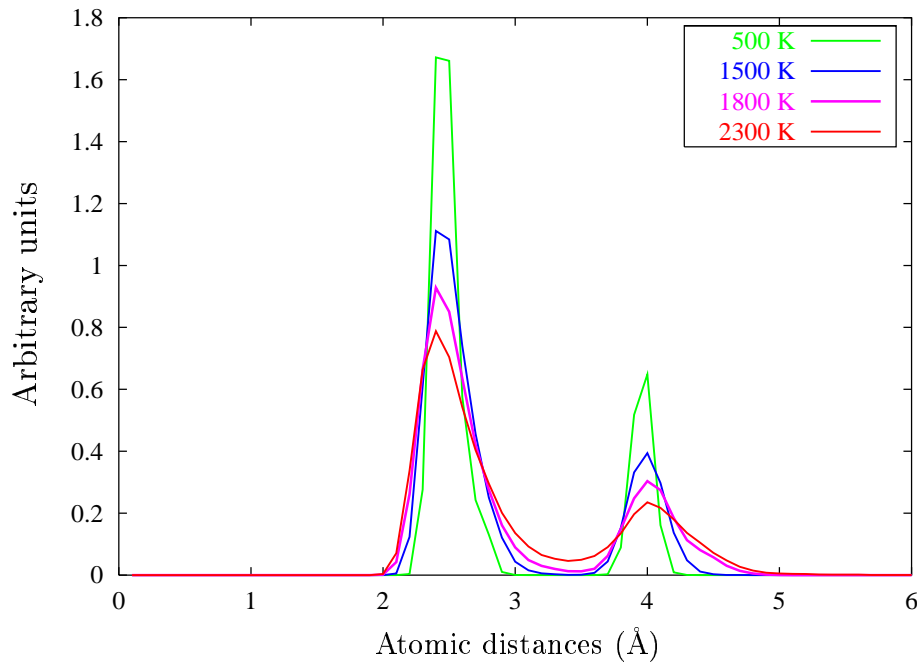


Figure 5.9: Atomic distance distribution of the Si₇ cluster at different temperatures.

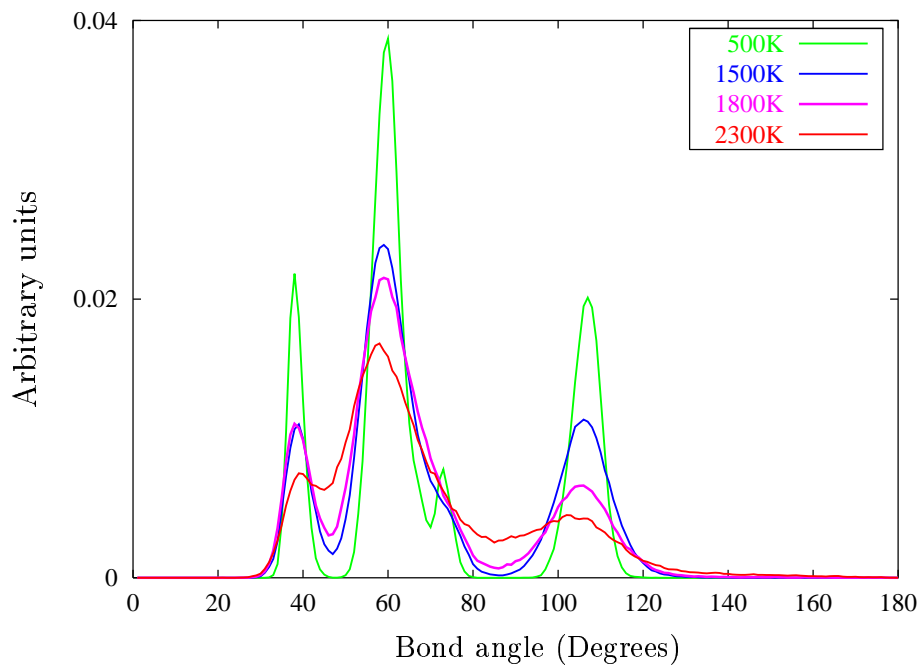


Figure 5.10: Bond angle distribution (BAD) of the Si₇ cluster at different temperatures.

system populates the potential energy surface of a C_{2v} structure given in Figure 5.11d. At high temperatures the system gains vibrational energy and thus can cross the barrier between the pentagonal bipyramid and the above mentioned C_{2v} structure. The C_{2v}

structure is 80 kJ/mol higher in energy than the global minimum structure. When the system is able to cross the barrier, it can freely move throughout the free energy surface between the above two isomers. This results in the above described structural changes. At temperatures higher than 1800 K structural changes to other isomers were also taking place during the MD simulation.

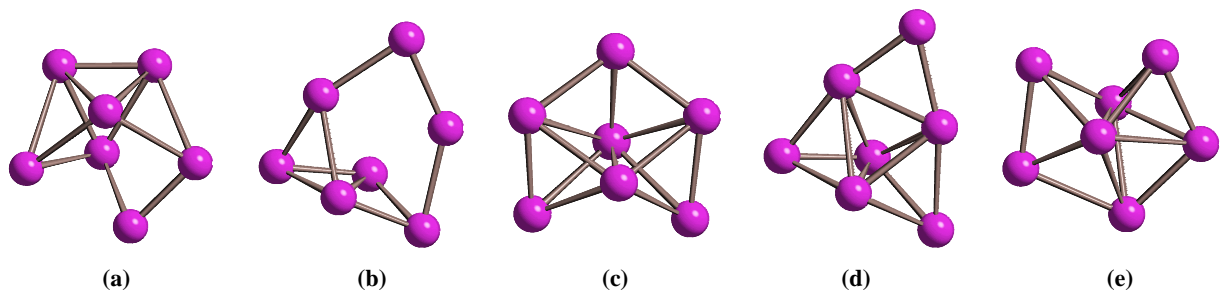


Figure 5.11: Snapshots during the MD simulation of Si_7 cluster at 1600 K: (a) at 23.80 ps (b) at 24.12 ps (c) at 27.58 ps (d) at 28.51 ps (e) at 31.03 ps.

5.1.4 Simulated Annealing of Medium Size Silicon Clusters

In the following subsections two of the most studied medium size silicon clusters, Si_{45} and Si_{60} , are considered.

Structure of Si_{45}

Different starting structures (see Table 5.7) were considered in the simulated annealing runs to find the energy minimum structures of Si_{45} . A preoptimization was performed for the starting structures by a quasi-Newton-Raphson method or MD run without controlling velocities. It was followed by simulated annealing for 11000 steps. All these structures were heated to 2000 K and equilibrated before cooling to 0 K. The starting structures taken for the simulated annealing and the finally obtained structures are shown in Figure 5.12.

To obtain a reasonable starting structure for the clusters Si_9 in Si_{36} -cage and Si_7 in Si_{38} -cage proposed in Ref. [72, 74], the positions of the core atoms were optimized using the Newton-Raphson optimization method keeping the cage fixed. The resulting structure (Figure 5.12f) was then fully relaxed during simulated annealing. In the case of Si_7 in Si_{38} cluster, two types Si_7 cores were considered. One is a triangular prism with a

center atom and the other was a pentagonal bipyramid structure. Optimization of the core atoms gave the same structure for these two cases (Figure 5.12c). The possibility of an elongated structure [92] was also investigated by starting from a stacked cubic structure (Figure 5.12g).

During the simulated annealing of the structure proposed by Jelski et al. [70] (Figure 5.12a) it was found that its Si_{17} core was not undergoing any rearrangement. A substantial distortion of the surface atoms of this cluster was observed. The four capping atoms of the six-membered rings were rearranged. All the other starting structures (Figure 5.12b-g) had undergone large structural changes during the simulated annealing. Binding energies of the final structures obtained after the simulated annealing are given in Table 5.7. The structure derived from that of Jelski et al. [70] was found to

Table 5.7: Binding energies (kJ/mol) of the final structures obtained from MSINDO simulated annealing with different starting structures for Si_{45} .

Starting structure	Final structure	
	Structure	Binding energy
Figure 5.12a	Figure 5.12a'	-16978
Figure 5.12b	Figure 5.12b'	-16926
Figure 5.12c	Figure 5.12c'	-16568
Figure 5.12d	Figure 5.12d'	-16770
Figure 5.12e	Figure 5.12e'	-16813
Figure 5.12f	Figure 5.12f'	-16544
Figure 5.12g	Figure 5.12g'	-16458

be more stable than all the other structures (Figure 5.12a'). The elongated structure (Figure 5.12g') was the least stable one. A general trend seen in these final structures is the preference for compact structures and the formation of more tetracoordinated silicon atoms. This observation is in accordance with that of Kaxiras and Jackson [58].

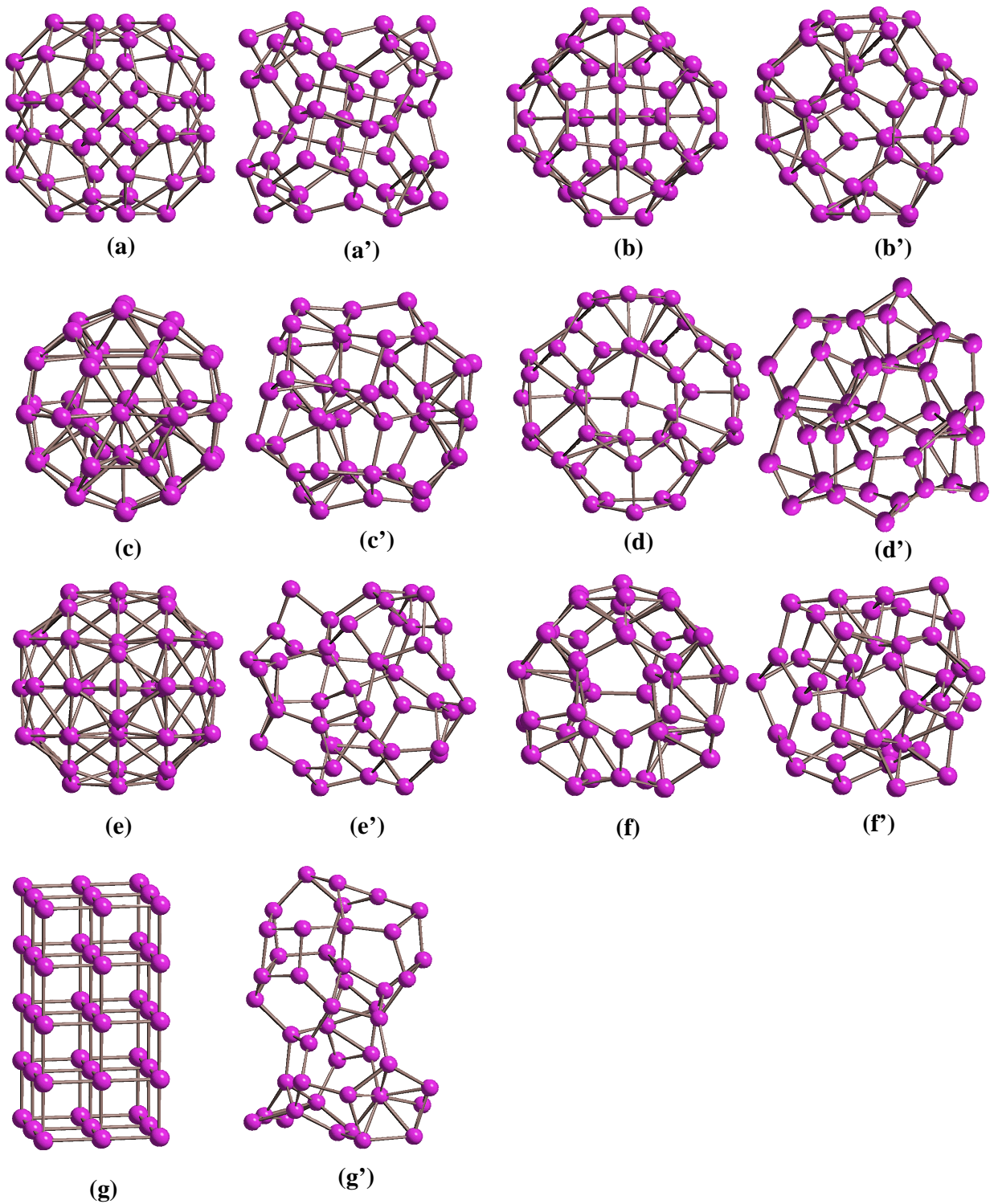


Figure 5.12: Initial structures (without prime) and final structures (with prime) of Si_{45} for simulated annealing; see Table 5.7 for details

Structure of Si₆₀

In the case of Si₆₀, compact (Figure 5.13a,b), fullerene-like (Figure 5.13c) and stacked structures (Figure 5.13d) were considered. The final structures are shown in Figure 5.13a'-d'. Their stability is listed in Table 5.8. The two compact structures were chosen as a three-layer bulk-like structure (Figure 5.13a) and an Si₁₄ core optimized in an Si₄₆ cage (Figure 5.13b). Repeated heating and cooling was done for 22000 steps. The first structure is more compact. The corresponding final structure (Figure 5.13a') turned out to be the most stable one (Table 5.8). Both final structures are of low symmetry.

Table 5.8: Binding energies (BE) (kJ/mol) of the final structures obtained from MSINDO simulated annealing with different starting structures for Si₆₀. Structure in Figure 5.13d' is obtained by a quasi-Newton-Raphson optimization of structure in Figure 5.13d.

Starting structure		Final structure	
Figure	Reference	Figure	BE
Figure 5.13a	-	Figure 5.13a'	-22774
Figure 5.13b	-	Figure 5.13b'	-22581
Figure 5.13c	[76-80]	Figure 5.13c'	-22489
Figure 5.13d	[76]	Figure 5.13d'	-21666

In the case of the fullerene-like I_h structure, the cage was destroyed and a network structure was formed above 1000 K. In order to maintain the cage structure the system was heated only to 1000 K in another simulation. The icosahedral symmetry was destroyed within a few steps of the run. The final structure after the MD run is a distorted cage structure similar to that proposed by Khan et al. [85] (Figure 5.13c'). This structure is higher in energy than the two compact structures (Figure 5.13a',b'). For comparison a parallel stacked naphthalene-like structure of Si₆₀ was optimized using a quasi-Newton-Raphson method. A symmetry restricted optimization gave a stacked structure which was found to be unstable by frequency analysis. A symmetry unrestricted optimization lead to a serious bulging of the edge bonds, showing that Si₆₀ does not prefer such a stacked naphthalene-like structure. This is different from C₆₀ that is stable in the graphite form which is similar to the above mentioned stacked naphthalene structure.

Unlike carbon, silicon prefers to be in tetrahedral coordination. The observed distortion from the I_h structure is driven by the preference of Si atoms to be in a tetrahedral coordinated state. The distortions of the Si_{36} and Si_{38} fullerene cages that are part of several modifications of Si_{45} can also be explained in this way. A structure where most Si atoms are tetrahedrally coordinated will be most stable. Thus one can expect a three-dimensional network structure to be more stable than the cage structure [86]. Si_{60} in cage structure was proposed by the previous first principle calculations. Such high-level calculations were performed to verify the relative energies of the cage-like and bulk-like structure to confirm the MSINDO result. Gradient-based optimizations with the gradient-corrected density functional PWGGA [90] using a 6-311G* basis set were done. The two representative structures for compact and cage shape of Figure 9a' and 9c' obtained by MSINDO were used as starting structures. The compact structure was found to be 440 kJ/mol more stable than the distorted cage structure. This qualitatively confirms the result obtained by MSINDO.

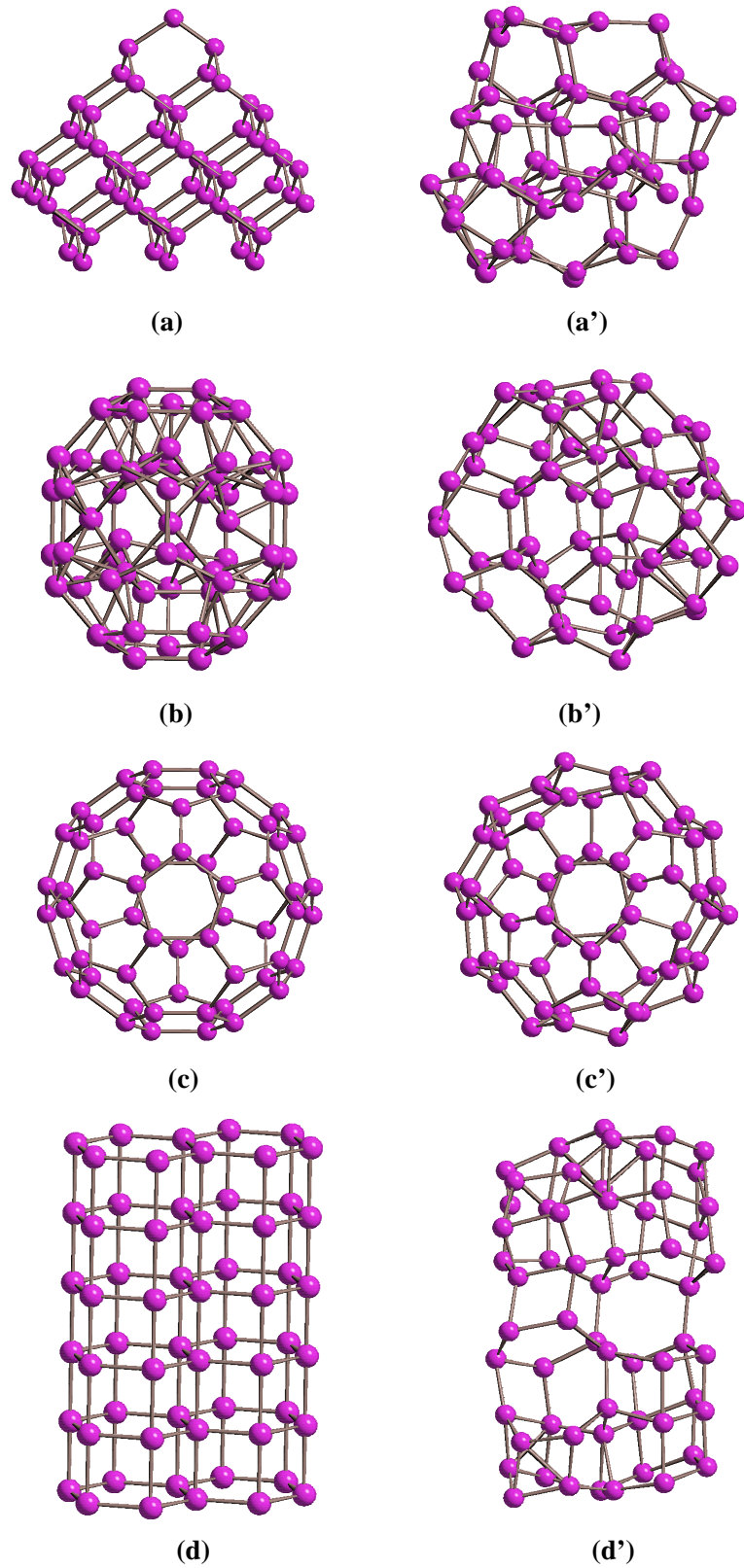


Figure 5.13: Initial structures (without prime) and final structures (with prime) of Si_{60} for simulated annealing; see Table 5.8 for details

5.2 Formation of Vanadia-Titania Catalysts

5.2.1 Introduction

Metal oxides attracted much attention in the past two decades due to their wide range of applications, especially in the field of heterogeneous catalysis [93], for e.g. vanadia-titania catalysts. Vanadia-titania catalysts are used in the selective catalytic reduction (SCR) of nitric oxides with ammonia [94]. In this process nitric oxides produced in technical combustion processes are removed. Vanadia-titania catalysts are also employed for the partial oxidation of hydrocarbons [95,96].

The most abundant polymorphs of titania are rutile and anatase. Rutile is thermodynamically stable, while anatase is metastable. It is found that, monolayer vanadia has a higher catalytic activity on anatase than on rutile in the SCR process. The observed increase of the catalytic activity has been attributed to the match between certain lattice planes of vanadia and anatase [97].

Stable surfaces of anatase are the (101), (001), and (100) surfaces. Using periodic density functional theory (DFT) with local density (LDA) and generalized gradient (GGA) approximation, Lazzeri et al. [98] predicted that the anatase (101) surface is more stable than the other two surfaces. Beltran et al. [99] found that the anatase (001) surface is more stable than the (101) surface with B3LYP hybrid functionals in the periodic DFT. The same conclusion was obtained in a study by Oliver et al. [100] based on classical inter-atomic potentials. The three surfaces have a differently topology and can be expected to react different with the vanadia particles.

Different preparative methods and reaction conditions are believed to affect the structure of the active vanadia species of the mixed catalyst [101,102]. Two common techniques used for the preparation of monolayer vanadium oxide catalyst are impregnation and grafting. In the impregnation technique, a solution containing the active species is adsorbed onto the porous support particles [101]. Impregnating the TiO_2 support with an aqueous solution of ammonium vanadate [103] is an example for this method. In the grafting technique, a monolayer catalyst is formed by the reaction of the active species from the solution with the hydroxyl groups on the surface of the support. An example for this method is the formation of monolayer vanadia catalysts on various oxide surfaces by using a solution of VOCl_3 in CCl_4 or benzene [104].

The term “VO_x” is used for the active vanadia species on the surfaces of metal oxide supports. Various experimental techniques were used for the investigation of the structure of vanadia-titania catalysts [101]. Infrared (IR) and Raman spectroscopy probed the existence of isolated and polymeric vanadia species [105]. Nuclear magnetic resonance (NMR) studies helped to identify different vanadia species with varying vanadium coordination [106]. Extended X-ray adsorption fine structure (EXAFS) and X-ray adsorption near-edge structure (XANES) investigations detected novel vanadia species, for e.g. with divanadyl groups [107]. Many other experimental techniques were also used in understanding the structure and reactivity of this catalyst [102]. The effect of hydration and preparative methods on the structure of the catalyst was also investigated [108].

But to obtain an detailed picture of the structure of the catalyst on an atomic scale, theoretical investigations are necessary. Sayle and co-workers [109] studied the structure of vanadia multi-layers on the anatase (001) surface using classical potentials. Interfaces formed by the interaction of different lattice planes of V₂O₅ with the anatase (001) surface were investigated. Significant deformations were found in the structure of V₂O₅ layers on the anatase (001) surface. But their model was unrealistic as the actual catalyst contains only a monolayer of vanadia particles on the TiO₂ support. Ferreira and Volpe used extended Hückel calculations to predict the structures of different vanadia species on different oxide surfaces [110]. A vanadia-titania catalyst was modeled by the adsorption of a V₂O₅ molecule on the anatase (100) and (001) surfaces by Calatayud et al. [111]. Recently Bredow et al. proposed a model where a V₂O₇H₄ entity was adsorbed on the anatase (100) surface [112]. This model was based on experimental observations of polyvanadate chains with VO₄ units at low vanadia concentration. Adsorption studies of NO, NH₃ and H₂O were performed on this model [113]. The same model was used to investigate the reaction mechanism of SCR of NO with NH₃ [114]. But up to now no theoretical investigation has focused on the influence of the various crystallographic planes of the anatase surfaces on the structure of the vanadia species. No MD simulations were performed in the previous studies to investigate the stability of vanadia species at experimental temperatures. In the study presented here, MD techniques were employed to study the reaction of the (101), (001) and (100) anatase surfaces towards hydrated vanadia species. Stabilities of different isolated and poly-

meric vanadia species were investigated. Reactions of hydroxyl groups on the anatase surfaces with adsorbed vanadia species were also studied here.

5.2.2 Bulk Properties of Anatase

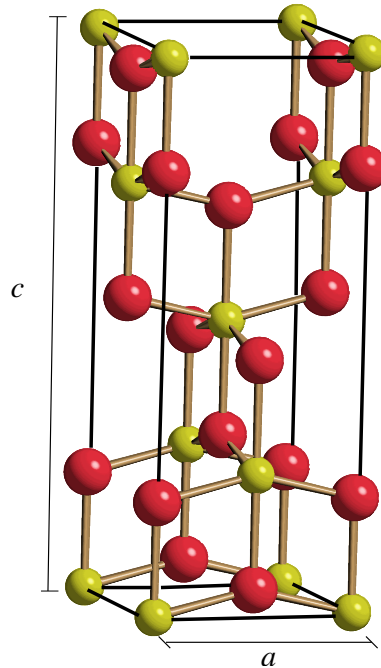


Figure 5.14: Anatase bulk unit cell. Yellow spheres represent titanium atoms and red spheres represent oxygen atoms.

Anatase has a tetragonal unit cell (Figure 5.14). The space group of anatase is $D_{4h}^{19} - I4_1/amd$ [115]. The titanium atoms are surrounded by six oxygen atoms in a distorted octahedral configuration. The stacking of the octahedra results in threefold coordinated oxygen atoms. The tetrahedral structure can be described in terms of three internal parameters a , c and u . Here a and c are the unit cell parameters in x and z directions, respectively, and u is the oxygen fractional coordinate [116]. Experimental values for the lattice parameters ($a = 3.786 \text{ \AA}$, $c = 9.514 \text{ \AA}$ and $u = 0.208$) were reported by Howard et al. [117]. The experimental binding energy per TiO_2 unit for rutile is 1876 kJ/mol [118].

The MSINDO CCM-3D calculation was performed using a $\text{Ti}_{64}\text{O}_{128}$ cluster. In a previous study [23] this cluster was found to give converged bulk properties for a CCM-3D calculation. Unit cell parameters were optimized and bulk properties were

calculated. The optimized lattice parameters are $a = 3.630 \text{ \AA}$, $c = 9.783 \text{ \AA}$ and $u = 0.205$. Lattice parameters a , c , and u deviate only by -4%, 3%, and -1% from the experimental values [117] (see Table 5.9). Compared to the results from previous periodic DFT/B3LYP calculations by Beltran et al. [99], lattice parameters deviates by -3%, 3%, and 1% (Table 5.9). Thus the lattice parameters from MSINDO-CCM calculation are in reasonable agreement with the values reported by previous theoretical calculation and experiment. Binding energy per TiO_2 unit for anatase from MSINDO-CCM calculations is 2065 kJ/mol. It is 189 kJ/mol higher than the experimental value (1876 kJ/mol) [118]. But the deviation from the experimental value is smaller compared to that observed in the previous periodic DFT/LDA calculations [98] (see Table 5.9).

Table 5.9: Bulk properties of anatase

Properties		MSINDO	DFT	Experiment
Unit cell parameters	a (\AA)	3.630	3.735 ^a	3.786 ^c
	c (\AA)	9.783	9.534 ^a	9.514 ^c
	u	0.205	0.203 ^a	0.208 ^c
Binding energy per TiO_2 (kJ/mol)		2065	2358 ^b	1876 ^e

^a Ref. [99]

^b Ref. [98]

^c Ref. [117]

^e Ref. [118]

5.2.3 Surface Properties of Anatase

Anatase is transformed into rutile at relatively low temperatures. Due to this reason, single crystal experiments on anatase are rare and have been performed only recently [115, 119, 120]. Hebenstreit et al. [121] prepared and studied anatase single crystal surfaces by scanning tunneling microscopy (STM). The anatase (101) surface has a sawtooth like structure (Figure 5.15a). Six- and five-fold coordinated titanium atoms and three- and two-fold coordinated oxygen atoms are present on this surface. The anatase (001) surface exhibits five-fold coordinated titanium atoms as well as two- and three-fold coordinated oxygen atoms (Figure 5.15b). Hermann et al. [122] found that

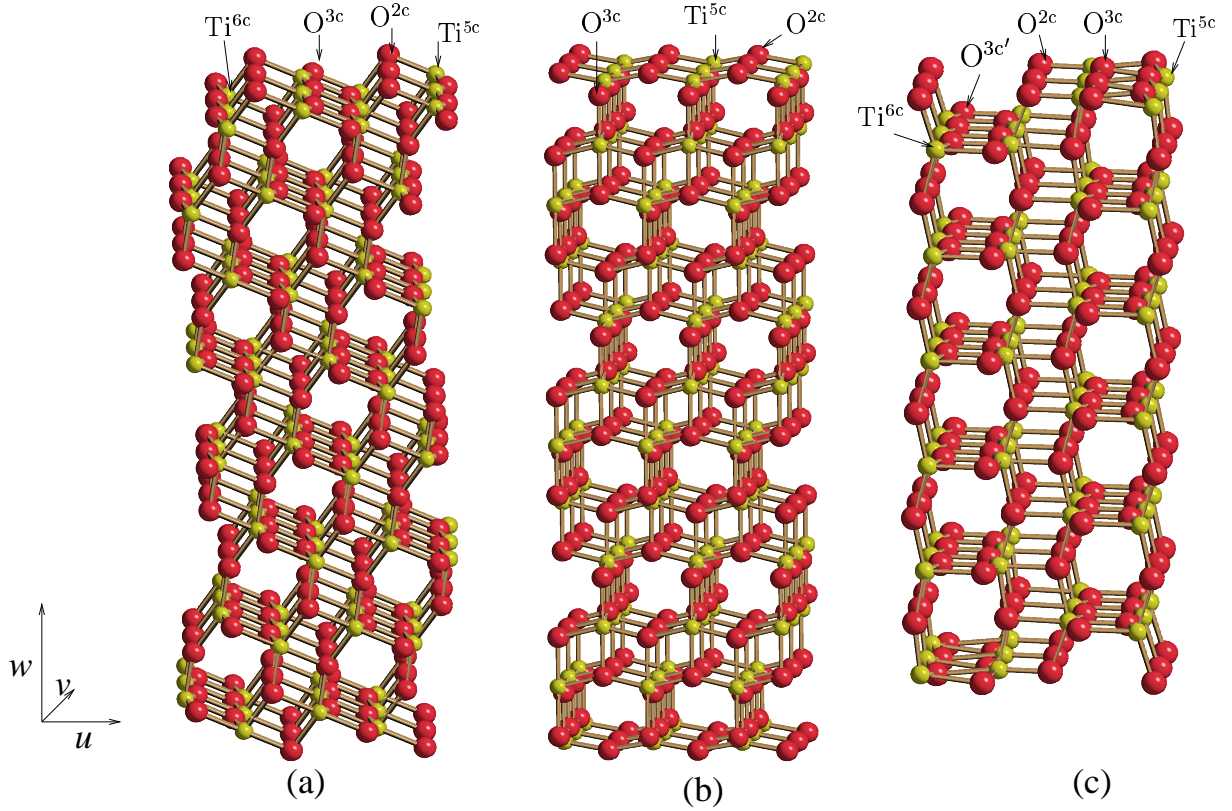


Figure 5.15: Clusters used for studying the surface relaxations of anatase surfaces. (a) anatase (101) $1 \times 3 \times 1$ ($\text{Ti}_{96}\text{O}_{192}$) cluster. $u = [10\bar{1}]$, $v = [010]$, $w = [101]$. (b) anatase (001) $1 \times 3 \times 3$ ($\text{Ti}_{108}\text{O}_{216}$) cluster. $u = [100]$, $v = [010]$, $w = [001]$. (c) anatase (100) $1 \times 3 \times 6$ ($\text{Ti}_{72}\text{O}_{144}$) cluster. $u = [001]$, $v = [0\bar{1}0]$, $w = [100]$.

the anatase (001) 1×1 surface is not stable and undergoes reconstruction on heating to elevated temperatures. On the anatase (100) surface, five-fold coordinated titanium atoms, three- and two-fold coordinated oxygen atoms are exposed (Figure 5.15c). In the channels along the $[010]$ direction, six-fold titanium atoms and three-fold oxygen atoms are also present.

Surface relaxation of the anatase (101), (001) and (100) surfaces was studied using MSINDO. For simulating anatase (101), (001), and (100) surfaces, two-dimensional cyclic $\text{Ti}_{96}\text{O}_{192}$, $\text{Ti}_{108}\text{O}_{216}$, and $\text{Ti}_{72}\text{O}_{144}$ clusters were chosen, respectively. Surface energies of the three surfaces and their convergence with the number of relaxed layers (on each side of the slab) are given in Table 5.10. The surface energy E_{surf} is calculated

according to the equation

$$E_{\text{surf}} = \frac{E_{\text{slab}} - E_{\text{bulk}}}{2A} \quad (5.82)$$

where E_{slab} is the total energy from a two-dimensional cyclic cluster calculation, E_{bulk} is the total energy from a three-dimensional cyclic cluster calculation per TiO_2 unit multiplied by the number of TiO_2 units in the slab and A is the surface area of the slab. In the present calculations, E_{bulk} is calculated by multiplying the total energy per TiO_2 unit for $\text{Ti}_{64}\text{O}_{128}$ three-dimensional cyclic cluster with the number of TiO_2 units in the slab. Surface energies are almost converged on relaxing 9, 9 and 5 layers for (101)- $\text{Ti}_{96}\text{O}_{192}$, (001)- $\text{Ti}_{108}\text{O}_{216}$ and (100)- $\text{Ti}_{72}\text{O}_{144}$ clusters, respectively.

Table 5.10: Surface energies E_{surf} for various anatase surfaces. N_{rlx} is the number of atomic layers relaxed in both sides of the cluster (see Figure 5.15) and E_{surf} is the surface energy in (J/m^2).

Surface	MSINDO			DFT/LDA ^a
	Cluster	N_{rlx}	E_{surf}	E_{surf}
(101)	$\text{Ti}_{96}\text{O}_{192}$	6	1.34	0.84
		7	1.33	
		8	1.32	
		9	1.31	
(001)	$\text{Ti}_{108}\text{O}_{216}$	6	1.37	1.38
		7	1.36	
		8	1.36	
		9	1.36	
(100)	$\text{Ti}_{72}\text{O}_{144}$	2	1.60	0.96
		3	1.54	
		4	1.52	
		5	1.51	

^a Ref. [98]

According to the surface energies obtained with MSINDO (Table 5.10), the order of increasing stability of anatase surfaces is (100) < (001) < (101). Lazzeri et al. [98]

reported that the stability increases with $(001) < (100) < (101)$ while DFT/B3LYP calculations by Beltrán et al. [99] and the simulations using classical potentials by Oliver et al. [100] resulted in the order of increasing stability is $(100) < (101) < (001)$. Results of MSINDO and the calculations of Lazzeri et al. [98] agree on the fact that the (101) plane is the most stable anatase surface. This was also observed in the experiments [115]. Absolute values of surface energies for (101) and (100) surfaces calculated by DFT [98] are lower than the MSINDO values. The reason for this might be that the DFT gives a very covalent picture of the surface bonds with strong relaxation.

The changes of atomic positions with respect to the corresponding bulk structure are given in Table 5.11. The number of relaxed layers on either side of the slabs were 9, 9, and 5 for anatase (101), (001) and (100) clusters, respectively. The results are compared with previous DFT/LDA calculation by Lazzeri et al. [98].

Table 5.11: Relaxation of anatase surfaces; changes Δu , Δv and Δw (Å) of atomic coordinates with respect to the corresponding bulk positions (see Figure 5.15)

Surface	Cluster	Atom	Relaxations					
			MSINDO			DFT/LDA ^a		
			Δu	Δv	Δw	Δu	Δv	Δw
(101)	Ti ₉₆ O ₁₉₂ (Figure 5.15a)	Ti ^{5c}	0.25	0.00	0.00	0.02	0.00	-0.18
		Ti ^{6c}	0.25	0.00	0.07	0.17	0.00	0.20
		O ^{2c}	0.06	0.00	-0.14	0.29	0.00	-0.02
		O ^{3c}	0.13	0.00	0.29	0.16	0.00	0.19
(001)	Ti ₁₀₈ O ₂₁₆ (Figure 5.15b)	Ti ^{5c}	0.05	0.00	0.04	0.04	0.00	-0.06
		O ^{2c}	-0.06	0.00	-0.01	-0.19	0.00	0.08
		O ^{3c}	-0.04	0.00	0.13	-0.17	0.00	-0.02
(100)	Ti ₇₂ O ₁₄₄ (Figure 5.15c)	Ti ^{5c}	0.06	0.00	-0.04	0.02	0.00	-0.04
		Ti ^{6c}	0.00	0.00	0.05	0.01	0.00	0.17
		O ^{2c}	0.17	0.00	-0.02	0.16	0.00	0.02
		O ^{3c}	0.05	0.00	0.18	0.04	0.00	0.18
		O ^{3c'}	0.00	0.00	0.04	0.01	0.00	0.10

^a Data from Ref. [98]

In the case of the (101) surface, there is a quantitative difference between the DFT results and the MSINDO results in the surface relaxations. However, the directions of

the displacements are the same. For the (001) surface, changes Δw for all the surface atoms are in opposite direction compared to the DFT results. Except the displacements of two-fold coordinated oxygens, the relaxation of the (100) is in good agreement with the DFT results.

5.2.4 Models of VO_x/TiO_2 Catalysts

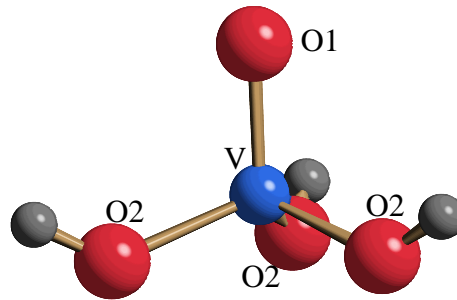


Figure 5.16: Structure of VO_4H_3 molecule. Blue sphere represents vanadium atom, red spheres represent oxygen atom and grey spheres represent hydrogen atoms

VO_x/TiO_2 catalysts are modeled by the adsorption of VO_4H_3 and $\text{V}_2\text{O}_7\text{H}_4$ on the anatase (101), (001) and (100) clean surfaces. VO_4H_3 and its dimer $\text{V}_2\text{O}_7\text{H}_4$ are the simplest realistic models to understand the structures of the VO_x/TiO_2 catalysts. In VO_4H_3 vanadium is tetrahedrally coordinated. In many of the preparative methods the starting materials have vanadium in tetrahedral coordination [101,102]. In aqueous medium, vanadium species will get hydrated. Different types of hydrated species are possible depending on the pH of the medium [108]. Hydration is also possible by atmospheric water and from water molecules adsorbed on titanium dioxide [106,108]. There is experimental evidence for the presence of a hydrated VO_x species on the TiO_2 support [106,123,124]. Ferreira and Volpe [110] have also used VO_4H_3 as a model in their simulations.

Three different $\text{Ti}_{36}\text{O}_{72}$ clusters were used for modeling the (101), (001) and (100) anatase surfaces. These clusters are shown in Figure 5.17. Only one side of these clusters was relaxed during the simulations. For the (101) and (001) clusters the first six atomic layers and for the (100) cluster the first three atomic layers were relaxed. The cluster used to simulate the (101) surface does not have a complete repeating unit

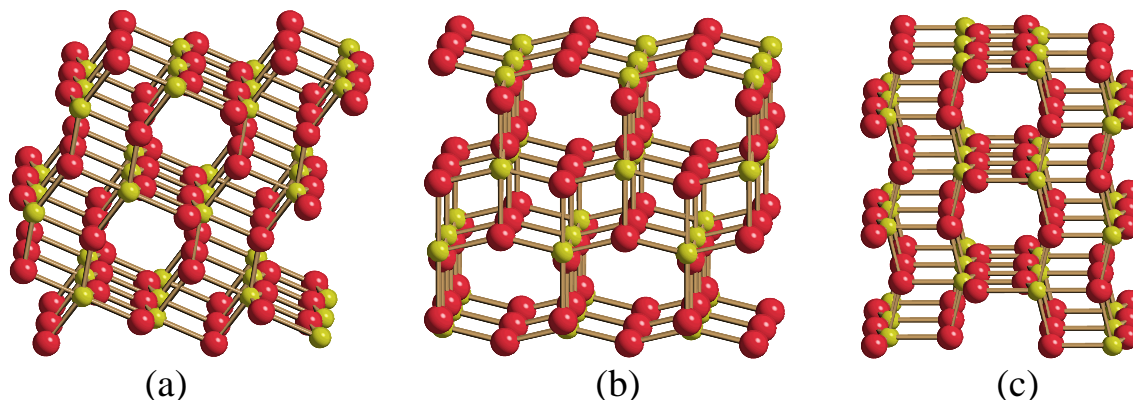


Figure 5.17: TiO_2 clusters ($\text{Ti}_{36}\text{O}_{72}$) used for modeling VO_x/TiO_2 catalysts. (a) anatase (101) (b) anatase (001) (c) anatase (100)

in the [101] direction. As shown in Figure 5.15a, the (101) cluster with a complete unit cell along w direction has the stoichiometry $\text{Ti}_{96}\text{O}_{192}$. With the available computers, it is impossible to use this cluster in MD simulations. Because of this reason, the smaller cluster $\text{Ti}_{36}\text{O}_{72}$ was chosen. But it was found that error due to the use of $\text{Ti}_{36}\text{O}_{72}$ cluster instead of $\text{Ti}_{96}\text{O}_{192}$ was dispensable. For e.g., adsorption energy for molecular adsorption of water molecule on $\text{Ti}_{96}\text{O}_{192}$ and $\text{Ti}_{36}\text{O}_{72}$ clusters were 95 kJ/mol and 99 kJ/mol, respectively.

5.2.5 Adsorption of VO_4H_3 on Anatase Surfaces

The results of the simulations of VO_4H_3 adsorption on the anatase (101), (001) and (100) are described in sections 5.2.5.1, 5.2.5.2 and 5.2.5.3, respectively. In Section 5.2.5.4 the results are discussed and compared with available literature data.

5.2.5.1 Anatase (101)

In a first step, VO_4H_3 was adsorbed molecularly on the anatase (101) surface. An adsorption structure shown in Figure 5.18a was considered first. In this structure two oxygen atoms of VO_4H_3 are bound to two neighboring five-fold coordinated surface titanium atoms. One of the hydrogen atoms of VO_4H_3 , H(1), is connected to the bridging surface oxygen O(5) by a hydrogen bond. The adsorption energy for this structure is -125 kJ/mol. The energy of the system further decreases by 25 kJ/mol, if the proton moves to the bridging surface oxygen atom O(5) (see Figure 5.18b). The

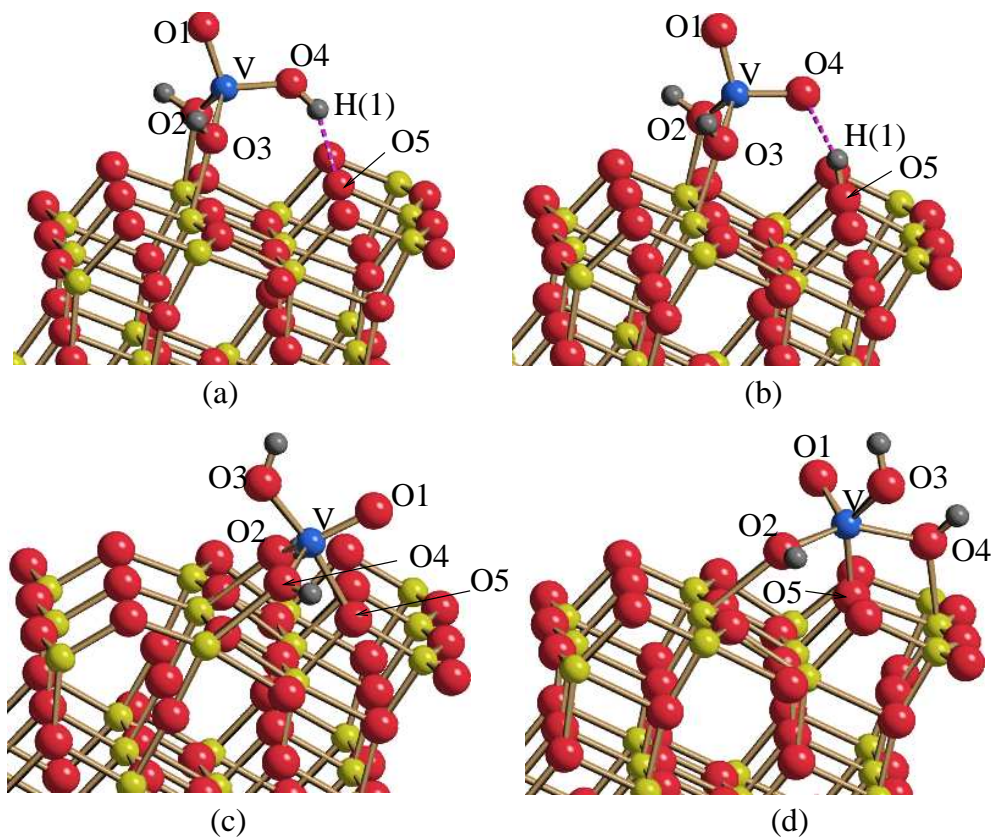


Figure 5.18: Different structures of VO_4H_3 on the anatase (101) surface. Dotted lines indicate hydrogen bonds. Here blue, yellow, red and grey spheres represent vanadium, titanium, oxygen and hydrogen atoms, respectively. The same color scheme is used throughout this section.

optimized lengths of all vanadium-oxygen bonds in the adsorbate structure are given in Table 5.12. The bond lengths of two vanadyl bonds in structure (5.18b), V-O(4) and V-O(1), are 1.61 Å and 1.60 Å, respectively. The former bond is slightly longer because it is involved in a hydrogen bond to H(1).

Two other adsorption structures were tested in which the vanadium atom is directly bound to the bridging oxygen O(5) (Figure 5.18 c, d). The structure (5.18c) is 4 kJ/mol higher in energy than structure (5.18b). The structure (5.18d) turned out to be the most stable among all the structures in Figure 5.18. This structure is 5 kJ/mol more stable than the dissociated structure (5.18b). Vanadium is five-fold coordinated and the VO_4 tetrahedron of the VO_4H_3 molecule is distorted in this structure. The adsorbate partially forms a continuation of the crystal surface. Optimized bond lengths of all vanadium-oxygen bonds present in these two structures are given in Table 5.12.

Table 5.12: Adsorption energies E_{ads} (kJ/mol) and vanadium-oxygen bond lengths (\AA) of different structures obtained by the adsorption VO_4H_3 on the anatase (101) surface.

Structure	E_{ads}	Bond length				
		V-O1	V-O2	V-O3	V-O4	V-O5
Figure 5.18a	-125	1.58	1.76	1.77	1.71	-
Figure 5.18b	-150	1.60	1.83	1.84	1.61	-
Figure 5.18c	-146	1.59	1.81	1.74	1.81	-
Figure 5.18d	-155	1.59	1.82	1.76	1.93	1.81

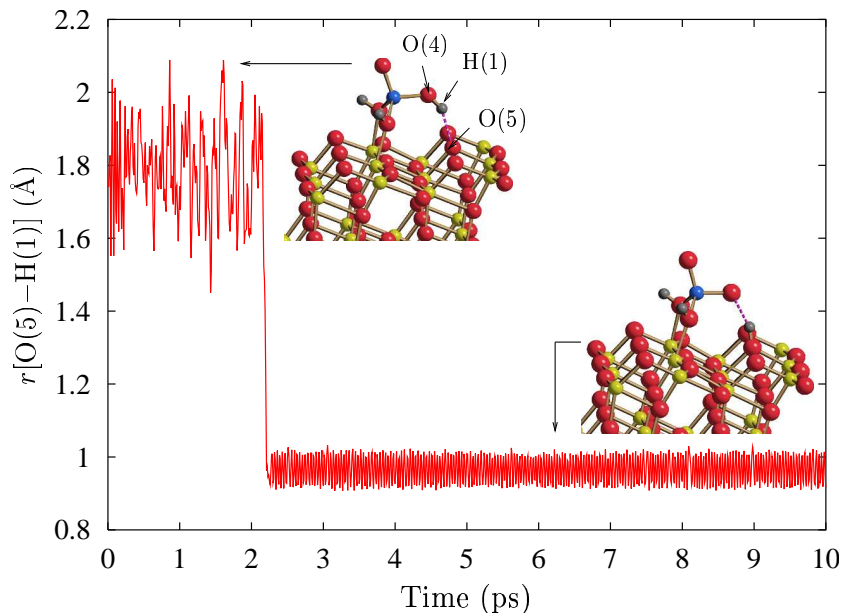


Figure 5.19: Distance $r[\text{O}(5) - \text{H}(1)]$ between the oxygen O(5) and hydrogen H(1) during the MD simulation at 300 K (see Figure 5.18a for labeling)

To investigate the stability of these structures at high temperatures, constant temperature MD simulations were performed at 300 K for 10 ps. The Nosé-Hoover chain (NHC) thermostat was used for controlling the temperature during these simulations. The frequency ω of the thermostat (Eq. 3.74) was set to 3600 cm^{-1} , which is close to the maximum frequency of vibration of the system. The same procedure was used for all constant temperature MD simulations presented in this section. The optimized

structure (5.18a) was used as starting point for the MD simulation. Within 2.2 ps, the O(4)-H(1) bond was broken and the hydrogen was transferred to the bridging surface atom O(5). The structure (5.18a) must therefore be considered as only metastable with respect to (5.18b). The distance between the bridging oxygen and the proton of the adsorbate ($r[\text{O}(5) - \text{H}(1)]$) during this MD simulation is shown in Figure 5.19. The dissociated structure remained stable during the rest of the simulation for 10 ps. But no transformation from (5.18b) to (5.18d) was observed. Another MD simulation for 10 ps at 300 K was performed starting with structure (5.18d). No remarkable structural rearrangements occurred during this simulation. This structure is therefore stable at room temperature. As a conclusion, both structures (5.18b) and (5.18d) are stable at room temperature and may coexist.

5.2.5.2 Anatase (001)

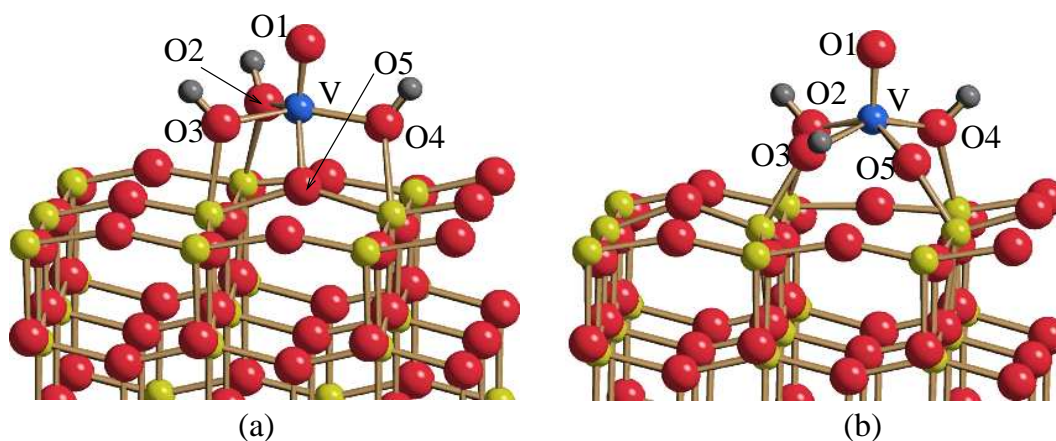


Figure 5.20: Different structures of VO_4H_3 on the anatase (001) surface

On the anatase (001) surface, three oxygen atoms of VO_4H_3 can bind to three five-coordinated surface titanium atoms as shown in Figure 5.20a. The VO_4 tetrahedron is distorted by the adsorption due to the interaction with the surface and a bond between the vanadium atom and surface oxygen O(5) is formed. The adsorption energy is -294 kJ/mol .

An MD simulation was performed at 300 K starting from structure (5.20a). After a few steps of the simulation, the two-fold coordinated surface oxygen O(5) to which the vanadium atom was connected, moved out from its lattice position and structure

Table 5.13: Adsorption energies E_{ads} (kJ/mol) and vanadium-oxygen bond lengths (\AA) of two structures obtained by the adsorption VO_4H_3 on anatase (001) surface.

Structure	E_{ads}	Bond length (\AA)				
		V-O1	V-O2	V-O3	V-O4	V-O5
Figure 5.20a	-294	1.60	1.80	1.86	1.84	1.79
Figure 5.20b	-450	1.59	1.82	1.94	1.83	1.73

(5.20b) was formed. The displacement Δr of the oxygen atom O(5) from its lattice position during the simulation process is shown in Figure 5.21. The oxygen atom

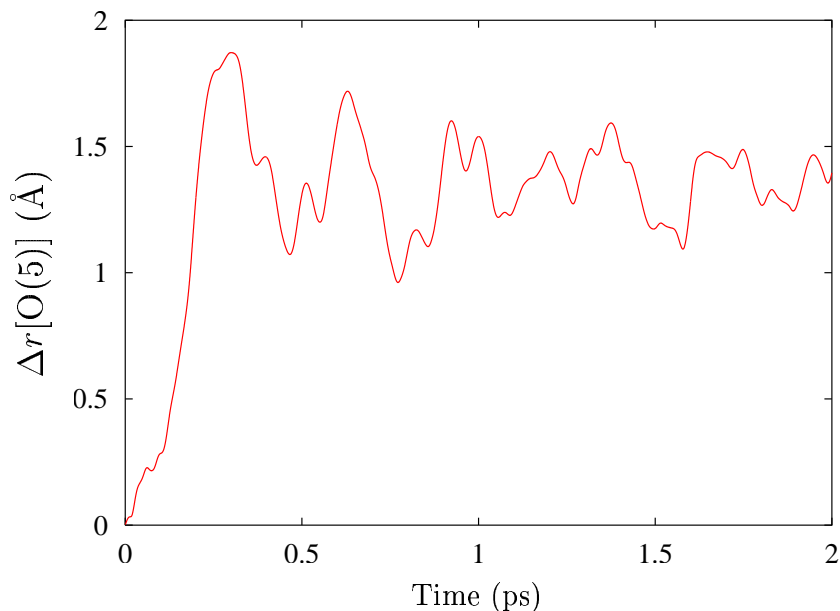


Figure 5.21: Displacement Δr from the regular lattice position of the surface oxygen O(5), which is bound to the vanadium atom (see Figure 5.20a).

moved by 1.3 to 1.5 \AA from its lattice position during the dynamics simulation. The final structure (5.20b) is about 156 kJ/mol more stable than structure (5.20a). The V=O(1) bond length slightly decreased (by 0.01 \AA), while the bond lengths of the other two V-O bonds increased (see Table 5.13). The V-O(4) bond decreased by 0.01 \AA and V-O(5) bond became shorter from 1.79 \AA to 1.73 \AA after the rearrangement. No further change in the structure was observed during the rest of the MD simulation

for 10 ps. This shows that the structure (5.20b) is stable at 300 K.

5.2.5.3 Anatase (100)

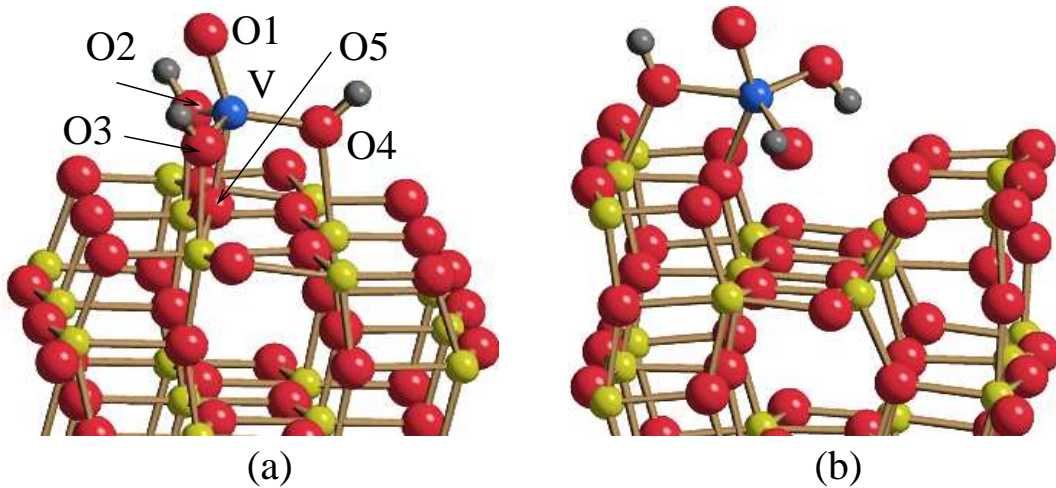


Figure 5.22: Different structures of VO_4H_3 on the anatase (100) surface

On the anatase (100) surface three oxygen atoms of VO_4H_3 can bind to three five-fold coordinated titanium atoms on the surface without significant distortion of the tetrahedral structure (see Figure 5.22a). In the optimized structure the vanadyl V-O(1) bond is slightly tilted (≈ 20 degrees) from the surface normal. The vanadium atom is bound to one of the three-fold coordinated surface oxygens. This oxygen atom O(5) is slightly displaced out of the surface. The V-O(1) bond length is 1.59 Å, the vanadium to surface oxygen bond length V-O(5) is 1.88 Å (see Table 5.14).

Table 5.14: Adsorption energy E_{ads} (kJ/mol) and vanadium-oxygen bond lengths (Å) of the most stable structure which is obtained by the adsorption VO_4H_3 on the anatase (100) surface.

Structure	E_{ads}	Bond length				
		V-O1	V-O2	V-O3	V-O4	V-O5
Figure 5.22a	- 231	1.59	1.81	1.81	1.77	1.88

The anatase (100) surface has channels along the [010] direction. In an alternative

structure VO_4H_3 was adsorbed in such a way that the vanadium atom is directly connected to one of the two-coordinated oxygens exposed at the edges of the channel (see Figure 5.22b). This structure is found to be 104 kJ/mol higher in energy than the structure in Figure 5.22a.

An MD simulation at 300 K was performed by starting with the energy minimum structure (Figure 5.22a) for 10 ps. This structure did not undergo any significant changes during that simulation and is therefore stable.

5.2.5.4 Discussion

Different types of bonding environments are present on the three different surfaces of anatase. The topology of the surface determines the structure of the vanadia species after adsorption. In most of the stable structures formed by the adsorption of VO_4H_3 on the three anatase surfaces, vanadium atoms are five-fold coordinated. Using ultraviolet-visible-near infrared spectroscopy, Larrubia and Busca reported that vanadium in vanadium oxide species on the supported catalysts has lower coordination than in bulk vanadia, possibly four or five [125].

Only on the anatase (101) surface, an undistorted tetrahedral VO_4 environment is possible, as shown in Figure 5.18b. Even though the adsorption shown in Figure 5.18d is the most stable one, the structures (5.18b) and (5.18c) might coexist under experimental conditions. On the basis of an EXAFS/XANES analysis, Kozłowski et al. [107] predicted a structure similar to that in Figure 5.18b. In a secondary ion mass spectroscopic (SIMS) experiment Bond et al. [126] observed ions of type $\text{V}_x\text{O}_y\text{H}^+$. This was believed to originate from a species containing $\text{VO}(\text{OH})$ groups. They used structure (5.18a) as the basis of their interpretation. But structure (5.18d) can also be the source for producing $\text{V}_x\text{O}_y\text{H}^+$ ions. ^1H and ^{51}V high-resolution solid state NMR studies also predicted structures with $\text{VO}(\text{OH})$ groups [106].

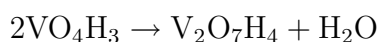
A distorted square-pyramidal structure type was found for the monomeric vanadia species on the anatase (001) surface. The formation of a VO_5H_3 species is connected with the formation of an oxygen vacancy on the anatase surface. A similar bonding situation with square pyramidal VO_5 units exists in the vanadium pentoxide (001) surface. The observed decrease in energy due to this rearrangement might be due to the formation of a less strained structure. A direct experimental evidence for the

structure on the (001) surface could not be found in the literature. But there are some experimental observations, which can be connected to the findings of this work. By electrical conductivity measurements Herrmann [127] found that the concentration of anionic vacancies in the TiO_2 support increases with increasing vanadia loading. This might be due to the interaction of the surface oxygen with the adsorbate as discussed in Section 5.2.5.2. Moreover, Went et al. [128] predicted VO_x species of type $\text{O}=\text{V}(\text{O})_4$ in square-pyramidal structure on the anatase (001) surface. This interpretation was based on the data obtained from *in situ* laser Raman spectroscopy [128, 129] and NMR spectroscopy [130] experiments. This supports the structure in Figure 5.20b. On comparing the adsorption energy of VO_4H_3 on the three surfaces, it is clear that adsorption is more favorable on the anatase (001) surface than on the (100) and the (101) surfaces.

The tetrahedral structure of the adsorbate is almost preserved on the (100) surface. In most of the spectroscopic analysis of the VO_x/TiO_2 catalysts, there is clear evidence that the monomeric VO_x species has tetrahedral coordination. Many experimental groups confirmed the existence of VO_4 tetrahedra, with three oxygens connected to the surface titanium atoms [105, 125, 131–133]. They assumed a structure similar to the one observed on the anatase (100) surface (Figure 5.22).

5.2.6 Adsorption of $\text{V}_2\text{O}_7\text{H}_4$ on Anatase Surfaces

In this section the results of the $\text{V}_2\text{O}_7\text{H}_4$ adsorption on the three anatase surfaces are presented. Several experimental studies have reported the formation of polyvanadates on the TiO_2 surface at higher vanadia concentration [101]. Polyvanadates can be formed before reaching the surface or by condensation reactions on the surface. It was assumed that the following reaction occurred between two VO_4H_3 molecules before or after adsorption.



5.2.6.1 Anatase (101)

Two different structures of $\text{V}_2\text{O}_7\text{H}_4$ on the anatase (101) surface were studied. They are shown in Figure 5.23. The structure (5.23a) is related to structure (5.18b). In

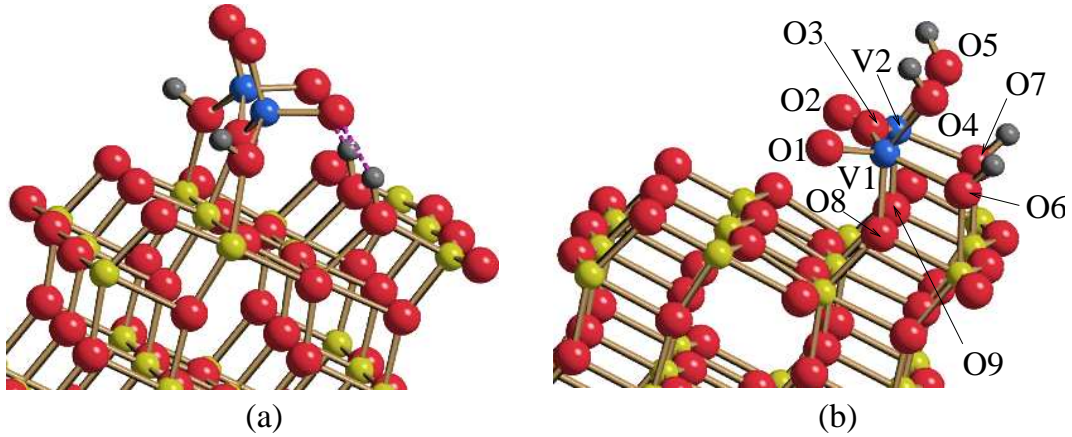


Figure 5.23: Different structures of $V_2O_7H_4$ on the anatase (101) surface

structure (5.23b) the $V_2O_7H_4$ molecule is bound to the surface in such a way that it partially forms the continuation of the anatase crystal structure in [100] direction. This structure is 63 kJ/mol more stable than the structure in Figure 5.23a. The adsorption energy is -376 kJ/mol. Vanadium-oxygen bond lengths of this structure are given in Table 5.15.

Table 5.15: Adsorption energy E_{ads} (kJ/mol) and vanadium-oxygen bond lengths (\AA) of the energy minimum structure of $V_2O_7H_4$ adsorbed on the anatase (101) surface.

Structure	E_{ads}	Bond	Bond length
Figure 5.23b	-376	V1-O1, V2-O2	1.60
		V1-O3, V2-O3	1.73
		V1-O4, V2-O5	1.76
		V1-O6, V2-O7	1.96
		V1-O8, V2-O9	1.83

An MD simulation was performed by starting with structure (5.23b) for 10 ps. No noticeable structural distortion occurred within this time scale. This structure is therefore stable at this temperature.

5.2.6.2 Anatase (001)

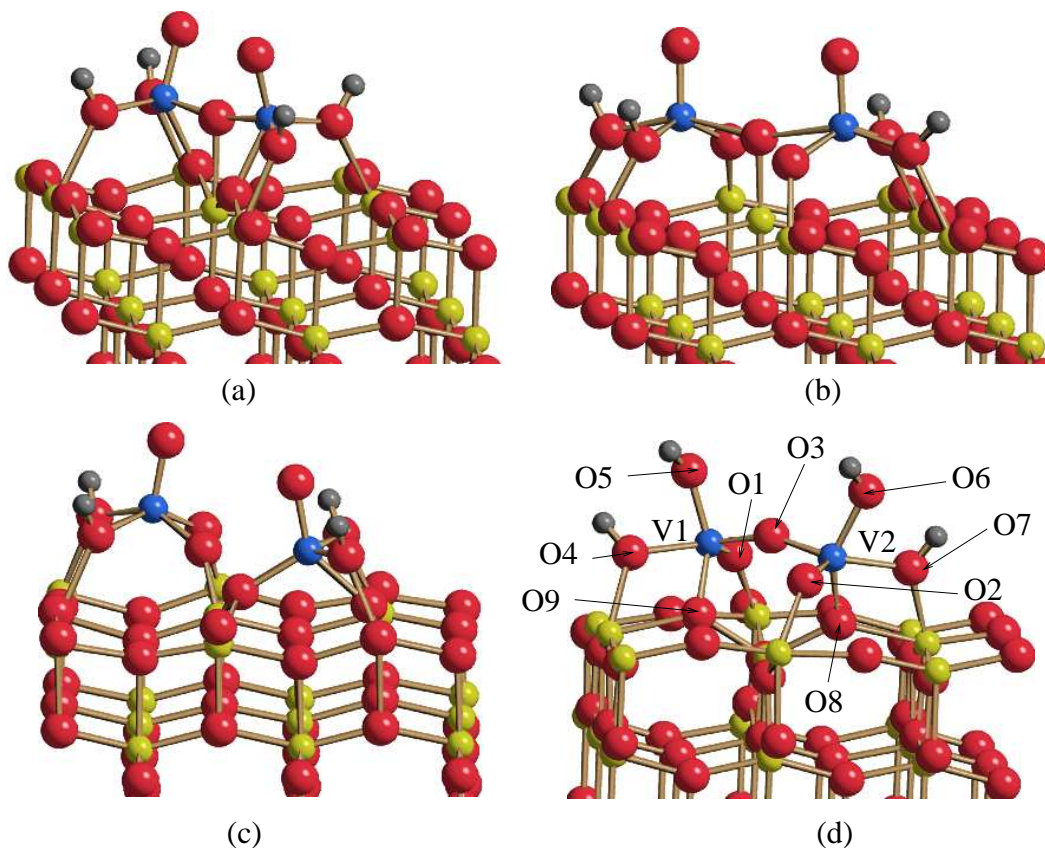


Figure 5.24: Different structures of $V_2O_7H_4$ on anatase (001) surface

Different adsorption structures of $V_2O_7H_4$ on the (001) surface are shown in Figure 5.24. In structure (5.24a), the V-V axis in the adsorbate is oriented along the $[1\bar{1}0]$ direction. The two vanadium atoms are five-fold coordinated. In this structure, the dihedral angle between two V=O groups is 35 degrees. The oxygen O(3) which is bridging the two V atoms is connected to one of the surface titanium atoms. In the case of VO_4H_3 adsorption on this surface, the surface oxygen atom bound to vanadium was displaced from its lattice position with the formation of a distorted square-pyramidal structure (5.20b). A similar type of adsorption structure was investigated in the case of $V_2O_7H_4$ adsorption, by constructing a model with two oxygens displaced from their lattice positions (see Figure 5.24b) with the formation of two corner-shared distorted square-pyramidal structure. But this possibility is ruled out since a fragmentation of the adsorbate into VO_5H_2 and VO_4H_2 occurred during the geometry optimization of this structure and structure (5.24c) was obtained.

In order to investigate the stability of structure (5.24a), an MD simulation at 300 K was performed for 10 ps. During that simulation the starting structure rearranged and structure (5.24d) was obtained. In this structure, the two vanadyl bonds V(1)-O(1) and V(2)-O(2) are connected to two five-fold coordinated surface titanium atoms and the two V-OH bonds V(1)-O(5)H and V(2)-O(6)H are pointing upwards. After this rearrangement the coordination of the oxygen atom O(3), which was forming the V-O-V bond, changed from three to two. The five-fold coordinated titanium atom just below this oxygen atom moved downwards by around 0.4 Å. The whole rearrangement occurred within 2 ps of the simulation. Structure (5.24d) then remained stable during the rest of the simulation. It is 82 kJ/mol lower in energy than structure (5.24a). The calculated adsorption energy and bond lengths of this structure are given in Table 5.16.

Table 5.16: Adsorption energy E_{ads} (kJ/mol) and vanadium-oxygen bond lengths (Å) of the most stable structure of $\text{V}_2\text{O}_7\text{H}_4$ adsorbed on the anatase (001) surface.

Structure	E_{ads}	Bond	Bond length
Figure 5.24d	- 439	V1-O1	1.63
		V2-O2	1.63
		V1-O3	1.75
		V2-O3	1.73
		V1-O4	1.91
		V1-O5	1.74
		V2-O6	1.76
		V2-O7	1.92
		V2-O8	1.81
		V1-O9	1.80

5.2.6.3 Anatase (100)

Three possible adsorption structures of $\text{V}_2\text{O}_7\text{H}_4$ on the (100) surface are shown in Figure 5.25. In structure (5.25a), the bridging oxygen, O(3), in the V-O-V bond is connected to a five-fold coordinated titanium atom. The two vanadyl bonds, V(1)-

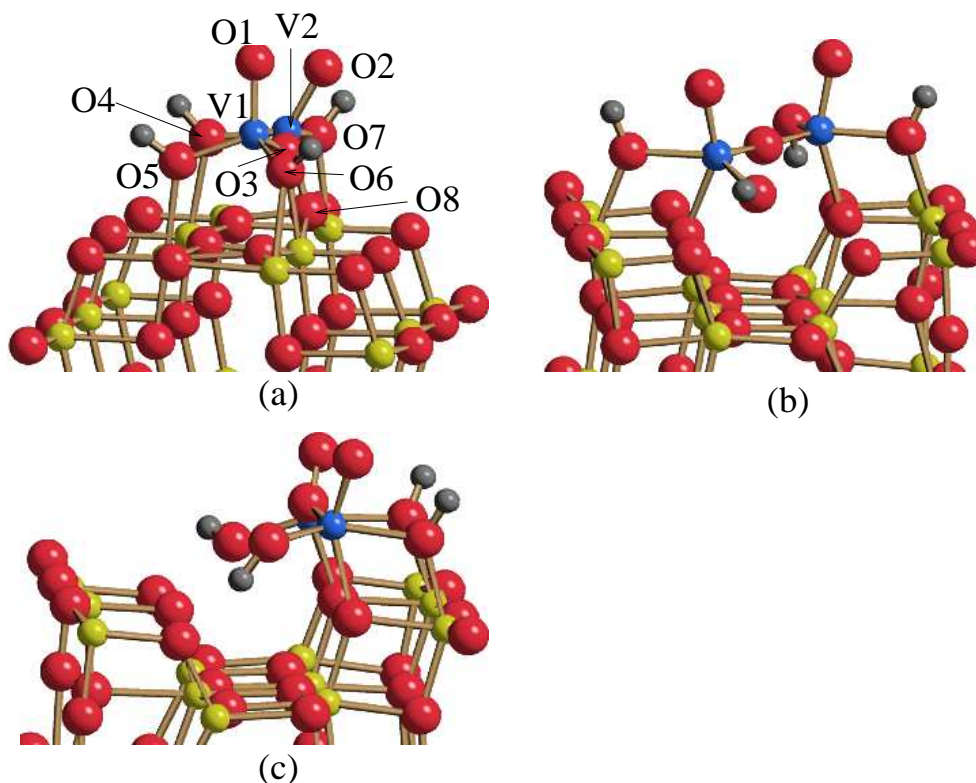


Figure 5.25: Different structures of $V_2O_7H_4$ on the anatase (100) surface

O(1) and V(2)-O(2), are tilted in opposite directions from the surface normal. Two other possible structures, where $V_2O_7H_4$ is adsorbed at the channels on the (100) surface, were also investigated (see Figure 5.25b, Figure 5.25c). In structure (5.25b), the $V_2O_7H_4$ is bridging across the channel, while the $V_2O_7H_4$ group is adsorbed on one side of the channel in structure (5.25c). But structures (5.25b) and (5.25c) are 71 kJ/mol and 79 kJ/mol less stable than structure (5.25a), respectively.

Starting from structure (5.25a), an MD simulation was performed at 300 K for 10 ps. The structure remained stable during the whole simulation which indicates that it is possibly the global minimum structure. The optimized values of vanadium-oxygen bond lengths of this structure are given in Table 5.17.

5.2.6.4 Discussion

The most stable structures obtained for the $V_2O_7H_4$ adsorption on the anatase surfaces contain V-O-V bridging groups. $V_2O_7H_4$ prefers to form a continuation of the crystal structure on the anatase (101) surface. On the anatase (001) surface, no vanadyl

Table 5.17: Adsorption energy E_{ads} (kJ/mol) and optimized vanadium-oxygen bond lengths (\AA) of the most stable structure (5.25a)

Structure	E_{ads}	Bond	Bond length
Figure 5.25a	– 315	V1-O1	1.59
		V2-O2	1.60
		V1-O3	1.71
		V2-O3	1.88
		V1-O5	1.77
		V2-O4	1.77
		V1-O6	1.78
		V2-O7	1.83
		V2-O8	1.79

groups are present in the adsorbed VO_x species. For this reason $\text{V}_2\text{O}_7\text{H}_4$ on the anatase (001) surface might be less catalytically active than on the other surfaces. Similar to the VO_4H_3 adsorption, a slightly distorted tetrahedral structure is formed during the adsorption of $\text{V}_2\text{O}_7\text{H}_4$ on the (100) surface. Adsorption at channels on the (100) surface is not favorable.

Raman and IR studies were used to probe the presence of V-O-V bridging groups by their bending bands in the region of 820 cm^{-1} [105,128]. The V=O and V-OH groups were also identified by experiments [106]. From the observation of V_2O_x fragments in SIMS experiments, Bond et al. [126] concluded that chains of vanadate groups exist on the TiO_2 support. The dimeric vanadates presented in this section are an example of such chains. Went et al. [129] concluded from their Raman spectroscopy studies that polymeric vanadate species have repeating units with divanadyl groups connected by V-O-V bonds. Bulushev et al. [133] proposed a polyvanadate structure with repeating units containing one vanadyl group where vanadium is making one V-O-Ti bond and the vanadyl groups are connected by V-O-V bonds. But such structures are not found in the present work. Their interpretations are questionable as they were based on independent evidence from V-O-V bonds and divanadyl and monovanadyl groups obtained in their experiments.

Condensation between VO_4H_3 groups can take place in ambient conditions which could lead to different condensed species like decavanadate [108]. But such a situation was not considered in the simulations.

5.2.7 Reaction of the Surface Hydroxyl Groups with VO_4H_3

5.2.7.1 Formation of Surface Hydroxyl Groups

Under ambient conditions, the surface of TiO_2 particles is hydrated. The number of hydroxyl groups on the surface of TiO_2 particles is nearly 1-2 per nm^2 [134]. Doe and Wachs [108] have discussed the effect of the surface hydroxylation on the structure of VO_x species found on the TiO_2 surfaces. The surface hydroxyls are found to be reactive towards the adsorbing species. They were believed to control the structure of the metal oxide species [135].

Table 5.18: Calculated adsorption energies E_{ads} (kJ/mol) of a water molecule on various anatase surfaces in molecular and dissociative form

Surface	E_{ads}	
	Molecular	Dissociative
(101)	-99	-160
(001)	-100	-208
(100)	-107	-194

As a first step water adsorption on anatase was investigated. The clusters used for these simulations were the same as discussed in section (5.2.4). Adsorption energies for molecular and dissociative adsorption on the (101), (001) and (100) surfaces are given in Table 5.18. According to MSINDO results, dissociative adsorption of water is thermodynamically more favorable than molecular adsorption on the three anatase surfaces considered. But in previous periodic DFT calculations [136,137] it was found that molecular adsorption of water is thermodynamically more stable than the dissociative adsorption on the anatase (101) and (100) clean surfaces. Periodic Hartree Fock [138] and SINDO1 free-cluster calculations [139] agree with the present MSINDO-CCM calculations that dissociative adsorption of water molecule is favored on the anatase (001)

surface.

In the next section, the results of the investigation of reactions of surface hydroxyls with the adsorbed monomeric VO_4H_3 groups are described.

5.2.7.2 Anatase (101)

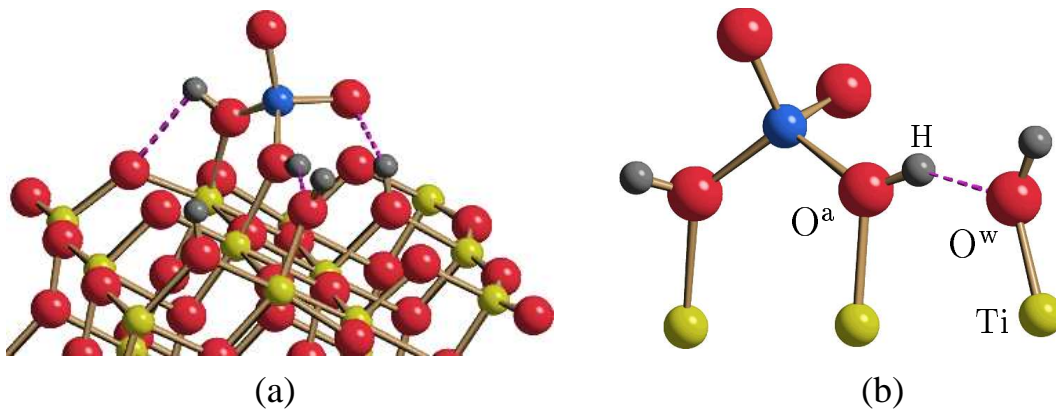


Figure 5.26: (a) VO_4H_3 adsorbed dissociatively near by a dissociated water molecule on (101) surface; (b) the hydroxyl group and the VO_4H_3 group, including the surface titanium atoms involved in the adsorption are shown separately from a different perspective for clarity.

At first dissociatively adsorbed VO_4H_3 on the (101) surface, as shown in Figure 5.18b, was considered. The surface area of the (101) $\text{Ti}_{36}\text{O}_{72}$ cluster is nearly 1.0 nm^2 . In order to match the experimentally observed hydroxyl concentration of 1-2 OH per nm^2 , one water molecule was adsorbed dissociatively on the surface, nearby the VO_4H_2 species (see Figure 5.26). The oxygen atom of the adsorbate with the proton H, near to the hydroxyl group is named O^{a} and oxygen atom of the hydroxyl group is denoted by O^{w} . An MD simulation at 300 K was performed for 2 ps. A metadynamics simulation was performed after this MD simulation to analyze the condensation reaction between the surface hydroxyl group and the protons of the VO_4H_2 species. The distances $r(\text{O}^{\text{a}}-\text{H})$, $r(\text{O}^{\text{w}}-\text{H})$, and $r(\text{O}^{\text{w}}-\text{Ti})$ (see Figure 5.26b) were selected as the collective coordinates. The collective coordinates were scaled according to their fluctuations during the previous MD run. The temperature of the simulation was kept at 300 K using the NHC thermostat. The metadynamics parameters Δs^\perp , M_α , k_α , W (in (3.75) and (3.76)) were chosen as 0.15, 20.0 a.m.u., 1.0 kJ/mol and 2.0 kJ/mol, respectively. A time

step of 1 fs was used for updating the nuclear coordinates and velocities. The Gaussian functions were updated at every 50 steps of the simulation.

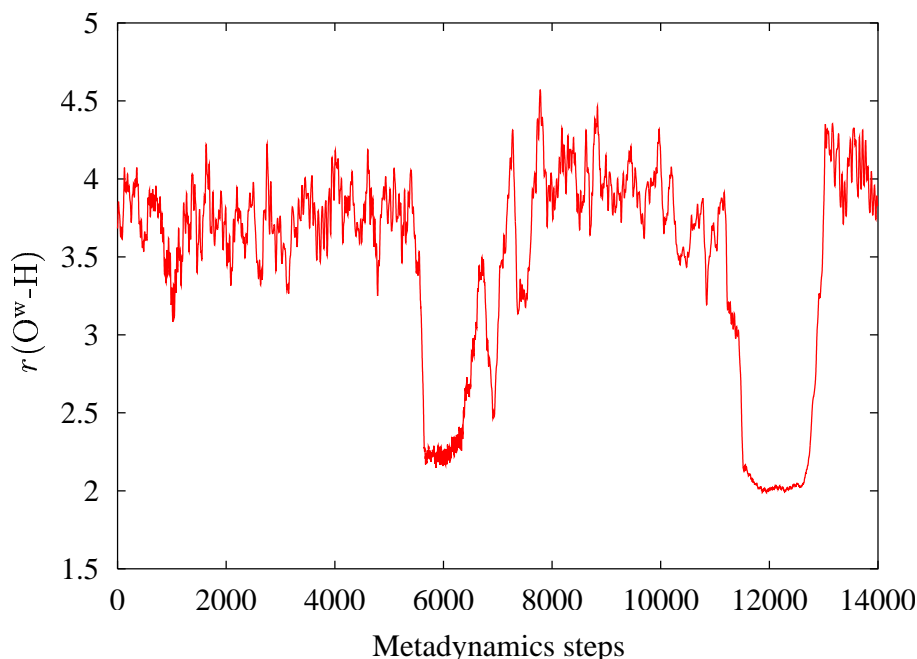


Figure 5.27: The distance $r(\text{O}^w\text{-H})$ between oxygen O^w and hydrogen H during the metadynamics simulation (see Figure 5.26 for labeling)

The distance $r(\text{O}^w\text{-H})$ during this simulation is shown in Figure 5.27. It never decreased below 2 Å indicating that no proton transfer from the VO_4H_2 group to the hydroxyl group occurred within 14000 steps of the simulation. From the snapshots at those points where $r(\text{O}^w\text{-H})$ is smallest, it was observed that the hydroxyl group bent about 30 degrees from the normal to the surface towards the VO_4H_2 group. The distance between the two closest titanium atoms on this surface is quite large (≈ 3.6 Å) and VO_4H_2 group is rigid. Because of these reasons, proton transfer from the hydroxyl groups and the VO_4H_2 did not occur under the present conditions.

By using Gaussians of appropriate width and height ($\Delta s^\perp = 0.30$ and $W = 10$ kJ/mol) in the metadynamic simulation, the condensation reaction could be enforced. However the transition state structure obtained in this way was unrealistic as the proton H was not connected to O^a or O^w (Figure 5.26b). Both MD simulations strongly indicate that transfer of a proton from VO_4H_2 to adsorbed OH groups is unlikely on the anatase (101) surface.

For structures (5.18c) and (5.18d) similar effects were observed. The VO_4H_3 molecule

is less flexible in those two cases compared to structure (5.18b) and thus proton transfer from the adsorbate to the hydroxyl group is unfavorable.

5.2.7.3 Anatase (001)

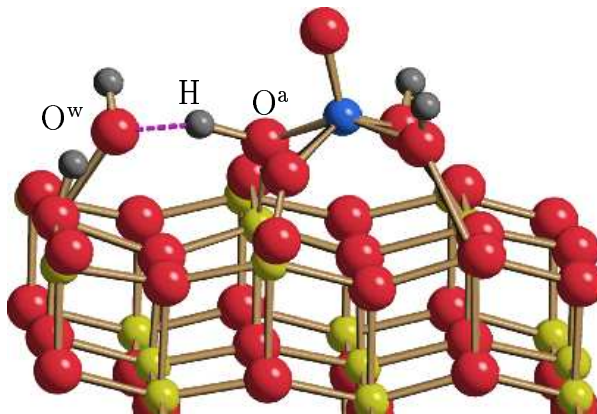


Figure 5.28: A snapshot during the metadynamics simulation of the reaction of the hydroxyl group with the VO_4H_3 molecule adsorbed on the (001) surface.

The surface area of the (001) $\text{Ti}_{36}\text{O}_{72}$ cluster is approximately 1 nm^2 . Thus to simulate experimental hydroxyl concentration on the (001) surface, one water molecule was dissociatively adsorbed near to the hydrated vanadia species (5.20b) in order to form structure (5.28). Starting from the optimized geometry an MD simulation was performed at 300 K for 2 ps using the NHC thermostat. No structural rearrangement was observed during this simulation, in particular, no hydrogen transfer from O^a to O^w . Metadynamics simulation was performed after the MD simulation in order to investigate the possible reaction between the hydroxyl group and the adsorbate. The collective coordinates, and the values of the metadynamics parameters used for the simulation were the same as mentioned in the previous section.

The distance $r(\text{O}^w\text{-H})$ during the metadynamics simulation is shown in Figure 5.29. No condensation reaction was observed within 12000 steps of the simulation. This was expected because the square-pyramidal structural is strongly bound to the surface and therefore not flexible enough to bend towards the hydroxyl group. But compared to the situation on the (101) surface, the hydroxyl group can bend more towards the protons of the adsorbate molecule, because three-fold coordinated oxygen atoms bridging neighboring titanium atoms along the [010] direction are lying below the

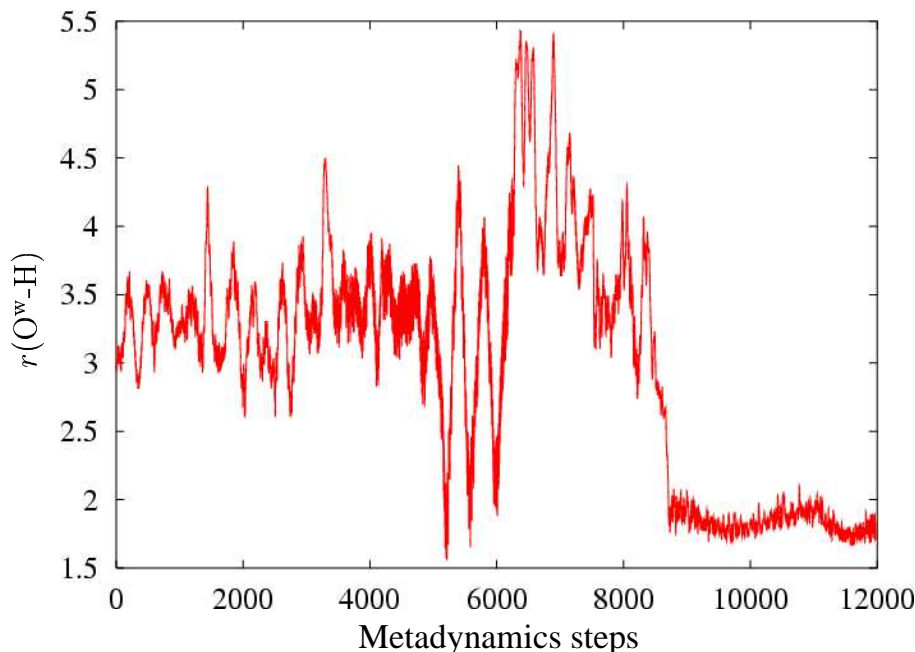


Figure 5.29: Distance $r(\text{O}^w\text{-H})$ between oxygen O^w and hydrogen H (Figure 5.28) during the metadynamics simulation.

plane containing the surface titanium atoms. The lowest $r(\text{O}^w\text{-H})$ distance during the metadynamics simulation is about 1.6 Å which is considerably less than in the simulation of the corresponding (101) surface reaction. The hydroxyl group bent about 35 degrees from the surface normal. The observed increase in distance $r(\text{O}^w\text{-H})$ between 6000 to 7000 steps of the metadynamics simulation was due to the proton transfer from the oxygen labeled O^a to the nearby two-fold coordinated oxygen atom connected to the vanadium atom.

5.2.7.4 Anatase (100)

In the case of the (100) surface, similar simulations were performed as mentioned before. The starting structure for the preliminary MD simulation is given in Figure 5.30a. The distance $r(\text{O}^a\text{-H})$ during the MD simulation and the following metadynamics simulation is shown in Figure 5.31. Within a few steps of the MD simulation the proton labeled H bent towards the hydroxyl group (see Figure 5.30b) by which the distance $r(\text{O}^a\text{-H})$ decreased from 3.4 Å to 2.0 Å. Within 250 steps of the metadynamics simulation, proton transfer occurred from the VO_4H_3 group to the hydroxyl group. The resulting structure is shown in Figure 5.30d. The final structure shown in Figure 5.30d is 51

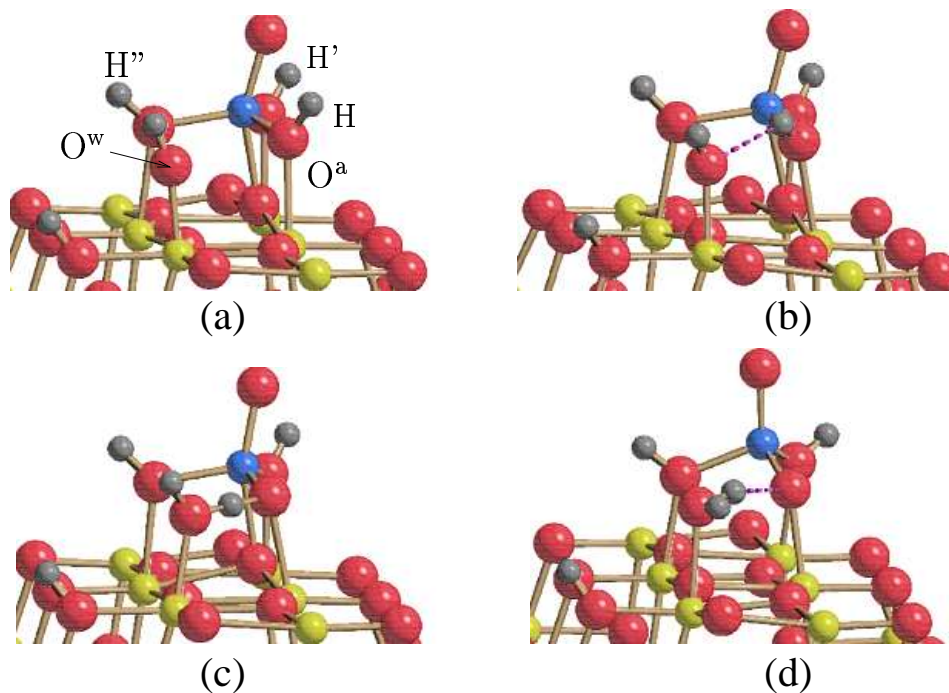


Figure 5.30: Different structures during the metadynamics simulation of the reaction between surface hydroxyls with VO_4H_3 on the anatase (100) surface

kJ/mol lower in energy than structure (5.30a). The transition state structure obtained from the metadynamics simulation is shown in Figure 5.30c. The potential energy barrier for this reaction is about 40 kJ/mol. After the proton transfer, vanadium to surface oxygen bond was broken as the bond from vanadium to oxygen labeled O^a became stronger.

Protons labeled H and H' behave in a similar way (see Figure 5.30a) while the proton labeled H'' is different. The reaction between the hydroxyl group with the proton H'' is unlikely because the distance $r(\text{O}^w\text{-H}'')$ ($> 3.6 \text{ \AA}$) is unfavorable for such a reaction.

5.2.7.5 Discussion

A reaction between a preadsorbed hydroxyl group and the adsorbed VO_4H_3 molecule is only favorable on the (100) surface and not on the anatase (001) and (101) surfaces. Protons of type H and H' (Figure 5.30a) can react with surface hydroxyl groups adsorbed on the nearest five-fold coordinated titanium atoms. This will result in the formation of a VO_4H group on the surface. Similar reactions are possible for $\text{V}_2\text{O}_7\text{H}_4$. Thus one can conclude that the hydrated polymeric chains formed on the (100) surface

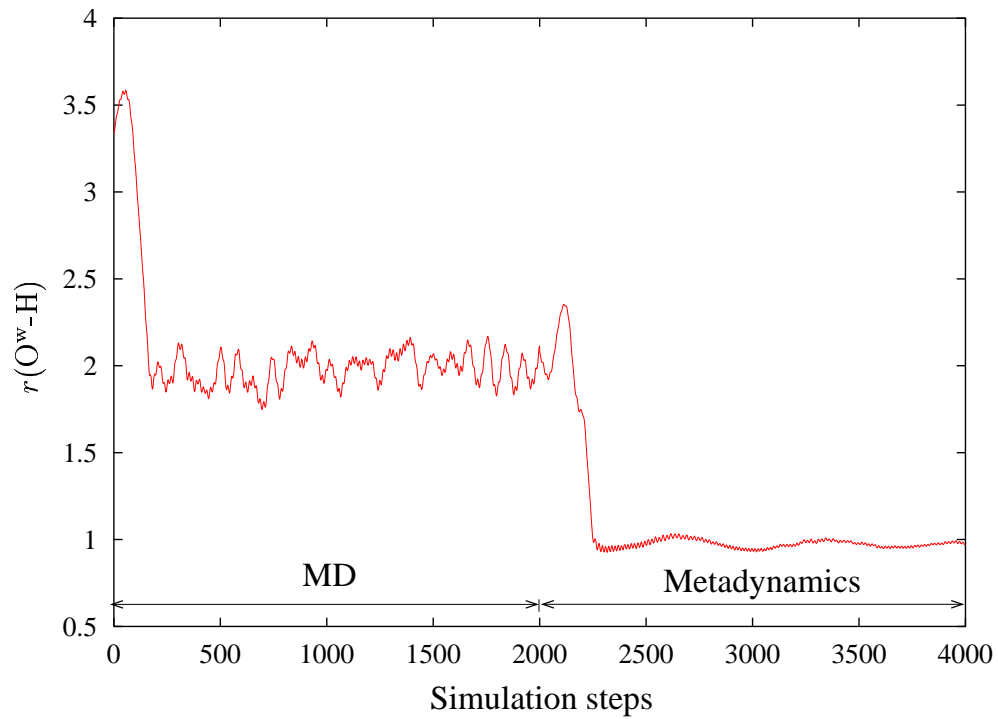


Figure 5.31: Distance $r(\text{O}^a\text{-H})$ between oxygen O^a and hydrogen H during the MD and the metadynamics simulations (see Figure 5.30 for labeling)

will have the form $(\text{VO}_4\text{H})_n$. At present there are no experimental predictions for this structure.

5.3 Oxygen Vacancy Diffusion in Rutile

5.3.1 Introduction

Titanium dioxide is the most investigated crystalline metal oxide [115]. In surface science, titanium dioxide is considered as a model system for many metal oxides. Understanding its properties at fundamental level will help to improve materials and device performance in many fields. TiO_2 is a wide gap semiconductor with many interesting applications. It is used in heterogeneous catalysis, as photocatalyst in solar cells for the production of hydrogen and electric energy, as a gas sensor, as white pigment, in corrosion-protective coating and in electronic and electrical devices [115]. It is used in bone implants due to its biocompatibility [140].

Titanium dioxide crystallizes in three different modifications: rutile, anatase and brookite. As discussed in the previous section, rutile is the thermodynamically most stable form of TiO_2 . Stable surfaces of rutile are the (110), (100) and (001) surfaces [141].

The phase diagram of TiO_2 contains various stable phases with different crystal structures [115]. TiO_2 can be easily reduced. Bulk reduction leads to a pronounced color change of the crystal (from transparent to light and dark blue). Intrinsic defects result in high conductivity. Defects play an important role in making TiO_2 technologically important. The bulk structure of reduced TiO_2 is quite complex with various types of defects such as oxygen vacancies, Ti^{3+} as well as Ti^{4+} interstitials and two-dimensional defects such as crystallographic shear planes. The defect structure varies with amount of oxygen deficiency which depends on temperature, gas pressure, impurities etc.. The dominant type of defect is still a subject of discussion.

The ability to control the amount of point defects on the surface is a peculiar feature of TiO_2 . The oxygen-deficient surface stoichiometry and structure of ion sputtered TiO_2 can be restored to bulk-like quality by annealing in vacuum in the absence of gas phase oxidant [142–144]. The stoichiometry of the surface can be restored either by the diffusion of the Ti^{3+} ions from the surface to the bulk or by the diffusion of oxygen anions from bulk to the surface. The actual point defect diffusion mechanism, which is responsible for bulk-assisted reoxidation is still unknown. Many research groups believe that oxygen atoms diffusing from the bulk to the surface is the mechanism [145–147]. In contrast, Henderson [148] reported that Ti^{3+} interstitials are responsible for this

phenomenon.

The effect of point defect diffusion is also observed in adsorption studies on rutile surfaces. It is assumed that the formation of TiS_x layer on rutile surface during the adsorption of sulfur on clean rutile (110) surface at high temperature is due to the migration of oxygen vacancies from bulk to the surface [149]. Dissociative adsorption of water molecules at temperatures near 500 K may also be due to the increase in concentration of the surface oxygen vacancies, which act as the active centers for the water dissociation [150]. Effect of oxygen vacancy diffusion was also observed in the case of NO_2 adsorption on the rutile (110) surface at high temperatures [151].

To my knowledge, no theoretical studies have been performed so far on the oxygen vacancy diffusion in rutile. Activation energies for the diffusion of small cations were calculated by Ajayi et al. [152] using classical potentials. With calculations based on classical interatomic potentials, Catlow and James [153] predicted that oxygen vacancies are the most stable non-stoichiometric defects. Shen and Bursill [154] found that a reconstructed titanium interstitial defect structure is more stable than other types of defects. Most of the quantum chemical studies conducted in this field concentrated only on the electronic structure of the oxygen vacancy in the bulk and on the surfaces of rutile [155–160]. Yu and Halley [161] investigated the electronic structure of the Ti^{4+} interstitials. But their semiempirical calculations did not take into account relaxation of atoms surrounding the defect. Rodriguez et al. [162] performed DFT calculations to obtain the relative stabilities of oxygen vacancies on the surface and in sub-surface layers, and of interstitial Ti^{4+} in the bulk and on the surface, in the presence of an adsorbed sulfur atom.

Quantum chemical MD simulations on the diffusion process of oxygen vacancies are of great importance in understanding the structure and reactivity of rutile at high temperatures. In this section, diffusion of oxygen vacancies are studied using MD techniques. First the bulk properties of rutile are calculated with MSINDO as basis for the defect studies.

5.3.2 Bulk Properties of Rutile

Rutile has a tetragonal unit cell ($a = b \neq c$) which is shown in Figure 5.32. The space group of rutile is $D_{4h}^{14}\text{-P4}_2/\text{mnm}$. As discussed in the case of anatase (Section 5.2.2),

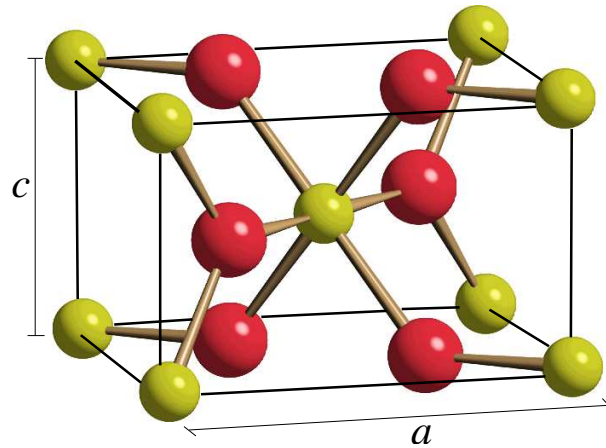


Figure 5.32: Unit cell of rutile

one additional parameter u is necessary to define the unit cell, which is the oxygen fractional coordinate. Experimentally determined values of unit cell parameters are $a = 4.587 \text{ \AA}$, $c = 2.954 \text{ \AA}$ and $u = 0.305$ [163]. The binding energy per TiO_2 unit for rutile was estimated to be 1894 kJ/mol experimentally [118].

To obtain the bulk properties of rutile with MSINDO, CCM three-dimensional calculations were performed. The three-dimensional cyclic $\text{Ti}_{48}\text{O}_{96}$ cluster was chosen for this calculation and the cell parameters were optimized. This cluster was found to give converged bulk properties in a previous MSINDO-CCM calculation [23]. Calculated bulk properties of rutile are given in Table 5.19. The obtained unit cell parameters are $a = 4.434 \text{ \AA}$, $c = 2.925 \text{ \AA}$, and $u = 0.300$. The cell parameters a , c , and u deviate by about -3% , -1% , and -2% from the experimental values, respectively. Compared to the values reported by Lazzeri et al. [98] using periodic DFT/LDA calculations, a , c , and u deviate about -2% , 0% , and -1% , respectively. Thus the lattice parameters are in good agreement with the previous calculation and the experiment (see Table 5.19). The binding energy per TiO_2 unit obtained by the present calculation (2082 kJ/mol) is in reasonable agreement with the experimental result (1894 kJ/mol) [118].

Thus MSINDO can reproduce the bulk properties of rutile reasonably well. Before conducting the defect studies, the surface properties of rutile were also studied using the MSINDO-CCM.

Table 5.19: Bulk properties of rutile

Properties		MSINDO	DFT	Experiment
Unit cell parameters	a (Å)	4.434	4.546 ^a	4.587 ^b
	c (Å)	2.925	2.925 ^a	2.954 ^b
	u	0.300	0.303 ^a	0.305 ^b
Binding energy per TiO ₂ (kJ/mol)		2082	2360 ^a	1894 ^c

^a Ref. [98]

^b Ref. [163]

^c Ref. [118]

5.3.3 Surface Properties of Rutile

Various surfaces of rutile have been studied using different levels of theory and experiments [115]. On the rutile (110)-(1×1) surface (see Figure 5.33a), there are two kinds of titanium and oxygen atoms. Five-fold coordinated and six-fold coordinated titanium atoms form alternate rows along the [001] direction. Rows of two-fold coordinated oxygen atoms are also present on this surface in the [001] direction. Three-fold coordinated oxygen atoms are lying in the main surface plane of the (110) surface. Even though the (110) surface is very stable, it undergoes reconstruction at high temperatures. The rutile (100) surface (see Figure 5.33b) is highly corrugated with periodic arrays of ridges and troughs parallel to the [001] direction. Similar to the (110) surface, rows of two-fold coordinated oxygen atoms form the first atomic layer of this surface. The surface also exposes five- and six-fold coordinated titanium atoms and three-fold coordinated oxygen atoms. The (100)-(1×1) surface undergoes reconstruction at relatively low temperatures compared to the (110) surface. A common kind of reconstruction found on this surface is (1×3). Different from the (110) and (100) surfaces, the (001) surface exposes four-fold coordinated titanium atoms (see Figure 5.33c). The surface also contains six-fold coordinated titanium atoms and two-fold coordinated oxygen atoms. The (001) surface undergoes reconstructions very easily. Different reconstruction patterns are observed on this surface at relatively low temperatures [115].

Surface energies of the rutile (110), (100) and (001) surfaces and their convergence with respect to the number of relaxed layers were studied using MSINDO. The two-dimensional cyclic clusters used for the simulations of the (110), (100) and (001) sur-

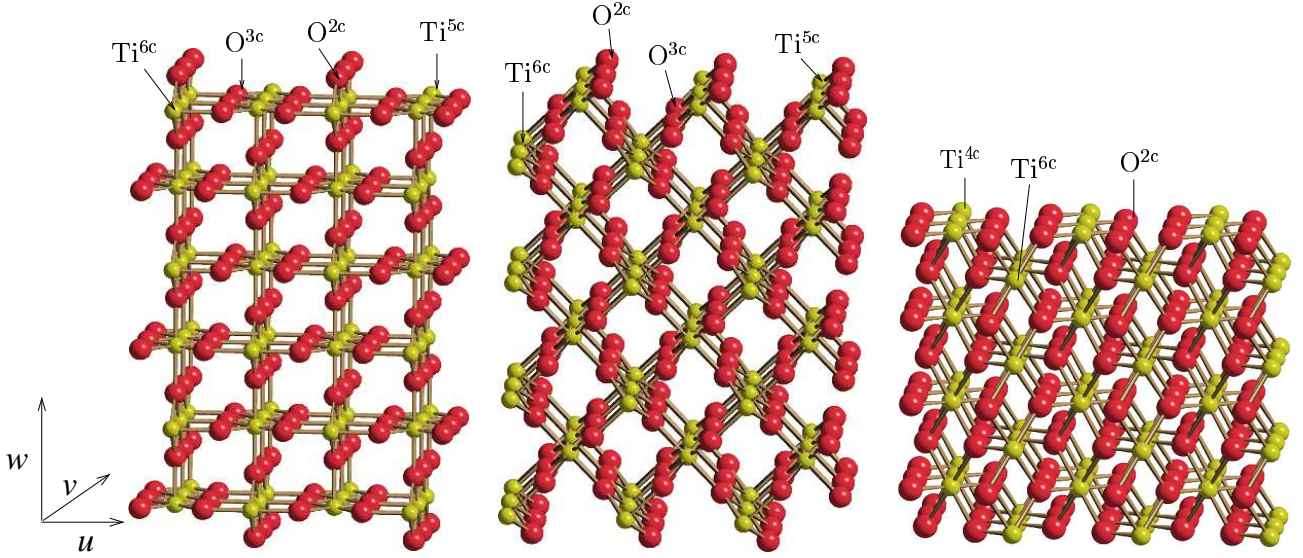


Figure 5.33: Clusters used for modeling various surfaces of rutile; (a) rutile (110) $2 \times 3 \times 4$ ($\text{Ti}_{96}\text{O}_{192}$) cluster. $u = [1\bar{1}0]$, $v = [001]$, $w = [110]$. (b) rutile (100) $3 \times 3 \times 4$ ($\text{Ti}_{54}\text{O}_{108}$) cluster. $u = [010]$, $v = [00\bar{1}]$, $w = [100]$. (c) rutile (001) $3 \times 3 \times 4$ ($\text{Ti}_{72}\text{O}_{144}$) cluster. $u = [100]$, $v = [0\bar{1}0]$, $w = [001]$.

faces were $\text{Ti}_{120}\text{O}_{240}$, $\text{Ti}_{90}\text{O}_{180}$, and $\text{Ti}_{90}\text{O}_{180}$. Surface energies were calculated according to (5.82). The reference bulk energy E_{bulk} in (5.82) was estimated obtained from a three-dimensional CCM calculation of $\text{Ti}_{48}\text{O}_{96}$ cluster. They are almost converged after relaxing 9, 9 and 4 atomic layers of (110)- $\text{Ti}_{120}\text{O}_{240}$, (100)- $\text{Ti}_{90}\text{O}_{180}$ and (001)- $\text{Ti}_{90}\text{O}_{180}$ clusters, respectively (Table 5.20). The calculated surface energies were higher than the periodic DFT/LDA results [141]. As discussed in the previous section, DFT might be underestimating the surface energies. From the calculated surface energies, the relative stability of rutile surfaces in increasing order is (001) < (100) < (110). The same order of stability was also reported by Ramamoorthy et al. [141].

The surface relaxation of the rutile (110), (100), and (001) surfaces was also studied using MSINDO-CCM. The changes of atomic positions with respect to the corresponding bulk structure are given in Table 5.21. For the calculation of the surface relaxation, (110)- $\text{Ti}_{120}\text{O}_{240}$, (100)- $\text{Ti}_{90}\text{O}_{180}$ and (001)- $\text{Ti}_{90}\text{O}_{180}$ clusters were used and 6, 6 and 2 atomic layers were relaxed on either side of the clusters, respectively. The surface relaxation calculated for the rutile (110) cluster in reasonable agreement with previous DFT/LDA calculations [141, 164] and with surface x-ray diffraction exper-

Table 5.20: Comparison of calculated surface energies E_{surf} (J/m²) of the rutile (110), (100), and (001) surfaces obtained with MSINDO and periodic LDA DFT calculations [141]. N_{rlx} is the number of atomic layers relaxed in both sides of the cluster.

Surface	MSINDO		DFT/LDA ^a	
	Cluster	N_{rlx}	E_{surf}	
(110)	Ti ₁₂₀ O ₂₄₀	6	1.75	0.89
		7	1.74	
		8	1.71	
		9	1.71	
(100)	Ti ₉₀ O ₁₈₀	6	2.33	1.12
		7	2.30	
		8	2.29	
(001)	Ti ₉₀ O ₁₈₀	2	2.67	1.40
		3	2.65	
		4	2.64	

iments [165]. For the rutile (100) surface, no displacement of the five-coordinated titanium atom was observed along the [100] direction, unlike the results of other theoretical studies [141, 166], where a small downward displacement was observed. Even though the magnitude of the O^{2c} displacements along the [010] and [100] directions on the (100) surface are quite large ($\Delta u = -0.35, \Delta w = 0.08$) compared to those reported by Ramamoorthy et al. [141] ($\Delta u = -0.18, \Delta w = 0.00$), they are in good agreement with more recent periodic DFT/LDA calculations by Muscat et al. [166] ($\Delta u = -0.31, \Delta w = 0.06$). In the case of the (001) surface, a qualitative difference in the results of MSINDO calculation and DFT/LDA calculation by Ramamoorthy et al. [141] exists for the relaxation of the O^{2c} atoms in the [001] direction. But the results of the present calculations are in good agreement with the periodic HF calculations by Muscat and Harrison [167].

Table 5.21: Surface relaxation of rutile surfaces; Δu , Δv , and Δw (Å) of atomic coordinates with respect to the corresponding bulk positions. MSINDO results are compared with periodic DFT/LDA results from Ramamoorthy et al. [141]

Surface	Cluster	Atom	Relaxations					
			MSINDO			DFT/LDA ^a		
			Δu	Δv	Δw	Δu	Δv	Δw
(110)	Ti ₁₂₀ O ₂₄₀ 2 × 3 × 5	Ti ^{5c}	0.00	0.00	-0.08	0.00	0.00	-0.18
		Ti ^{6c}	0.00	0.00	0.16	0.00	0.00	0.13
		O ^{2c}	0.00	0.00	-0.04	0.00	0.00	-0.07
		O ^{3c}	-0.06	0.00	0.14	0.00	0.00	0.12
(100)	Ti ₉₀ O ₁₈₀ 3 × 3 × 5	Ti ^{5c}	0.06	0.00	0.00	0.17	0.00	-0.07
		Ti ^{6c}	0.02	0.00	0.00	0.10	0.00	0.00
		O ^{2c}	-0.35	0.00	0.08	-0.18	0.00	0.00
		O ^{3c}	-0.11	0.00	0.03	-0.12	0.00	0.02
(001)	Ti ₉₀ O ₁₈₀ 3 × 3 × 5	Ti ^{4c}	0.00	0.00	-0.13	0.00	0.00	-0.32
		Ti ^{6c}	0.00	0.00	0.15	0.00	0.00	0.32
		O ^{2c}	0.07	-0.07	-0.05	0.10	-0.10	0.03

^a Ref. [141]

5.3.4 Diffusion of Surface Oxygen Vacancy

The most prominent point defect present on the rutile surfaces and in the bulk is the oxygen vacancy. Surface oxygen vacancies have been experimentally characterized with spectroscopic techniques [93]. The concentration of such surface defects varies according to the preparative methods and thermal treatments [115]. Oxygen vacancies are observed as bright spots in STM images of the rutile (110) surface [168].

For studying the oxygen vacancy diffusion, a two-dimensional Ti₄₈O₉₅-(2×3×2) cluster was used. An oxygen defect at the surface was first considered. The defect is in the position of a bridging two-fold coordinated oxygen atom of the Ti₄₈O₉₆-(2×3×2) cluster (as shown in Figure 5.34b). For a better explanation, relevant atoms of the cluster are labeled as shown in Figure 5.35. The same labeling is used throughout this section. One oxygen vacancy was created in the position 7 (Figure 5.35) and is denoted by X(7). Closed shell singlet and open shell triplet calculations were performed on this

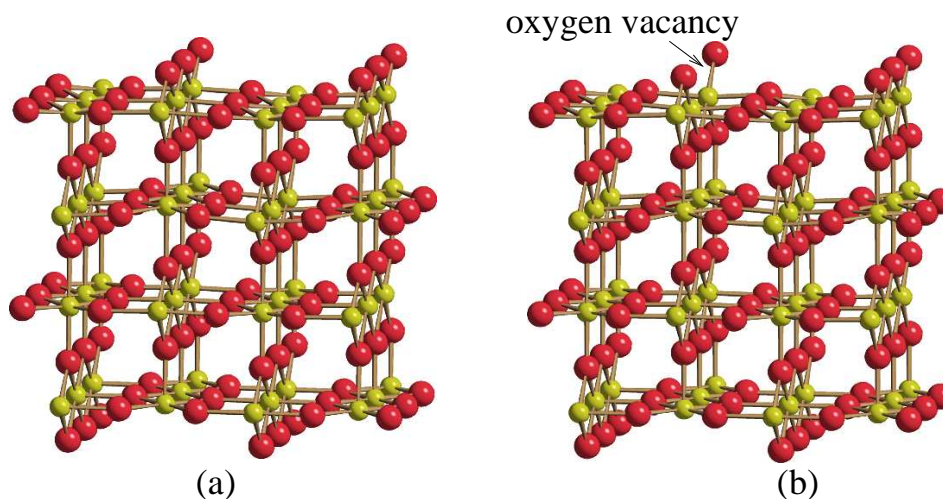


Figure 5.34: (a) (110)-Ti₄₈O₉₆ cluster; (b) (110)-Ti₄₈O₉₅ cluster with an oxygen vacancy

system. The triplet spin state was treated by the UHF method. It was found that the triplet state is 441 kJ/mol lower in energy than the singlet state. Many of the previous calculations have also demonstrated that the spin-polarized state is more stable than the spin-paired situation [157, 158, 160].

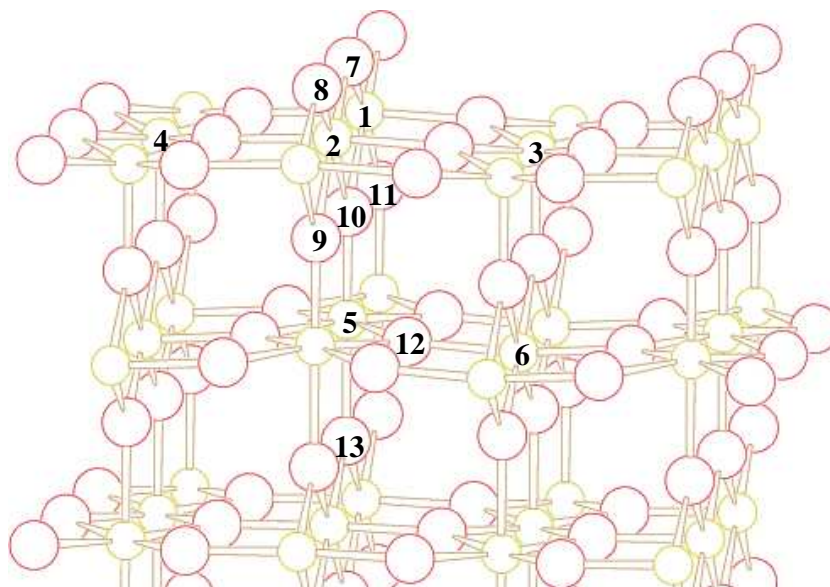


Figure 5.35: Labeling of the ideal lattice positions of titanium (yellow circles) and oxygen atoms (red circles) in the rutile (110)-Ti₄₈O₉₅ cluster used for the simulations

The spin densities of the titanium atoms neighboring the defect (see Figure 5.35) are shown in Table 5.22. The spin density on the titanium atoms Ti(1) and Ti(2), which became five-fold coordinated after the loss of oxygen, is very close to zero, 0.005 a.u.. The unpaired electrons are mainly located at the surface titanium atoms Ti(3) and Ti(4) with spin densities close to 1.0 a.u.. The spin density of the six-fold coordinated titanium atom Ti(5) is 0.0.

Table 5.22: Spin densities (in a.u.) of titanium atoms neighboring the defect X(7); see Figure 5.35 for labeling

Atom	Spin density
Ti(1)	0.005
Ti(2)	0.005
Ti(3)	0.988
Ti(4)	0.988
Ti(5)	0.000

Previous calculations have also found that the unpaired electrons are localized on these titanium atoms. Mackrodt et al. [157] and Chen et al. [159] introduced artificial basis functions on the defect site in their calculations in order to check the possibility of an F-type color center and came to the same conclusion that the electrons are localized on the five-fold coordinated titanium atoms rather than on the defect site. The same conclusion was also obtained in the experiments [115, 169].

The MD techniques as implemented in MSINDO were used to simulate the oxygen diffusion process. At first the diffusion of the oxygen atom O(10) to vacancy X(7) was considered. As mentioned earlier, the UHF approach was used for the calculations of the triplet state. The annealing temperature used in the experiments is usually between 700 K and 1200 K. Due of this reason, temperature of the simulation was selected as 1000 K. An MD simulation was performed for 10 ps using the Nosé-Hoover chain thermostat and a time step of 1 fs. At every step of the simulation the density matrix elements were converged to 1×10^{-7} a.u. in the SCF calculations. Three atomic layers in the bottom of the cluster were fixed during the MD simulation. The thermostat frequency was assigned as 750 cm^{-1} , which is close to the maximum surface phonon

frequency of rutile. Large amplitude vibrations were observed for the surface atoms during the simulation. But no oxygen vacancy diffusion occurred within 10 ps time scale.

To accelerate the diffusion process, the metadynamics technique was employed. Three collective coordinates were selected for the metadynamics simulation. One of the collective coordinates was the distance between the oxygen atom O(10) and the titanium atom Ti(5). When diffusion takes place, the distance O(10)-Ti(5) will increase. The distance between the vacancy X(7) and the diffusing oxygen O(10) was the second collective coordinate. This distance should decrease to zero during the diffusion. The third collective coordinate was the angle θ defined by \angle O(9)-O(10)-O(11). This angle will decrease from 180 degrees during the diffusion process.

The collective coordinates were scaled according to their fluctuations during the previous MD simulation at 1000 K as mentioned in Section 3.2.2. The metadynamics parameters Δs^\perp , W , k_α and M_α (in (3.75) and (3.76)) were 0.3, 5.0 kJ/mol , 1.0 kJ/mol and 20 a.m.u., respectively. The time step of the simulation was 1 fs and the Gaussian potential was updated at every 50 steps. Temperature was kept constant at 1000 K using the Nosé-Hoover chain thermostat, similar to the MD simulation.

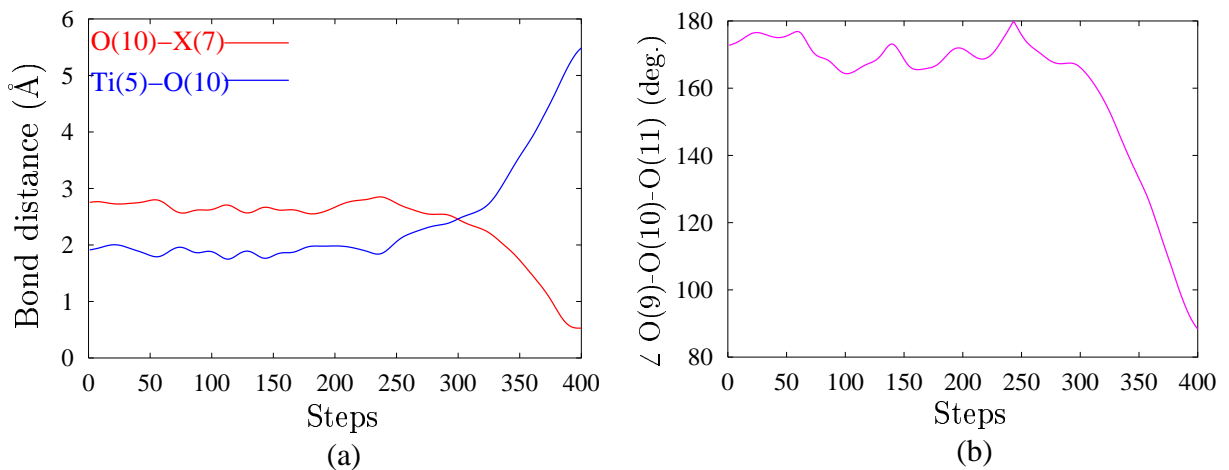


Figure 5.36: (a) Distances O(10)-X(7) and Ti(5)-O(10); (b) Angle O(9)-O(10)-O(11) during the metadynamics simulation of O(10)-X(7) migration. Labeling of the atoms are according to Figure 5.35.

The values of the unscaled collective coordinates during the simulation are shown in Figure 5.36. In 400 steps of the simulation, oxygen O(10) had moved to the X(7)

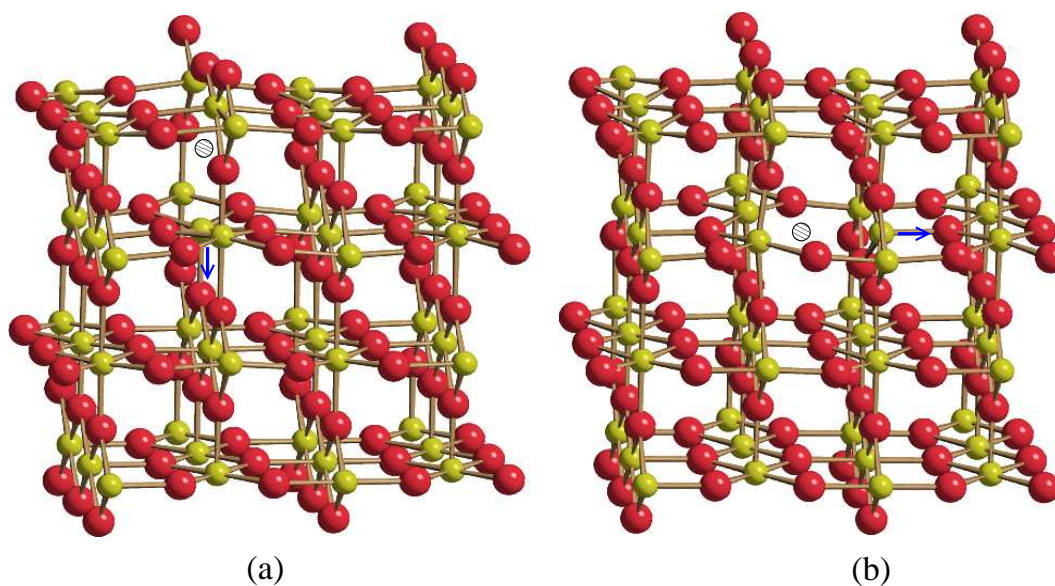


Figure 5.37: Energy minimum structures of $\text{Ti}_{48}\text{O}_{95}$ cluster with oxygen vacancies (shaded circles); (a) vacancy X(10) (b) vacancy X(12). Labeling of the atoms are according to Figure 5.35. Blue arrows from titanium atoms show its direction of relaxation due to the formation of the vacancy

position, and the structure shown in Figure 5.37a was obtained. A transition state search was performed from the approximate transition state structure obtained from the metadynamics simulation. The calculated barrier height was 131 kJ/mol. The final structure after the diffusion process (Figure 5.37a) is 75 kJ/mol higher in energy than the initial structure (5.34b).

In the final structure (5.37a), the titanium atom Ti(5) (Figure 5.35) is five-fold coordinated and has relaxed downwards by about 0.38 Å. The unpaired electrons remained at the surface atoms Ti(3) and Ti(4) with spin densities close to 1.0 a.u. (see Table 5.23).

To confirm the stability of structure (5.37a), an MD simulation for 10 ps at 1000 K was performed for that structure. Technical details of the MD simulation were the same as discussed before. No oxygen vacancy diffusion was observed during this simulation.

When the final structure (5.37a) was treated as a closed shell system, its energy was found to be 246 kJ/mol higher than the triplet state. On the singlet hypersurface, structure (5.37a) is 35 kJ/mol lower in energy than structure (5.34b). A wrong description of the relative energies is thus obtained from closed shell calculations. This

Table 5.23: Calculated spin densities on atoms neighboring the oxygen defect for structures (Figure 5.37a) and (Figure 5.37b). See Figure 5.35 for labeling

Structure	Atom	Spin density
Figure 5.37a	Ti(1)	0.004
	Ti(2)	0.004
	Ti(3)	0.996
	Ti(4)	0.996
	Ti(5)	0.000
Figure 5.37b	Ti(1)	0.003
	Ti(2)	0.003
	Ti(3)	1.000
	Ti(4)	0.997
	Ti(5)	0.000

shows the importance of treating oxygen vacancies in rutile as open shell systems. To investigate the diffusion of the oxygen vacancy further towards the bulk, diffusion of the oxygen atom O(12) to the vacancy X(10) was considered. Three collective coordinates were selected for the description of this diffusion process. Distances Ti(6)-O(12), X(10)-O(12), and \angle X(10)-Ti(5)-O(12) were the collective coordinates. The distance Ti(6)-O(12) should increase and the bond distance X(10)-O(12) should decrease during the diffusion. The bond angle \angle X(10)-Ti(5)-O(12) was reduced from 90 degrees to zero by the movement of O(12). All the technical details for the metadynamics simulation were the same as before. The values of the unscaled collective coordinates during the simulation are shown in Figure 5.38. O(12) left its original position after 1400 steps. The final structure after the migration is shown in Figure 5.37b. A transition state search was performed from the approximate transition state structure obtained in the metadynamics simulations. The potential energy barrier for this diffusion process is about 181 kJ/mol. The final structure (5.37b) is about 128 kJ/mol higher in energy than the initial structure (5.37a). In this structure, the titanium atom Ti(6) has moved away from the defect by about 0.24 Å in the direction shown by the arrows in Figure 5.37b. The spin densities of the titanium atoms Ti(3) and Ti(4) remain close to 1.0

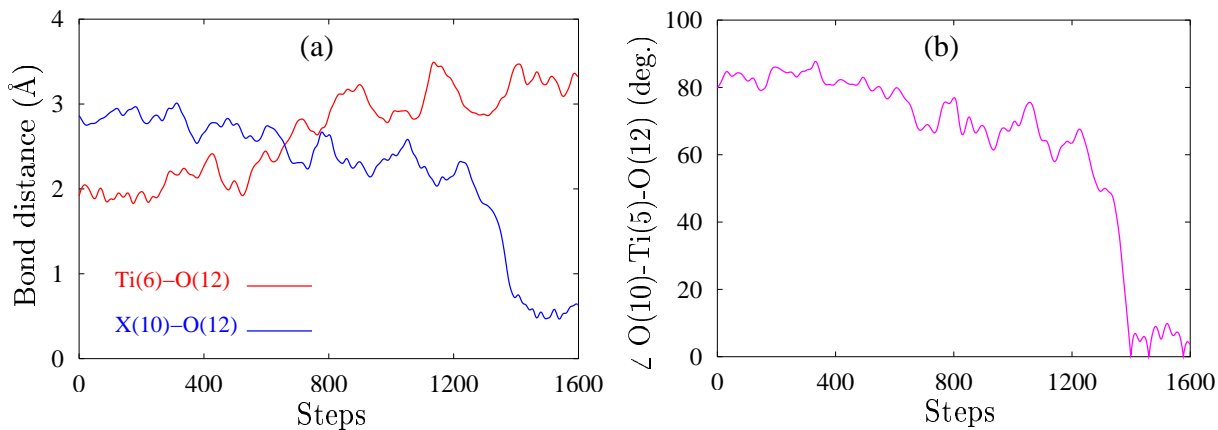


Figure 5.38: (a) Distances Ti(6)-O(12) and X(10)-O(12); (b) Angle X(10)-Ti(5)-O(12) during the metadynamics simulation of O(12)-X(10) migration are shown. Labeling of the atoms are according to Figure 5.35.

(Table 5.23).

The results of the above simulations are summarized in Figure 5.39. Oxygen vacancy diffusion from first atomic layer (structure A in Figure 5.39) to the third atomic layer (structure B in Figure 5.39) has to surmount an activation barrier of 131 kJ/mol. During the diffusion of oxygen vacancy from the third layer to the fifth layer (structure B in Figure 5.39) a barrier of 181 kJ/mol has to be overcome. But the activation barriers for the oxygen vacancy diffusion from the bulk to surface are lower than from the surface to the bulk. The energy barriers for the diffusion processes C to B and B to A are 53 kJ/mol and 56 kJ/mol, respectively.

In order to investigate the feasibility of such diffusion processes in experimental conditions, the time scales of those processes are calculated for various temperatures by applying the transition state theory. For an unimolecular reaction, the reaction rate constant k is given by

$$k = \frac{k_B T}{h} \exp(-\Delta E^\# / k_B T)$$

where k_B is the Boltzmann constant, T is the temperature, h is Plank's constant and $\Delta E^\#$ is the activation energy barrier. The half-life of the reaction $\tau_{1/2}$ is given by,

$$\tau_{1/2} = \frac{\ln 2}{k} \quad (5.83)$$

The half-life of the reaction for the diffusion processes at various temperatures are given in Table 5.24. Structural transition from A to B can occur at temperatures higher than

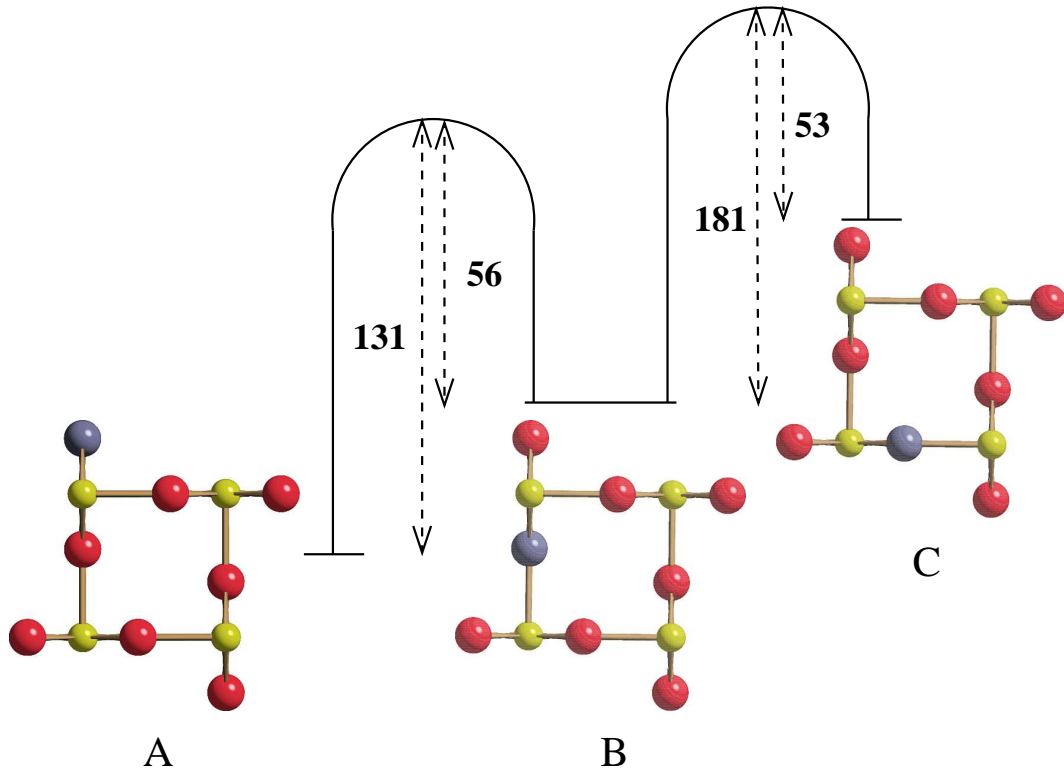


Figure 5.39: Potential energy barriers for oxygen vacancy diffusion processes. Grey spheres represent oxygen vacancy. Structures A, B and C contain oxygen vacancies in the first, third and fourth atomic layers, respectively. Activation energies are given in kJ/mol.

500 K in a time scale of a few seconds. Transition from B to C will occur in a time scale of a few seconds at 700 K. Thus a structural transition from A to B and then to C is probable above 700 K. But the potential energy barriers for the oxygen vacancy diffusion from bulk to surface, that is C to B and B to A, are smaller than those for the surface to the bulk diffusion, that is from A to B and B to C. Thus one can conclude that the route of oxygen vacancy diffusion, A to B and B to C, is unfavorable. On the other hand, bulk to surface oxygen vacancy diffusion, C to B and B to A, is highly favorable at temperatures above 300 K.

During the experimental study of adsorption of sulfur on rutile (110) clean and stoichiometric surfaces, Hebenstreit et al. [149] found that at temperatures above 600 K sulfur atoms occupy the positions of two-fold coordinated bridging oxygen. The above observation can be explained by the migration of the oxygen vacancies from bulk to the surface. At high temperatures S atoms will desorb from the five-fold coordinated tita-

Table 5.24: Half-life for the diffusion processes at different temperatures estimated using transition state theory. see Figure 5.39 for labeling

Temperature (K)	Half time (s)			
	A \rightarrow B	B \rightarrow C	C \rightarrow B	B \rightarrow A
300	10^9	10^{18}	10^{-4}	10^{-4}
500	1	10^5	10^{-8}	10^{-8}
700	10^{-4}	1	10^{-10}	10^{-10}
1000	10^{-7}	10^{-4}	10^{-11}	10^{-11}

niium atoms and will occupy the oxygen vacancies formed on the surface. Increase of the concentration of dissociated water molecules during the water adsorption studies [150] and the observation of increasing surface nitrate content with increasing temperature during the NO_2 adsorption [151] on the rutile (110) surface can be explained by the increase of oxygen vacancy concentration at high temperatures due to its migration from bulk to the surface. The present results are also in line with the observation of Henderson [148] that the oxygen vacancy diffusion from the surface to the bulk is not the mechanism of “bulk-assisted” re-oxidation of the sputtered (110) surface.

Oxygen vacancy diffusion further towards the bulk, X(12) to O(13), was not studied as the cluster used for the present calculations is not large enough to describe relaxation correctly around the defect.

5.4 Water Adsorption on Rutile Surfaces

5.4.1 Introduction

The TiO₂-water system is of fundamental and practical interest in the field of catalysis, electrochemistry, fuel cells, active coatings, corrosion and photochemical applications such as solar cells [93]. Under ambient conditions, water adsorption on rutile surface can affect adsorption and reaction processes. Thus a large number of theoretical and experimental works have been devoted in understanding the water chemistry on the TiO₂ surfaces [170, 171].

Earlier experimental studies of water adsorption on microcrystalline rutile powders concluded that water molecules dissociate on the rutile surfaces [172, 173]. From the infrared spectrum of water molecules on the rutile surface, it was interpreted that water molecules exist in dissociated and undissociated form on the rutile surfaces [174]. Using ultraviolet photo emission spectroscopy experiments Kurtz et al. [175] reported that water molecules adsorb molecularly on the perfect rutile (110) surface at about 160 K in monolayer (ML) coverage. On increasing temperature, concentration of dissociated water molecules was found to increase. The authors believed that increasing concentration of surface oxygen vacancies with temperature is the reason for this observation. Hugenschmidt et al. [150] studied water adsorption on the rutile (110) surface with different defect densities using temperature programmed desorption (TPD), work function measurements and X-ray photoelectron spectroscopy (XPS). They reported that water molecules in monolayer coverage are molecularly adsorbed on the clean surface and desorb at about 270 K. Second-layer water molecules were found to desorb at about 170 K. The TPD peaks at 500 K were assigned to dissociated water molecules at thermally induced oxygen vacancies. Henderson [176] performed high resolution electron energy loss spectroscopy (HREELS) and TPD studies of water adsorption on the rutile (110) surface under ultra high vacuum conditions. From the vibrational features at 1605 cm⁻¹ and 3420 cm⁻¹ for very low water exposures, he concluded that water molecules adsorb molecularly on the rutile (110) surface. Recent investigations with scanning tunneling microscopy (STM) [177, 178] confirmed that oxygen vacancies act as active sites for water dissociation on the rutile (110) surface.

With secondary ion mass spectrometry (SIMS), Bourgeois et al. [179] found that water

adsorbs dissociatively on the rutile (100) surface. The TPD and the oxygen isotopic labeling studies by Henderson [180] showed that the rutile (100) surface is more active for water dissociation compared to the (110) surface. He found that the dissociated water molecules on this surface desorb by a recombination of the surface hydroxyl groups at about 300 K.

Using tight binding embedded cluster calculations, Goniakowski et al. [181] found that dissociative adsorption of water molecule is thermodynamically more stable than molecular adsorption on the rutile (110) surface. Based on periodic HF calculations Fahmi and Minot [138] reported that a water molecule prefers to dissociate on both the rutile (110) and (100) surfaces. The semiempirical SINDO1 cluster calculations of Breidow and Jug [139] also yielded that dissociative adsorption is energetically favored. They reported that water dissociation is more favorable at bridging oxygen vacancies. The same conclusion was obtained from periodic DFT calculations [182, 183]. In contrast, molecular adsorption of a water molecule was found to be lower in energy in the HF and B3LYP embedded cluster calculations of Stefanovich and Truong [185]. Car-Parrinello MD simulations with DFT methods also reported the same result [187]. In an another DFT-MD simulation, a mixed dissociative and molecular adsorption of water molecules was found to be more stable [186]. Using the same techniques Zhang and Lindan [188, 189] simulated multilayer water adsorption on the rutile (110) surface. They reported that the presence of second-layer water could facilitate the proton transfer among the water molecules.

In the present study, MD techniques were used to simulate the vibrational spectra of water molecules in monolayer and double layer coverages on the clean rutile (110) and (100) surfaces. The calculated spectra were compared with the available literature data.

5.4.2 Models

The rutile (110) and (100) surfaces were modeled using the $\text{Ti}_{48}\text{O}_{96}$ (Figure 5.40a) and $\text{Ti}_{36}\text{O}_{72}$ (Figure 5.40b) two-dimensional cyclic clusters, respectively. The optimized bulk lattice parameters (Table 5.19) were used for these clusters. All atoms except those in the three bottom layers of these clusters were relaxed during geometry optimizations and MD simulations.

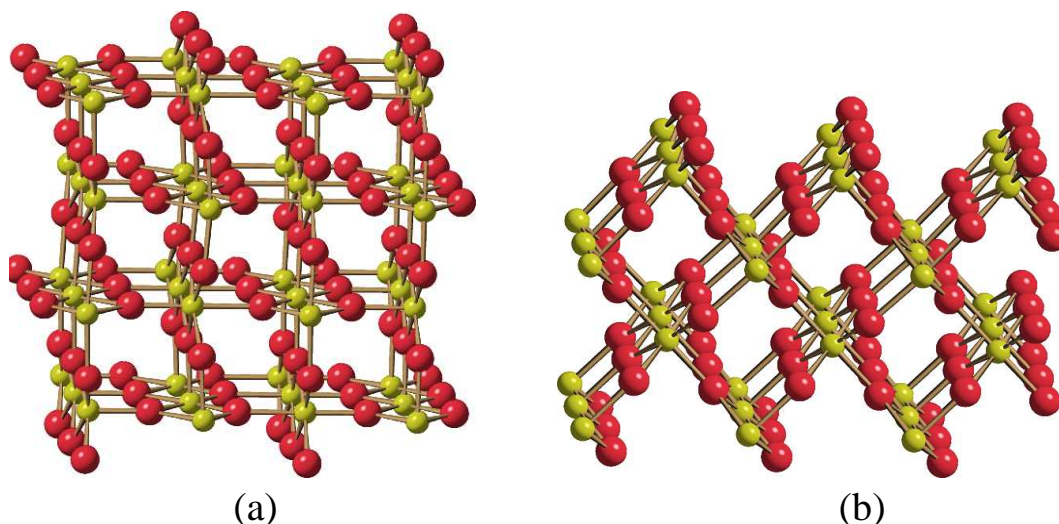


Figure 5.40: Clusters used to model the rutile (110) and (100) surfaces; (a) $\text{Ti}_{48}\text{O}_{96}$; (b) $\text{Ti}_{36}\text{O}_{72}$

5.4.3 Adsorption of an Isolated Water Molecule

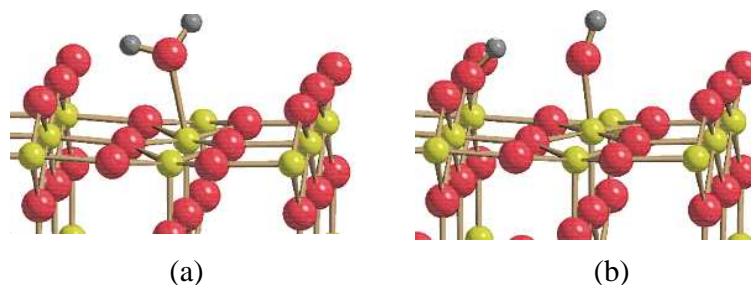


Figure 5.41: Optimized structures of an isolated water molecule adsorbed on the rutile (110)- $\text{Ti}_{48}\text{O}_{96}$ cluster; (a) molecular; (b) dissociative

Before studying the monolayer ($\theta=1$ or 1 ML) and the double layer ($\theta=2$ or 2 ML) water coverage, structure and adsorption energy of molecularly and dissociatively adsorbed isolated water molecules were calculated. A single water molecule was adsorbed molecularly on one of the five-fold coordinated titanium atoms of a relaxed $\text{Ti}_{48}\text{O}_{96}$ cluster. The optimized structure is shown in Figure 5.41a, and the adsorption energy E_{ads} is -119 kJ/mol (Table 5.25). For the dissociative adsorption (Figure 5.41b), the calculated E_{ads} is -226 kJ/mol (Table 5.25).

A single water molecule was adsorbed molecularly and dissociatively also on the rutile

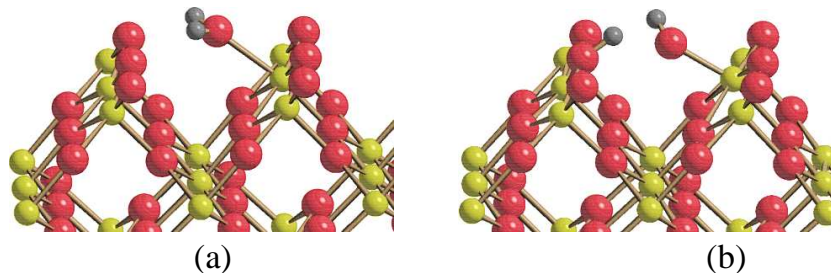


Figure 5.42: Optimized structures of an isolated water molecule adsorbed on the rutile (100)- $\text{Ti}_{36}\text{O}_{72}$ cluster; (a) molecular; (b) dissociative

(100)- $\text{Ti}_{36}\text{O}_{72}$ cluster as shown in Figures 5.42 a and b, respectively. The calculated E_{ads} for dissociative adsorption (-156 kJ/mol) was found to be lower than the molecular adsorption (-105 kJ/mol) (Table 5.25). Thus the dissociative adsorption of water molecule is thermodynamically favored on both the rutile (110) and (100) surfaces. For the (110) surface, the results are in agreement with the previous SINDO1 calculations [139].

Table 5.25: Calculated adsorption energies E_{ads} (kJ/mol) of a water molecule on rutile (110) and (100) surfaces in molecular and dissociative form

Surface	Adsorption type	Structure	E_{ads}
(110)	Molecular	5.41a	-119
	Dissociative	5.41b	-226
(100)	Molecular	5.42a	-105
	Dissociative	5.42b	-156

5.4.4 Monolayer Water Coverage

5.4.4.1 Rutile (110) Surface

There are six five-fold coordinated titanium atoms on the surface of the rutile (110)- $\text{Ti}_{48}\text{O}_{96}$ cluster. As five-fold coordinated titanium atoms are assumed to be the active centers for the adsorption of water molecules, $\theta=1$ corresponds to the adsorption of 6 water molecules.

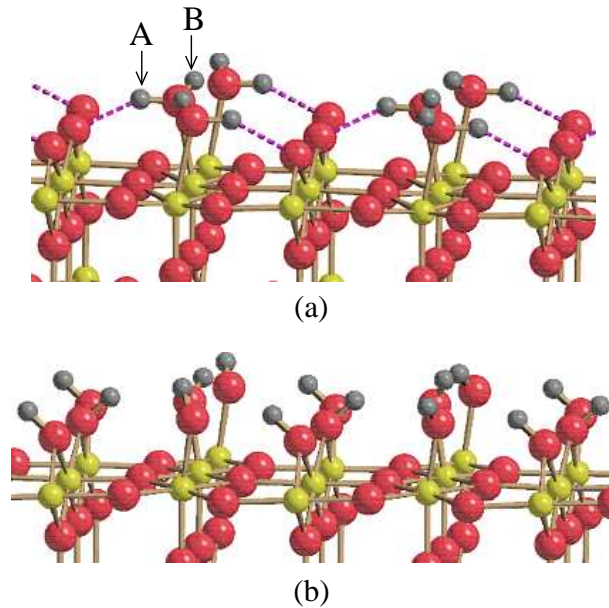


Figure 5.43: Structures of water molecules on rutile (110)-Ti₄₈O₉₆ cluster for $\theta=1$; (a) molecular; (b) dissociative

The energy minimum structure of molecularly adsorbed water molecules for $\theta=1$ is obtained using geometry optimization (Figure 5.43a). The water molecules are tilted alternatively to two different bridging oxygen atoms forming hydrogen bonds (Figure 5.43a). The calculated E_{ads} per water molecule for this structure is -128 kJ/mol. It is lower than the E_{ads} for a molecularly adsorbed isolated water molecule. Complete dissociation of the water molecules (Figure 5.43b) was found to be lower in energy. The estimated E_{ads} per water molecule for the completely dissociated structure (5.43b) is -163 kJ/mol, which is higher than that for the dissociatively adsorbed isolated water molecule. The adsorption structures with partial dissociation of monolayer water molecules were found to be less stable than the total dissociation. Thus a complete dissociation of the water molecules can occur on the (110) surface for $\theta = 1$.

To obtain the vibrational spectrum of the adsorbed water molecules, an MD simulation was performed. The temperature of the MD simulation was 100 K, which is close to the experimental temperature where the HREELS data were collected [176]. Constant temperature simulation was performed using the Nosé-Hoover chain thermostat. The thermostat frequency was 3600 cm⁻¹, which is close to the maximum frequency of the system. The time step used for the simulation was 1 fs.

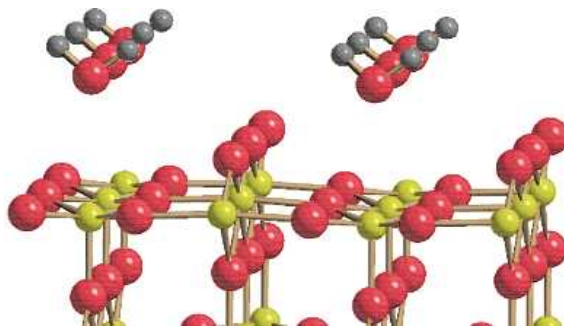


Figure 5.44: Starting structure for the MD simulation of 1 ML water on rutile (110) surface.

In the starting structure, water molecules were adsorbed about 3 Å away from the surface, on top of the five-fold coordinated titanium atoms (Figure 5.44). Simulation was not started from the optimized geometry to facilitate the crossing of any energy barriers. During the simulation, water molecules moved towards the surface and were bound to the five-fold coordinated titanium atoms. The adsorption structure after 2 ps was similar to structure (5.43a). No dissociation of water molecules was observed during the 6 ps of the simulation.

The vibrational density of states (VDOS) of the hydrogen atoms in the system was obtained by calculating the Fourier transform of their velocity auto correlation function (VACF) (see Eq. (3.47) in Section 3.1.4). The trajectories of the hydrogen atoms for the first 2 ps (2000 steps) of the simulation were not accounted for calculating the VACF due to the equilibration of the system. The estimated VDOS for the hydrogen atoms is shown in Figure 5.45a. There are three sets of peaks in the spectrum. The set of peaks around 1600 cm^{-1} corresponds to the bending modes of the adsorbed water molecules. The two sets of peaks, one about 3450 cm^{-1} and the other about 3610 cm^{-1} , are due to the O-H stretching vibrations.

From the VDOS, it is clear that two types of O-H groups are present in the system. VDOS was calculated separately for the hydrogen atoms which are pointing towards (type A) and pointing away (type B) from the bridging oxygen atoms. It was found that the peak at 3450 cm^{-1} is originating entirely from the type A hydrogen atoms (Figure 5.45b). Type B hydrogen atoms are giving the set of peaks around 3610 cm^{-1} (Figure 5.45c). This shows that hydrogen atoms of type A are hydrogen bonded to the bridging oxygen, which results in the red-shift of their stretching frequency. As there

is no red-shift for type B hydrogen atoms, it can be concluded that no intermolecular hydrogen bonding is formed between the type B hydrogen atoms to the neighboring water molecule.

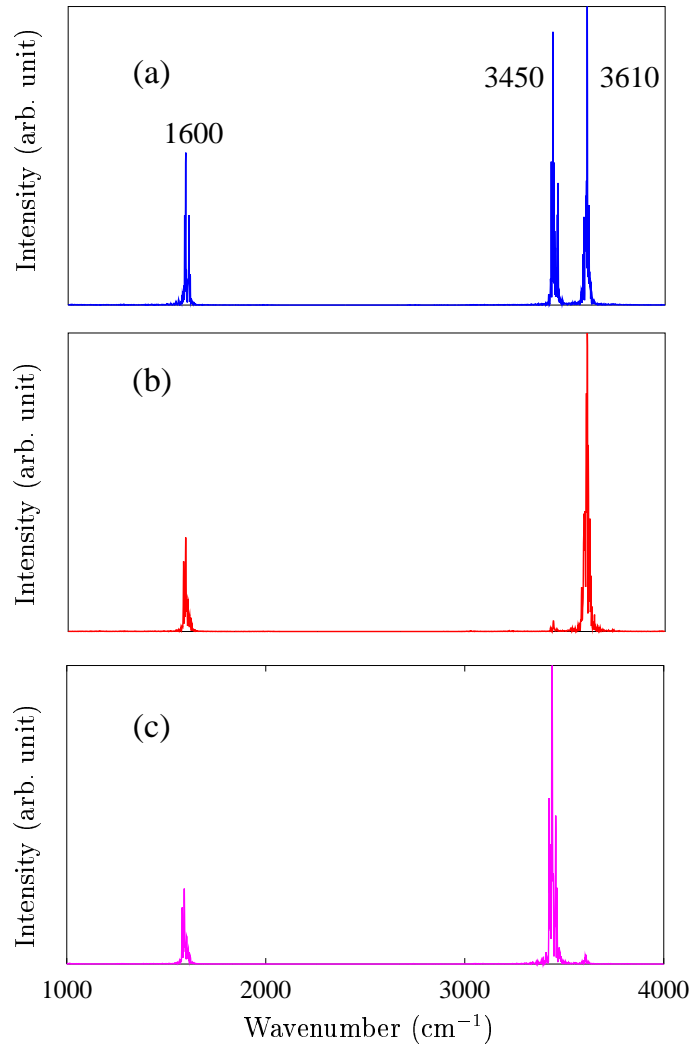


Figure 5.45: VDOS of hydrogen atoms estimated for molecularly adsorbed water molecules in monolayer saturation on the rutile (110) surface at 100 K; (a) all hydrogen atoms; (b) type A hydrogen atoms; (c) type B hydrogen atoms; see Figure 5.43a for labeling

The time scale of the above simulation was not large enough to obtain the global minimum structure (5.43b). In order to compare the VDOS of the molecularly adsorbed water molecules to the completely dissociated structure, an MD simulation starting with structure (5.43b) was performed at 100 K for 6 ps. No recombination of hydroxyls was observed in the simulation. The hydroxyl groups on the five-fold coordinated

atoms (terminal hydroxyls) were bending towards the hydrogen atoms on the bridging oxygen atoms (bridging hydroxyls). The VDOS of the hydrogen atoms was estimated as mentioned before.

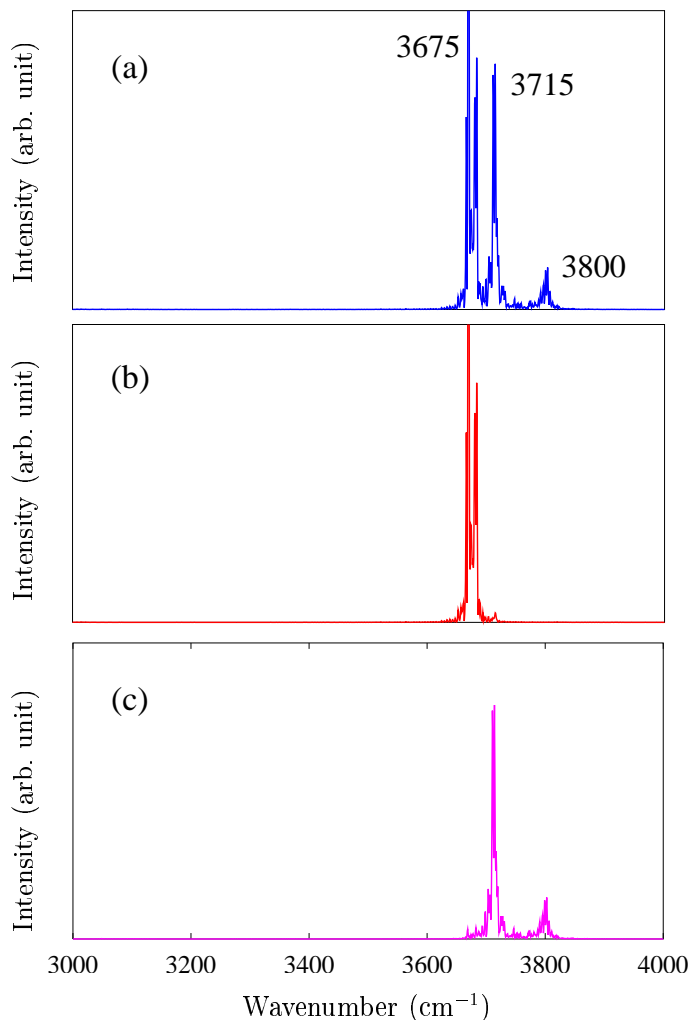


Figure 5.46: The VDOS of hydrogen atoms estimated for dissociatively adsorbed water molecules in monolayer saturation on the rutile (110) surface at 100 K; (a) all hydrogen atoms; (b) hydrogen atoms of bridging hydroxyls; (c) hydrogen atoms of terminal hydroxyls

In the vibrational spectrum, there are peaks at 3675 cm^{-1} , 3715 cm^{-1} and 3800 cm^{-1} (Figure 5.46a). When the VDOS for the bridging hydroxyls (Figure 5.46b) and terminal hydroxyls (Figure 5.46c) was estimated separately, it was found that the peak at 3675 cm^{-1} is due to the bridging hydroxyls and the peaks at 3715 cm^{-1} and 3800 cm^{-1} are due to terminal hydroxyl groups. Vibrational features of the terminal hydroxyl groups

appear at higher frequency compared to the bridging hydroxyl groups because the O-H bond in a terminal hydroxyl group is stronger than in a bridging hydroxyl group. The peak around 3800 cm^{-1} is of low intensity compared to the peak at 3715 cm^{-1} . The stretching frequencies of terminal hydroxyl groups are appearing at 3800 cm^{-1} , but are mostly red-shifted to 3715 cm^{-1} due to the hydrogen bonding interaction with the hydrogen atoms of the bridging hydroxyls.

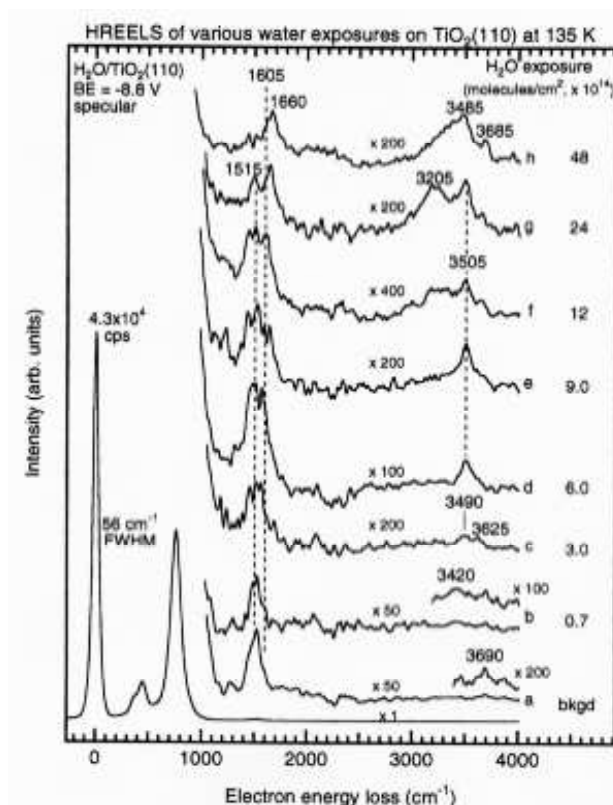


Figure 5.47: HREELS spectrum for various exposures of water adsorbed on the rutile (110) surface at 130 K; from Henderson [176]

From work function change measurements during water adsorption, Hugenschmidt et al. [150] reported that molecularly adsorbed water molecules are hydrogen bonded to the bridging oxygen atoms. This is in agreement with the present calculation. In the HREELS spectrum (Figure 5.47) for $\theta = 1$ on the rutile (110) surface (at 135 K), peaks are observed at 1605 cm^{-1} , 3490 cm^{-1} , and 3625 cm^{-1} [176]. This is in good agreement with the vibrational spectrum of the molecularly adsorbed monolayer water obtained in the present calculation (see Figure 5.45a). In Ref. [176], the peaks at 3490 cm^{-1} and 3625 cm^{-1} in the HREELS spectrum were attributed to the stretching vibrations of

non-hydrogen bonded O-H groups of molecularly adsorbed water molecules and non-hydrogen bonded O-H groups of dissociatively adsorbed water molecules, respectively. No peak in the HREELS spectrum was assigned as the stretching vibrations of the hydrogen bonded O-H groups. This might be due to the fact that the vibrational feature due to the non-hydrogen bonded O-H bonds of water molecules were not well resolved in the HREELS spectrum. For example, a broad peak can be only be observed from 3400 cm^{-1} to 3600 cm^{-1} at a coverage of 3×10^{14} molecules/ cm^2 in the HREELS spectrum (see Figure 5.47).

A peak at 3660 cm^{-1} found in the IR spectrum collected at room temperature was characterized as the stretching frequencies of the hydroxyl groups formed by the water dissociation [174]. The peak at 3690 cm^{-1} in the HREELS spectrum at 300 K was explained by the presence as non-hydrogen bonded hydroxyl groups on the surface [176]. The vibrational frequencies found for the bridging hydroxyl groups in the present work (3675 cm^{-1}) are in good agreement with these interpretations.

5.4.4.2 Rutile (100) Surface

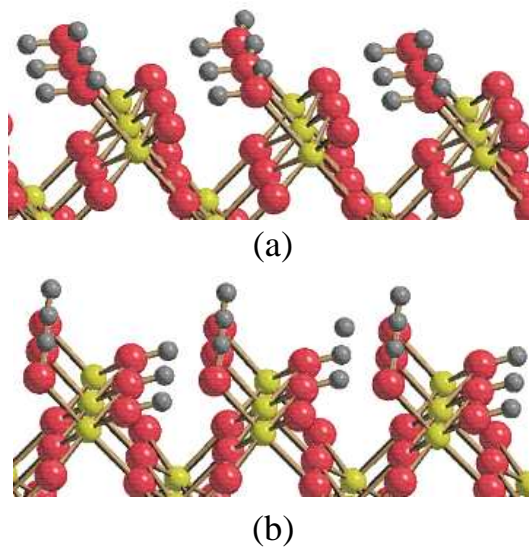


Figure 5.48: Structures of water molecules on the rutile (100)- $\text{Ti}_{36}\text{O}_{72}$ cluster for $\theta=1$;
(a) molecular; (b) dissociative

The adsorption of 1 monolayer of water molecules on the (100)- $\text{Ti}_{36}\text{O}_{72}$ cluster corresponds to the adsorption of 9 water molecules. First the relative stabilities of the completely dissociated and molecularly adsorbed monolayer coverage was calculated.

The obtained E_{ads} per water molecule for molecularly (Figure 5.48a) and dissociatively (Figure 5.48b) adsorbed water molecules were -133 kJ/mol and -176 kJ/mol, respectively. The adsorption energies of molecular and dissociative adsorption of 1 ML water molecules are lower than that for an isolated water molecule on this surface.

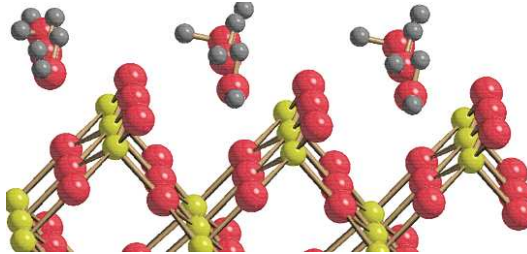


Figure 5.49: Starting structure of the MD simulation of 1 ML of water on the rutile (100)- $\text{Ti}_{36}\text{O}_{72}$ cluster

An MD simulation was then performed for this system. In the starting structure, water molecules were adsorbed nearly 2.5 Å above from the five-fold coordinated titanium atoms on the surface (Figure 5.49). The simulation was performed at 100 K for 6 ps. Technical details of the simulation are the same as before. During the simula-

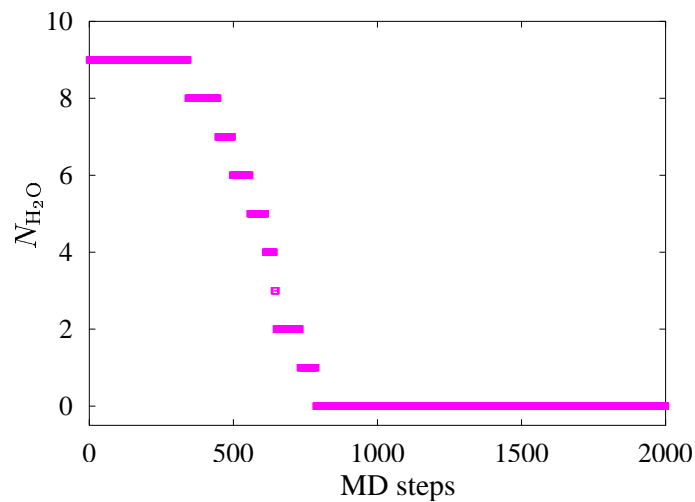


Figure 5.50: Number of undissociated water molecules ($N_{\text{H}_2\text{O}}$) during the MD simulation of water molecules on the rutile (100)- $\text{Ti}_{36}\text{O}_{72}$ cluster at monolayer coverage

tion, the water molecules moved towards the five-fold coordinated titanium atoms and dissociated on the neighboring two-fold coordinated oxygen atoms.

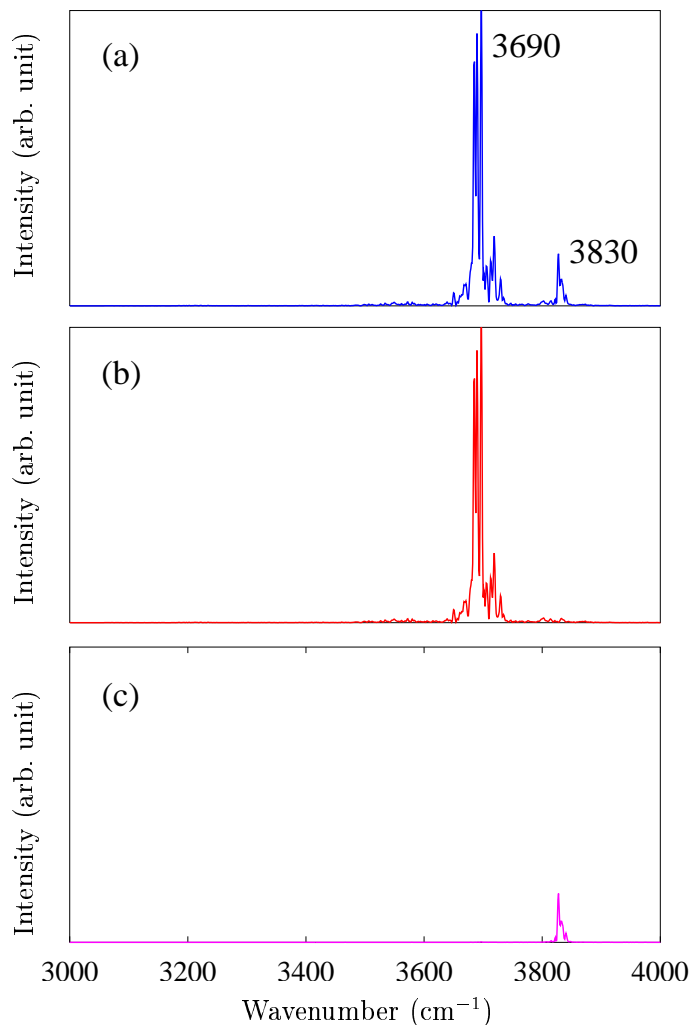


Figure 5.51: The VDOS of hydrogen atoms estimated for dissociatively adsorbed water molecules in monolayer coverage on the rutile (100) surface at 100 K; (a) all hydrogen atoms; (b) hydrogen atoms of bridging hydroxyls; (c) hydrogen atoms of terminal hydroxyls

The number of undissociated water molecules during the MD simulation is shown in Figure 5.50. Dissociation of water molecules started after 0.4 ps (400 steps) and all nine water molecules were dissociated within 0.7 ps (700 steps) of the simulation (Figure 5.50). The rutile (100) surface is highly reactive towards the adsorbing water molecules compared to the (110) surface. This is also observed experimentally [180]. The high reactivity is due its peculiar surface structure. The hydrogen atoms of the water molecules adsorbed on the five-fold coordinated titanium atoms are much closer to the neighboring bridging oxygen atoms compared to the (110) surface. Lattice vibrations

of the rutile (100) surface can make this distance small enough to facilitate the water dissociation.

The VDOS of the completely dissociated water molecule was then calculated (Figure 5.51a). For the calculation of the VDOS, the trajectories of the hydrogen atoms were considered only for the last 4 ps, since the system was equilibrating in the first 2 ps of the simulation. In the obtained VDOS there were mainly two sets of peaks, one about 3690 cm^{-1} and the other about 3830 cm^{-1} . The hydrogen atoms of the bridging hydroxyl groups were responsible for the peak at 3690 cm^{-1} (Figure 5.51a). The peak at about 3830 cm^{-1} (Figure 5.51b) was due to the terminal hydroxyl groups. These frequencies are close to those observed for the hydroxyl groups on the rutile (110) surface. Compared to the peak at 3690 cm^{-1} , the intensity of the peak at 3830 cm^{-1} is considerably lower. As equal numbers of bridging and terminal hydroxyl groups are present in the system, their intensities should also be the same. The very low intensity at 3830 cm^{-1} is probably due to the effect of the vibrations of the five-fold coordinated surface titanium atoms which screen the O-H vibrations.

5.4.5 Double Layer Water Coverage

5.4.5.1 Rutile (110) Surface

Double layer water coverage on the rutile (110)- $\text{Ti}_{48}\text{O}_{96}$ cluster was simulated by the adsorption of 12 water molecules. The calculated energy minimum structure for undissociated first-layer water molecules is given in Figure 5.52a. In this structure the water molecules in the first-layer are tilted towards the bridging oxygen atoms and are hydrogen bonded. Water molecules in the second-layer are also hydrogen bonded to the bridging oxygen atoms. Another adsorption structure was also considered (Figure 5.52b) where the first-layer water molecules are completely dissociated. This structure is 99 kJ/mol lower in energy than the structure (5.52a).

An MD simulation was performed at 100 K starting from the structure shown in Figure 5.53. In this structure the water molecules in the first-layer are 3.0 \AA away from the five-fold coordinated titanium atoms and the second-layer water molecules are 3.0 \AA away from the bridging oxygen atoms. The technical details of the simulation are the same as before. During the simulation, the water molecules moved towards the surface

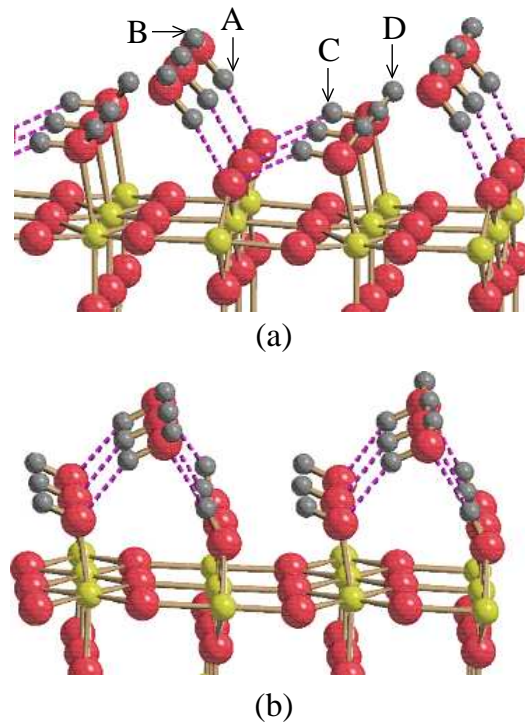


Figure 5.52: Structures of water molecules on the rutile (110)- $\text{Ti}_{48}\text{O}_{96}$ cluster for $\theta=2$; (a) molecular; (b) dissociative adsorption of first-layer water molecules

and a structure similar to Figure 5.52a was formed within 1 ps of the simulation. Dissociation of the first-layer or desorption of the second-layer water molecules was not observed during the 6 ps of the simulation at 100 K. Desorption was not expected, as the TPD data [150, 176] show that desorption of the second-layer water molecules occur at about 180 K.

In the adsorbate structure (5.52a), there are four types of hydrogen atoms. Those in the second-layer which are pointing towards the bridging oxygen atoms will be called type A. The other set of hydrogen atoms in the second-layer will be called type B hydrogen atoms. The hydrogen atoms of the first-layer water molecules which are pointing towards the bridging oxygen atoms will be called type C, and the others type D hydrogen atoms. The VDOS of the hydrogen atoms in the system was obtained from their trajectories for 4 ps. In the calculated VDOS (Figure 5.54a) there are peaks at 1625 cm^{-1} , 1700 cm^{-1} , and a broad maximum from 3500 cm^{-1} to 3700 cm^{-1} . The peaks at 1625 cm^{-1} , and 1700 cm^{-1} are due to the bending modes of water molecules. By simulating the VDOS of the hydrogen atoms in the first (Figure 5.54d,e) and second

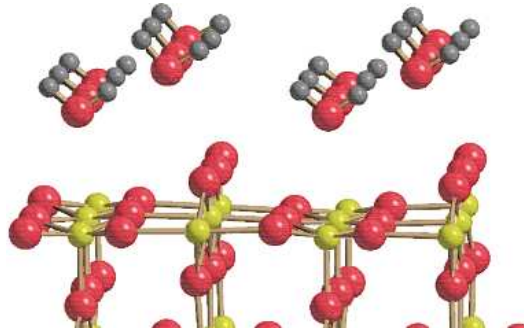


Figure 5.53: Starting structure of the MD simulation of 2 ML of water on the rutile (110)-Ti₄₈O₉₆ cluster

(Figure 5.54b,c) layer separately, it was found that the bending mode of first layer water molecules was at lower wavenumbers (1620 cm^{-1}) than that of the second-layer water molecules (1700 cm^{-1}). The peaks from 3600 cm^{-1} to 3650 cm^{-1} (Figure 5.54b) are due to type A hydrogen atoms while the type B hydrogen atoms show their vibrational features from 3610 cm^{-1} to 3700 cm^{-1} (Figure 5.54c). The stretching frequencies of the O-H bonds with type C and type D hydrogen atoms are at 3500 cm^{-1} (Figure 5.54d) and 3600 cm^{-1} (Figure 5.54e), respectively.

In the HREELS spectrum reported by Henderson [176], bending modes of water molecules were observed at 1605 cm^{-1} and 1660 cm^{-1} for 2 ML coverage (see spectrum in Figure 5.47 for 9.0×10^{14} molecules/cm² water coverage). This peak at 1660 cm^{-1} in the experiment corresponds to the peak at 1700 cm^{-1} in the present calculation. It was found in the experiment that the O-H stretching frequency of the first-layer water molecules is not affected by the second-layer water molecules. A frequency of 3505 cm^{-1} was obtained in the HREELS spectrum (Figure 5.47e) is in very good agreement with the present calculation (3500 cm^{-1}). The O-H stretching frequencies of second-layer water molecules (Figure 5.54b,c) are observed above 3600 cm^{-1} . This shows that their interactions with the bridging surface oxygen atoms are weak compared to that of the first-layer water molecules. This agrees with the experimental conclusion that the second-layer water molecules interact only weakly with the surface [150,176]. A small red-shift in the stretching frequencies of the O-H bonds with type B hydrogen atoms (see Figure 5.54c) shows the presence of a weak interaction between the second-layer water molecules during their vibrational motions.

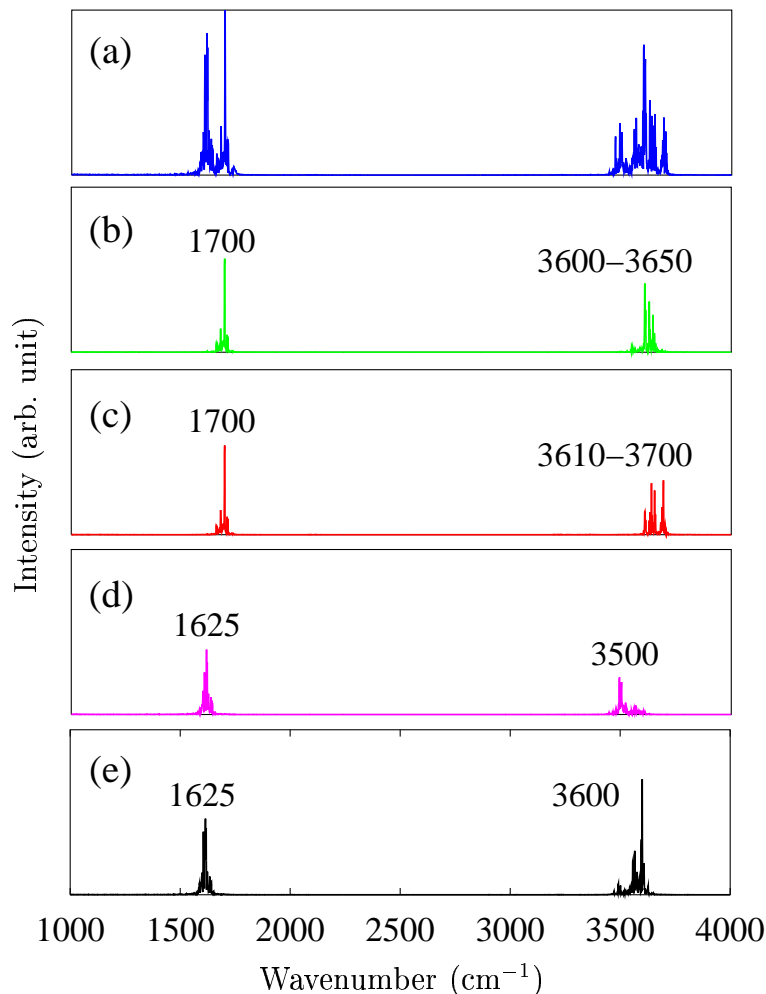


Figure 5.54: The VDOS of 2 ML of molecularly adsorbed water molecules on rutile (110) surface at 100 K; (a) all hydrogen atoms; (b) type A hydrogen atoms; (c) type B hydrogen atoms; (d) type C hydrogen atoms; (e) type D hydrogen atoms; see Figure 5.52a for labeling

5.4.5.1 Rutile (100) Surface

A second-layer water model was constructed by placing 18 water molecules on top of the (100)- $\text{Ti}_{36}\text{O}_{72}$ cluster. Relative energies of molecularly and dissociatively adsorbed water molecules were studied first. The structure with completely dissociated first-layer water molecules (Figure 5.55a) is 376 kJ/mol lower in energy than the structure with molecularly adsorbed first-layer water molecules (Figure 5.55b).

An MD simulation was performed at 100 K starting with the structure (5.56). First-layer water molecules are 2.5 Å away from the five-fold coordinated titanium atoms

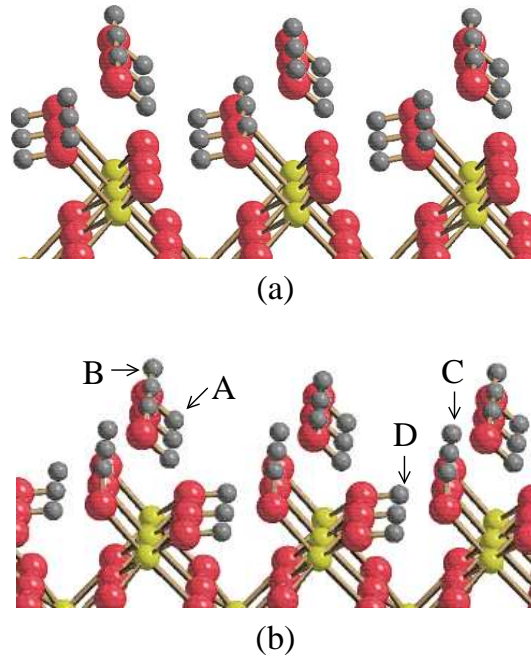


Figure 5.55: Structures of water molecules on the rutile (100)- $\text{Ti}_{36}\text{O}_{72}$ cluster for $\theta=2$;
 (a) molecular; (b) dissociative adsorption of first-layer water molecules

and the second-layer water molecules are 3 \AA away from the bridging oxygen atoms. Technical details of the simulation are the same as before. During the MD simulation, first-layer water molecules bind to the five-fold coordinated titanium atoms. But the second-layer water molecules were desorbing from the surface during the simulation. The average distance, $r(\text{O}^{1\text{ML}} - \text{O}^{2\text{ML}})$, between the oxygen atoms of the first- and the second-layer water molecules is shown in Figure 5.57. For the initial structure, $r(\text{O}^{1\text{ML}} - \text{O}^{2\text{ML}})$ was about 2.2 \AA . After 2000 steps of the simulation this distance was about 4.7 \AA . This clearly indicates that the second-layer water molecules were desorbed from the surface. In contrast, in the TPD experiment the major part of the second-layer water molecules were found to desorb only at higher temperatures at about 160 K [180]. In the structure (5.56), the interaction of the second-layer water molecules to the surface atoms are weak and thus they desorbed at 100 K. Instead of starting from an arbitrary structure, a second MD simulation was performed at 100 K with the energy minimum structure (5.55b), where the the second-layer water molecules are near the surface oxygen atoms. During this simulation for 6 ps, no desorption of the second-layer water molecules was observed.

The VDOS of the hydrogen atoms was obtained from this simulation (see Figure 5.58a).

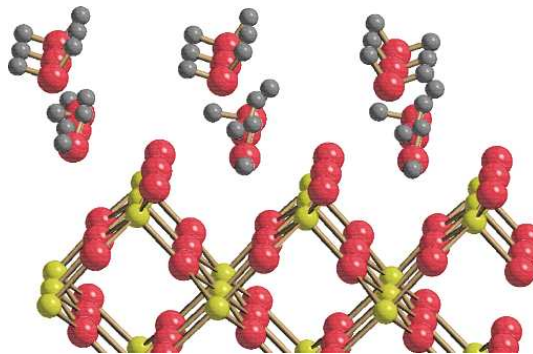


Figure 5.56: Starting structure of the MD simulation of 2 ML of water on the rutile (100)- $\text{Ti}_{36}\text{O}_{72}$ cluster

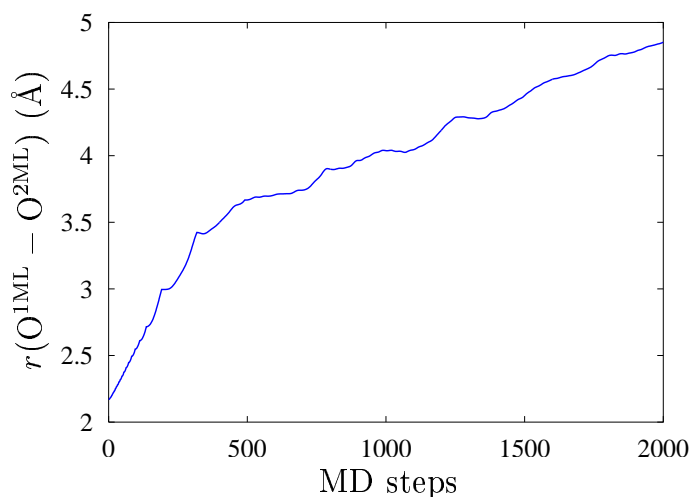


Figure 5.57: Average distance $r(\text{O}^{1\text{ML}} - \text{O}^{2\text{ML}})$ between the oxygen atoms of the first- and the second-layer water molecules on the (100) surface at 100 K.

The hydrogen atoms which are pointing towards the surface and the other hydrogen atoms in the second-layer water molecules of structure (5.55a) will be called type A and type B hydrogen atoms, respectively. The hydrogen atoms in the terminal hydroxyl groups will be called type C and those in the bridging hydroxyl groups will be called type D. The peak at 1695 cm^{-1} is due to the bending modes of second-layer water molecules (see Figure 5.58b and Figure 5.58c). The stretching frequency of the bridging hydroxyl groups in the second-layer water molecules is mostly appearing at 3650 cm^{-1} . The red-shifted peak at 3560 cm^{-1} is due to the stretching of the hydroxyl groups with type A hydrogen atoms. It has a low intensity compared to the peak at 3650 cm^{-1} (Figure 5.58b). This indicates that the interaction of the second-layer water

molecules with the surface is weak. During the vibrational motion of the second-layer water molecules, type A hydrogen atoms are forming hydrogen bonds with the bridging oxygen atoms. The stretching frequency of the bridging hydroxyl groups is around at 3550 cm^{-1} (Figure 5.58e), which is lower than that observed for the bridging hydroxyl groups (3690 cm^{-1}) for $\theta = 1$ on the rutile (100) surface (Figure 5.51b). This is due to the interaction of the second-layer water molecules with the bridging oxygen atoms. The vibrational feature due to the stretching of the terminal hydroxyl groups appears at 3725 cm^{-1} (Figure 5.51d).

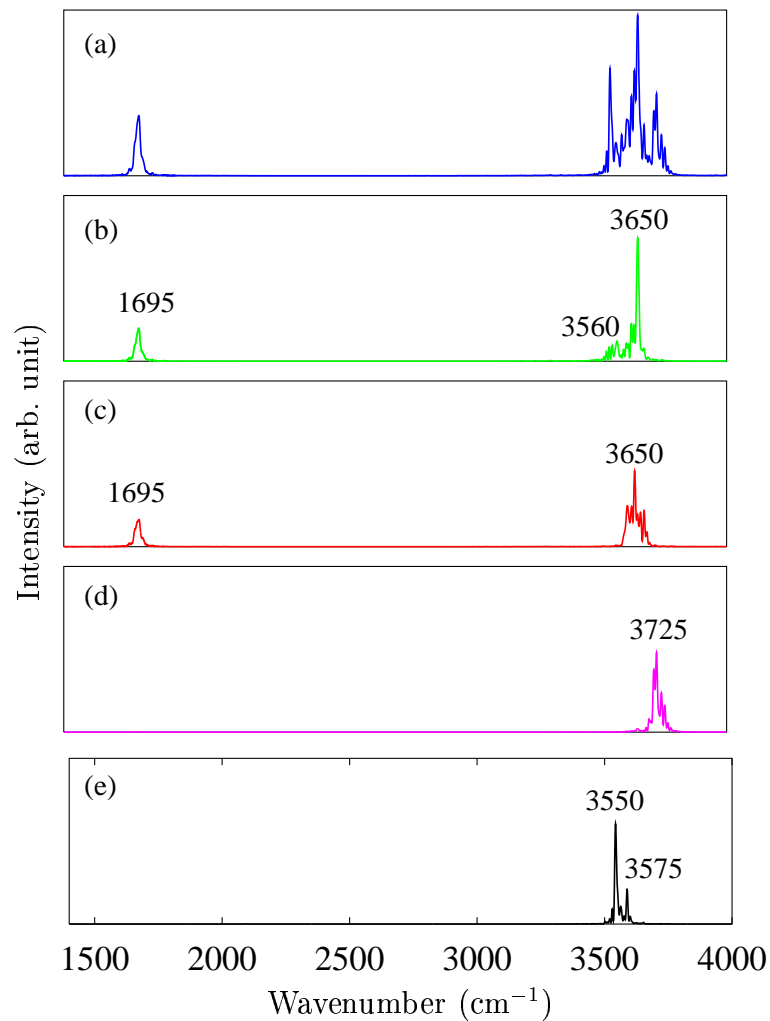


Figure 5.58: The VDOS of hydrogen atoms estimated for 2 ML water coverage with the first-layer water molecules dissociated on the rutile (100) surface at 100 K; (a) all hydrogen atoms; (b) type A; (c) type B; (d) type C; (e) type D hydrogen atoms; see Figure 5.55b for labeling

5.5 Mixing of Zinc Oxide and Zinc Sulfide

5.5.1 Introduction

Wide and direct band semiconductor materials like zinc chalcogenides are used in blue and ultraviolet optical devices. Doped zinc chalcogenides are employed for designing various electronic and electrical appliances. Materials with required optical properties can be produced by mixing different zinc chalcogenides.

Mixing of two different zinc chalcogenides, say ZnA and ZnB, would result in a solid solution $\text{ZnA}_{1-x}\text{B}_x$.



The stability of a solid solution is determined by its free energy of mixing $\Delta_{\text{M}}G$.

$$\Delta_{\text{M}}G = \Delta_{\text{M}}H - T\Delta_{\text{M}}S \quad (5.85)$$

Here $\Delta_{\text{M}}H$ is the enthalpy of mixing, $\Delta_{\text{M}}S$ is the free energy of mixing and T is the temperature. Miscibility will not occur if $\Delta_{\text{M}}G$ is positive.

The entropy of mixing $\Delta_{\text{M}}S$ consists of configurational entropy, $\Delta_{\text{M}}S_{\text{conf}}$ and thermal entropy, $\Delta_{\text{M}}S_{\text{ther}}$.

$$\Delta_{\text{M}}S = \Delta_{\text{M}}S_{\text{conf}} + \Delta_{\text{M}}S_{\text{ther}} \quad (5.86)$$

By assuming that mixing in (5.84) leads to an ideal solution, $\Delta_{\text{M}}S_{\text{conf}}$ is estimated as

$$\Delta_{\text{M}}S_{\text{conf}} = -R(1-x)\ln(1-x) - Rx\ln(x) \quad (5.87)$$

where R is the gas constant. $\Delta_{\text{M}}S_{\text{ther}}$ is evaluated for the reaction (5.84) as,

$$\Delta_{\text{M}}S_{\text{ther}} = S(\text{ZnA}_{1-x}\text{B}_x) - (1-x)S(\text{ZnA}) - xS(\text{ZnB}) \quad (5.88)$$

Entropy S can be evaluated using MD techniques (see Section 3.1.4).

Solid solutions $\text{ZnS}_{1-x}\text{Se}_x$ produced by the mixing of ZnS and ZnSe were found to be stable for all possible values of x ($0 < x < 1$) [190, 191]. The stability of $\text{ZnS}_{1-x}\text{Se}_x$ is due to similar sizes of the anions. But due to the difference in the sizes of oxygen and sulfur, a miscibility gap is expected for ZnO and ZnS. Yoo et al. [192] produced $\text{ZnO}_{1-x}\text{S}_x$ with very low concentration of S ($x \approx 0.03$) at ~ 1000 K using laser ablation techniques. Binnewies and Locmelis [193] prepared ZnO/ZnS mixed crystals with low sulfur content ($x \approx 0.01$) at ~ 1200 K.

Using MSINDO-CCM, Janetzko and Jug [194] investigated the miscibility of ZnS with ZnSe and ZnO. They found that ZnS and ZnSe can mix for all possible values of x between 0 and 1. But a miscibility gap was observed for ZnS and ZnO at 1000 K. The latter result is in contradiction to the experimental observation that small concentration of ZnS can mix with ZnO [192, 193].

In the calculations of Janetzko and Jug [194], thermal entropic contributions were not included ($\Delta_{\text{M}}S_{\text{ther}} = 0$) and the enthalpy of mixing $\Delta_{\text{M}}H$ was approximated as energy of mixing, $\Delta_{\text{M}}E_0$.

$$\Delta_{\text{M}}H \approx \Delta_{\text{M}}E_0$$

For the reaction (5.84), $\Delta_{\text{M}}E_0$ is given by

$$\Delta_{\text{M}}E_0 = E_0(\text{ZnA}_{1-x}\text{B}_x) - (1-x)E_0(\text{ZnA}) - xE_0(\text{ZnB}) \quad (5.89)$$

Here E_0 is the total energy obtained from quantum chemical calculation.

The present work is aimed to study the effect of the thermal entropic contribution to the free energy of mixing for ZnO and ZnS. The entropy of mixing calculated by Janetzko and Jug [194] is improved by the inclusion of thermal entropy. Thermal entropy is estimated from MD simulations using a quantum-classical approach described in Section 3.1.4.

5.5.2 Bulk Properties

ZnO (wurzite) has a hexagonal unit cell where zinc and oxygen ions are tetrahedrally coordinated (space group $P6_3mc$). The lattice parameters a , c and u for ZnO are 3.198 Å, 5.185 Å, and 0.378, respectively [195]. The band gap of ZnO is 3.44 eV [196]. At temperatures below 1200 K and 1 atm pressure, ZnS prefers to have cubic sphalerite structure (space group $F\bar{4}3m$). Similar to ZnO, zinc and oxygen atoms have tetrahedral coordination in ZnS. The experimentally determined lattice parameter a for ZnS is 5.410 Å [197]. The band gap of ZnS (3.85 eV) [198] is slightly higher than ZnO (3.44 eV).

Bulk properties of ZnO and ZnS were calculated using three-dimensional CCM calculations in the framework of MSINDO. In the calculations, some of the standard MSINDO parameters for Zn and S [14] were modified as explained in Ref. [194]. The screening

parameters $K_{\text{SC}}(3d)$, $K_{\text{SC}}(4s)$, and $K_{\text{SC}}(4p)$ for Zn are -0.0048, 0.0080, and 0.0331, respectively. The parameter $\kappa(4s4p3d)$ for Zn is 0.1230. The parameters $K_{\text{SC}}(3d)$ and $\kappa(4s4p3d)$ for S, used in the calculations are 0.0286 and 0.0281, respectively.

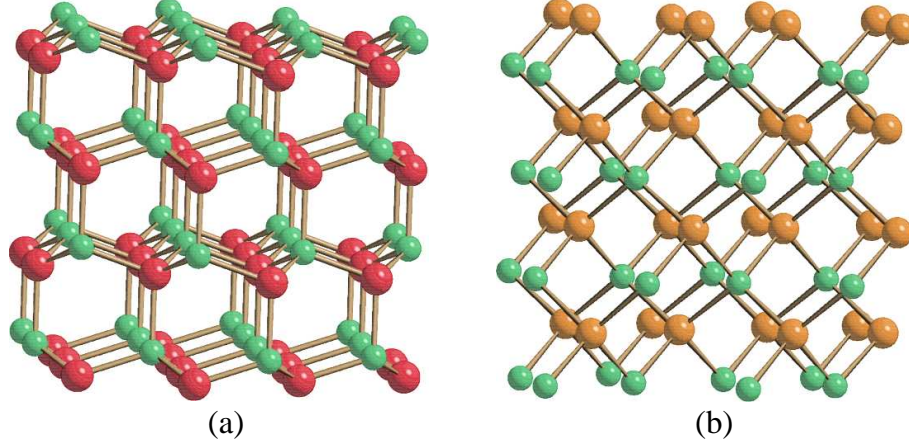


Figure 5.59: Cyclic clusters used for the simulation of ZnO and ZnS bulk; (a) $\text{Zn}_{48}\text{O}_{48}$ and (b) $\text{Zn}_{32}\text{O}_{32}$. Here green, red, and orange colored spheres represent zinc, oxygen and sulfur atoms, respectively.

For simulating the ZnO and ZnS bulk three-dimensional cyclic $\text{Zn}_{48}\text{O}_{48}$ (Figure 5.59a) and $\text{Zn}_{32}\text{O}_{32}$ (Figure 5.59b) clusters were chosen, respectively. In the previous study [194], these clusters were found to give converged bulk properties. The optimized cell parameters for ZnO are $a = 3.198 \text{ \AA}$, $b = 5.185 \text{ \AA}$, $u = 0.378$ and the estimated band gap is 3.48 eV. For ZnS, the optimized lattice parameter is 5.372 \AA . Thus the results from the MSINDO-CCM calculations are in good agreement with the experimental results (see Table 5.26).

The substituted clusters considered in the present work are $\text{Zn}_{48}\text{O}_{47}\text{S}$ and $\text{Zn}_{32}\text{S}_{31}\text{O}$. They correspond to $\text{ZnO}_{0.98}\text{S}_{0.02}$ and $\text{ZnO}_{0.03}\text{S}_{0.97}$ systems, with x equal to 0.02 and 0.97, respectively. Their optimized lattice parameters are given in Table 5.27. The lattice parameters a and c for $\text{ZnO}_{0.98}\text{S}_{0.02}$ are 3.208 \AA and 5.204 \AA , respectively. The calculated unit cell parameter for $\text{ZnO}_{0.03}\text{S}_{0.97}$ cluster is $a = 5.342 \text{ \AA}$.

5.5.3 Entropy and Free Energy of Mixing

As the mixing of ZnO and ZnS was observed at $\sim 1000 \text{ K}$ in the experiments [192, 193], calculations were also performed at 1000 K . To estimate the entropy, a canonical

Table 5.26: Lattice parameters a , c (Å), internal parameter u , and band gap E_g (eV) for ZnO and ZnS calculated using the MSINDO-CCM by Janetzko and Jug [194]. These results are also compared with the experimental data.

System	Cluster		Unit cell parameters		Band gap	
			MSINDO	Experiment	MSINDO	Experiment
ZnO	Zn ₄₈ O ₄₈	a	3.198	3.253 ^a	3.67	3.44 ^b
		c	5.185	5.213 ^a		
		u	0.378	0.382 ^a		
ZnS	Zn ₃₂ O ₃₂	a	5.372	5.410 ^c	3.48	3.85 ^d

^a Ref. [195]

^b Ref. [196]

^c Ref. [197]

^d Ref. [198]

Table 5.27: Lattice parameters a , c (Å) for ZnO_{1-x}S_x mixed systems.

System	Cluster	Lattice parameters
ZnO _{0.98} S _{0.02}	Zn ₄₈ O ₄₇ S	$a = 3.208$
		$c = 5.204$
ZnO _{0.03} S _{0.97}	Zn ₃₂ S ₃₁ O	$a = 5.342$

ensemble simulation was performed using the Nosé-Hoover chain thermostat. The time step of the simulation was 0.5 fs. For accurate determination of the entropy, a smaller time step was used in the calculations compared to that in the previous sections (1 fs). The frequency of the thermostat was 750 cm⁻¹, which is close to the maximum vibrational frequency of the bulk.

The entropy of ZnO was estimated by using the three-dimensional cyclic Zn₄₈O₄₈ cluster. The system was equilibrated for 2000 steps at 1000 K. This was followed by an MD run for 12000 steps (6 ps) from which the vibrational density of states of ZnO was obtained by the Fourier transform of the mass weighted atomic velocities using Eq. (3.60). The entropy was evaluated using the vibrational density of states according to Eq. (3.60). Convergence of the entropy with respect to number of MD steps is shown in Figure 5.60 and Table 5.28. After 12000 steps of the simulation, fluctuations in

entropy were below $< 0.1 \text{ J mol}^{-1} \text{ K}^{-1}$. Thus the entropy of ZnO is taken as $95.0 \text{ J mol}^{-1} \text{ K}^{-1}$. The deviation from the experimental value ($100.8 \text{ J mol}^{-1} \text{ K}^{-1}$) [199] is only about -6 % (Table 5.28).

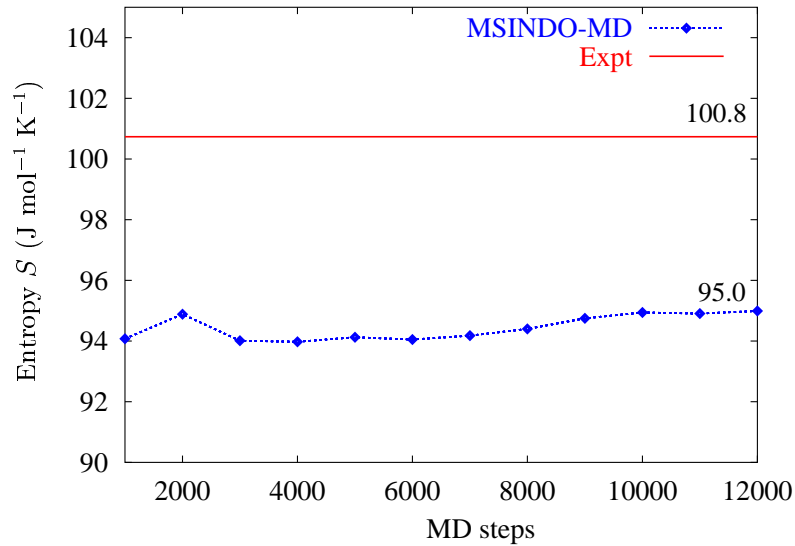


Figure 5.60: Convergence of entropy S at 1000 K for the ZnO crystal with respect to number of MD steps. Red line is the experimental estimate of entropy and the blue points are the entropy estimated using MSINDO-MD simulations.

Table 5.28: Convergence of entropy S ($\text{J mol}^{-1} \text{ K}^{-1}$) at 1000 K for the ZnO crystal with respect to the number of MD steps.

MD steps	S
1000	94.074
2000	94.882
3000	94.010
4000	93.976
5000	94.123
6000	94.048
7000	94.178
8000	94.400
9000	94.747
10000	94.940
11000	94.904
12000	94.990

The same procedure was used to estimate the entropy of other systems. Using a three-dimensional cyclic $\text{Zn}_{32}\text{S}_{32}$ cluster the entropy was calculated to be $106.5 \text{ J mol}^{-1} \text{ K}^{-1}$. This value deviates about -11% from the experimental result ($118.0 \text{ J mol}^{-1} \text{ K}^{-1}$) [199]. Thus the estimated entropy values for ZnO and ZnS are in reasonable agreement with the experiment (see Table 5.28). Entropies of $\text{ZnO}_{0.98}\text{S}_{0.02}$, and $\text{ZnO}_{0.03}\text{S}_{0.97}$ systems were evaluated using three-dimensional cyclic $\text{Zn}_{48}\text{O}_{47}\text{S}$ and $\text{Zn}_{32}\text{S}_{31}\text{O}$ clusters, respectively. The estimated entropies for $\text{ZnO}_{0.98}\text{S}_{0.02}$ and $\text{ZnO}_{0.03}\text{S}_{0.97}$ are $95.3 \text{ J mol}^{-1} \text{ K}^{-1}$ and $107.6 \text{ J mol}^{-1} \text{ K}^{-1}$, respectively.

Table 5.29: MSINDO-MD results for the entropy S ($\text{J mol}^{-1} \text{ K}^{-1}$) at 1000 K for ZnO, ZnS, $\text{ZnO}_{0.98}\text{S}_{0.02}$ and $\text{ZnS}_{0.97}\text{O}_{0.03}$ systems; results are compared with the available literature data.

System	Cluster	S	
		MSINDO-MD	Experiment ^a
ZnO	$\text{Zn}_{48}\text{O}_{48}$	95.0	100.8
ZnS	$\text{Zn}_{32}\text{S}_{32}$	106.5	118.0
$\text{ZnO}_{0.98}\text{S}_{0.02}$	$\text{Zn}_{48}\text{O}_{47}\text{S}$	95.3	-
$\text{ZnO}_{0.03}\text{S}_{0.97}$	$\text{Zn}_{32}\text{S}_{31}\text{O}$	107.6	-

^a Ref. [199]

The thermal entropy for mixing $\Delta_{\text{M}}S_{\text{ther}}$ was estimated for $\text{ZnO}_{0.98}\text{S}_{0.02}$ and $\text{ZnO}_{0.03}\text{S}_{0.97}$ according to Eq. (5.88). For $\text{ZnO}_{0.98}\text{S}_{0.02}$ system $\Delta_{\text{M}}S_{\text{ther}}$ was $0.03 \text{ J mol}^{-1} \text{ K}^{-1}$. $\Delta_{\text{M}}S_{\text{ther}}$ is smaller compared to the configurational entropy $\Delta_{\text{M}}S_{\text{conf}}$ for this system ($0.81 \text{ J mol}^{-1} \text{ K}^{-1}$). The contribution of $\Delta_{\text{M}}S_{\text{ther}}$ to the total entropy is very small (4%). For the $\text{ZnS}_{0.97}\text{O}_{0.03}$ system, $\Delta_{\text{M}}S_{\text{ther}}$ is $1.42 \text{ J mol}^{-1} \text{ K}^{-1}$. This value is higher than $\Delta_{\text{M}}S_{\text{conf}}$ of this system ($1.12 \text{ J mol}^{-1} \text{ K}^{-1}$). Contribution of $\Delta_{\text{M}}S_{\text{ther}}$ to the total entropy of the system is about 56%.

The free energies of mixing are evaluated for the two mixed systems, $\text{ZnO}_{0.98}\text{S}_{0.02}$ and $\text{ZnO}_{0.03}\text{S}_{0.97}$. Without including the thermal entropy the free energies of mixing $\Delta_{\text{M}}G_{\text{old}}$ for $\text{ZnO}_{0.98}\text{S}_{0.02}$ and $\text{ZnO}_{0.03}\text{S}_{0.97}$ are 0.95 kJ/mol and 2.01 kJ/mol , respectively. The free energy of mixing $\Delta_{\text{M}}G_{\text{corr}}$ including the thermal entropic contribution for $\text{ZnO}_{0.98}\text{S}_{0.02}$ system was 0.92 kJ/mol . The inclusion of thermal entropy has only small influence in the free energy of mixing. But for the $\text{ZnS}_{0.97}\text{O}_{0.03}$ system, the free energy

of mixing is lowered by about 1.42 kJ/mol by the inclusion of thermal entropy (see Table 5.30).

Table 5.30: The estimated values of $\Delta_M E_0$ (kJ/mol), $\Delta_M S_{\text{conf}}$ ($\text{J mol}^{-1} \text{K}^{-1}$), $\Delta_M S_{\text{ther}}$ ($\text{J mol}^{-1} \text{K}^{-1}$), $\Delta_M G_{\text{old}}$ (kJ/mol), $\Delta_M G_{\text{corr}}$ (kJ/mol) for $\text{ZnO}_{0.98}\text{S}_{0.02}$ and $\text{ZnS}_{0.97}\text{O}_{0.03}$; Here $\Delta_M G_{\text{corr}}$ and $\Delta_M G_{\text{old}}$ are the free energies of mixing with and without thermal entropy contributions, respectively.

System	x	$\Delta_M E_0$	$\Delta_M S_{\text{conf}}$	$\Delta_M S_{\text{ther}}$	$\Delta_M G_{\text{old}}$	$\Delta_M G_{\text{corr}}$
$\text{ZnO}_{0.98}\text{S}_{0.02}$	0.02	1.76	0.81	0.03	0.95	0.92
$\text{ZnS}_{0.97}\text{O}_{0.03}$	0.97	3.13	1.12	1.42	2.01	0.59

Thus the present calculations show that the thermal entropic contribution to the free energy of mixing is not large enough to bring the free energy of mixing to negative values.

6 Summary

The Born-Oppenheimer MD was implemented in the semiempirical SCF MO method MSINDO. Integration of the equations of motion was performed by the velocity Verlet algorithm. Total energy conservation of the MSINDO-MD procedure was tested. For an SCF convergence criteria of 10^{-8} a.u., the maximum deviation in the total energy was about 10^{-5} a.u. per pico second, which is normally expected from a Born-Oppenheimer MD procedure. The accuracy of the implementation was again verified by carrying out the simulated annealing of simple molecules like N_2 , H_2O , NH_3 , CH_4 and C_6H_6 . The optimized structures of these molecules from the simulated annealing and the quasi Newton Raphson optimizations were virtually the same. For the temperature control the Nosé-Hoover chain (NHC) thermostat was implemented. Integration of the equations of motion of the NHC thermostat was done by a reversible multiple time step algorithm. The total energy conservation and the average temperature in a canonical ensemble simulation of ZnS bulk shows that the NHC thermostat scheme was included correctly in MSINDO. The metadynamics technique was implemented in order to accelerate the escape from the free energy minima. The efficiency of metadynamics was illustrated by exploring the free energy surface of Si_7 cluster. After the successful testing of the MSINDO-MD code, it was employed for solving various problems in cluster, surface and solid state chemistry.

Simulated annealing of Si_n ($n=5-7$) clusters was performed. The obtained structures and relative energies of the various isomers are in agreement with results of density functional calculations. This demonstrates the accuracy of the parametrization for silicon compounds. In a study of the melting behavior of the Si_7 cluster, it was observed that the system undergoes structural transformation from a pentagonal bi-pyramid to a C_{2v} structure above 1600 K. This was monitored via the bond length fluctuation, mean square displacement, atomic distance and bond angle distributions. Using the simulated annealing technique it was found that a distorted cage-like structure with an Si_{17} core is the energy minimum structure for the Si_{45} cluster. The Si_{60} cluster prefers a compact bulk-like structure rather than fullerene-like cage or elongated structures. Various problems in surface chemistry were then considered. Static and dynamic calculations with MSINDO-CCM were used to identify possible structures of hydrated

vanadia species on different anatase surfaces. VO_4H_3 and $\text{V}_2\text{O}_7\text{H}_4$ molecules were adsorbed on the anatase (101), (001) and (100) surfaces and their stability at room temperature was studied using constant temperature MD simulations. The calculations show that vanadia species with divanadyl groups can exist on the anatase (101) surface. In the other energy minimum structures of VO_4H_3 on this surface, five-fold coordinated vanadium atoms with $\text{VO}(\text{OH})$ groups are present. The adsorption of VO_4H_3 results in the formation of an oxygen vacancy on the anatase (001) surface. The vanadate species has a distorted square pyramidal structure, similar to the VO_5 units in the vanadium pentoxide (001) surface. The stable structure of VO_4H_3 on the anatase (100) surface consists of a slightly distorted tetrahedron. Adsorption at the channels on the (100) surface was found to be unstable. The most stable structures obtained for the $\text{V}_2\text{O}_7\text{H}_4$ adsorption on the anatase surfaces contain V-O-V bonds. On the anatase (101) surface, the $\text{V}_2\text{O}_7\text{H}_4$ molecule prefers to form a continuation of the anatase crystal structure. Oxygen vacancies are not created on the (001) surface by the adsorption of a $\text{V}_2\text{O}_7\text{H}_4$ molecule. No vanadyl groups are present in the vanadia species on the anatase (001) surface. Thus $\text{V}_2\text{O}_7\text{H}_4$ on the anatase (001) surface might be less catalytically active than on the other surfaces. A slightly distorted tetrahedral structure is formed during the adsorption of $\text{V}_2\text{O}_7\text{H}_4$ on the (100) surface. Adsorptions at the edges or across the channels on the (100) surface are not thermodynamically favorable. Possible reactions of the surface hydroxyls with the adsorbed monomeric VO_4H_3 groups were also investigated. It was found that the preadsorbed surface hydroxyls are inert towards condensation reaction with hydrogen atoms of the adsorbed VO_4H_3 molecule on the (101) and (001) surfaces. On the (100) surface, proton transfer from the adsorbed VO_4H_3 molecule to the surface hydroxyls was found to occur under the experimental conditions. It was concluded that the hydrated polymeric chains formed on the (100) surface will have the form $(\text{VO}_4\text{H})_n$ under certain experimental conditions. The present investigations show that different surfaces of anatase are reacting differently with the vanadia particles. The topology of the surface determines the structure of the vanadia species after adsorption. In polycrystalline catalysts, all three anatase (101), (001) and (100) surfaces might be exposed and corresponding experiments observe an overall effect. The results obtained from the present calculations can explain various experimental observations.

The oxygen vacancy diffusion in rutile (110) surface was studied with the metadynamic techniques. The activation barrier for the oxygen vacancy migration from the first to the third atomic layer of the (110) surface was estimated to be 131 kJ/mol. Similarly, migration of the oxygen vacancy from the third to the fifth atomic layer was also simulated. The energy barrier for this process was about 181 kJ/mol. The migration of oxygen vacancies in the opposite direction, from the fifth to the third and then to the first atomic layers involves much smaller energy barriers (~ 50 kJ/mol). The time scale for these diffusion processes was estimated using the transition state theory. It was found that the diffusion of the oxygen vacancies from the surface to the bulk is not favorable even at high temperatures. On the other hand, the diffusion of oxygen vacancies from the bulk to the surface can occur at temperatures above 300 K in less than one second. Various experimental findings can be explained using the results obtained from these calculations.

Constant temperature MD simulations were used to calculate the vibrational density of states (VDOS) of the rutile-water adsorbate system. Isolated water molecules were found to adsorb dissociatively on both the rutile (110) and (100) surfaces. Similarly, for a monolayer water coverage, a complete dissociation of the water molecules was thermodynamically stable. The VDOS of undissociated water molecules in monolayer coverage was evaluated. The red-shift of the stretching frequency of O-H bonds was observed due the hydrogen bonding of the water molecules to the bridging oxygen atoms. The VDOS obtained for the fully dissociated monolayer coverage, show that bridging hydroxyl groups are hydrogen bonded to the oxygen atoms of the terminal hydroxyl groups. On the (100) surface, all the monolayer water molecules were dissociated into H and OH during the MD simulation at 100 K. In the vibrational spectrum obtained for the double layer water coverage on the (110) surface, where all the water molecules are molecularly adsorbed, the bending modes of water molecules in the first layer were found at lower wavenumbers (1625 cm^{-1}) compared to the second layer (1700 cm^{-1}). Vibrational features of the first layer water molecules were not affected by the adsorption of the second layer. It was also found from the VDOS that the interactions of the second layer water molecules with the bridging oxygen atoms are weak compared to the first layer water molecules. The VDOS for the water molecules adsorbed in double layer coverage on the rutile (100) surface with a complete dissociation of the first layer

water molecules show that the second layer water molecules are weakly connected to the surface. The results of this investigation are in reasonable agreement with the HREELS data from the literature.

The thermal entropic contribution to the free energy of mixing of ZnO and ZnS was estimated. Canonical ensemble simulations at 1000 K were performed for ZnO, ZnS, $\text{ZnO}_{0.98}\text{S}_{0.02}$ and $\text{ZnO}_{0.03}\text{S}_{0.97}$ bulk using the three-dimensional CCM. Entropy was calculated using a quantum-classical approach. The thermal entropic contributions to the free energy of mixing for $\text{ZnO}_{1-x}\text{S}_x$ with $x = 0.02$ and 0.97 were calculated. It was found that the thermal entropic contributions are not large enough to obtain negative free energy of mixing for ZnO and ZnS.

Appendix A

Analytical Derivatives of Collective Coordinates

The equation of motion (3.77) for the metadynamics contains an analytical derivative of a collective coordinate S_α with respect to the nuclear coordinates \mathbf{R}_I , $\nabla_{\mathbf{R}_I} S_\alpha(\mathbf{R}_I)$. Thus for a certain type of collective coordinate, its analytical derivatives have to be evaluated. The analytical derivatives of four different collective coordinates are given in this section.

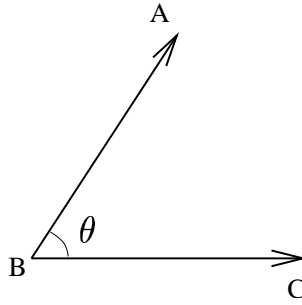
A.1 Bond Distances

If the collective coordinate S_α in (3.75) is defined as a bond distance R_{AB} between two atoms A and B, then its derivative with respect to the nuclear coordinate is given by

$$\nabla_{\mathbf{R}_I} S_\alpha(\mathbf{R}_I) = \nabla_{\mathbf{R}_I} R_{AB} = \begin{cases} -\mathbf{e}_{AB} & \text{if } I \text{ is atom A} \\ \mathbf{e}_{AB} & \text{if } I \text{ is atom B} \\ \mathbf{0} & \text{otherwise} \end{cases} \quad (\text{A.1})$$

where $\mathbf{e}_{AB} = \mathbf{R}_{AB}/R_{AB}$ and \mathbf{R}_{AB} is given by $\mathbf{R}_B - \mathbf{R}_A$.

A.2 Bond Angles



Let S_α is defined as θ , the angle between vectors \mathbf{R}_{BA} and \mathbf{R}_{BC} , where

$$\cos \theta = \mathbf{e}_{BA} \cdot \mathbf{e}_{BC}$$

where $\mathbf{e}_{BA} = \mathbf{R}_{BA}/R_{BA}$ and $\mathbf{e}_{BC} = \mathbf{R}_{BC}/R_{BC}$.

Therefore,

$$\nabla_{\mathbf{R}_I} S_\alpha(\mathbf{R}_I) = \nabla_{\mathbf{R}_I} \theta = -\frac{1}{\sin \theta} \nabla_{\mathbf{R}_I} (\mathbf{e}_{BA} \cdot \mathbf{e}_{BC}) \quad (\text{A.2})$$

But,

$$\nabla (\mathbf{K} \cdot \mathbf{L}) = (\mathbf{L} \cdot \nabla) \mathbf{K} + (\mathbf{K} \cdot \nabla) \mathbf{L} + \mathbf{L} \times (\nabla \times \mathbf{K}) + \mathbf{K} \times (\nabla \times \mathbf{L})$$

Thus (A.2) becomes

$$\begin{aligned} \nabla_{\mathbf{R}_I} \theta &= -\frac{1}{\sin \theta} \{ (\mathbf{e}_{BC} \cdot \nabla_{\mathbf{R}_I}) \mathbf{e}_{BA} + (\mathbf{e}_{BA} \cdot \nabla_{\mathbf{R}_I}) \mathbf{e}_{BC} + \mathbf{e}_{BC} \times (\nabla_{\mathbf{R}_I} \times \mathbf{e}_{BA}) \\ &\quad + \mathbf{e}_{BA} \times (\nabla_{\mathbf{R}_I} \times \mathbf{e}_{BC}) \} \end{aligned}$$

The last two terms in the right hand side of the above equation are zero.

Therefore, if I is atom A,

$$\nabla_{\mathbf{R}_A} \theta = \frac{-1}{R_{BA} \sin \theta} (\mathbf{e}_{BC} - \mathbf{e}_{BA} \cos \theta)$$

if I is atom B,

$$\nabla_{\mathbf{R}_B} \theta = \frac{1}{R_{BA} \sin \theta} (\mathbf{e}_{BC} - \mathbf{e}_{BA} \cos \theta) + \frac{1}{R_{BC} \sin \theta} (\mathbf{e}_{BA} - \mathbf{e}_{BC} \cos \theta)$$

if I is atom C,

$$\nabla_{\mathbf{R}_C} \theta = \frac{-1}{R_{BC} \sin \theta} (\mathbf{e}_{BA} - \mathbf{e}_{BC} \cos \theta)$$

and if $I \neq$ atom A, B or C,

$$\nabla_{\mathbf{R}_I} \theta = 0 \tag{A.3}$$

A.3 Dihedral Angles

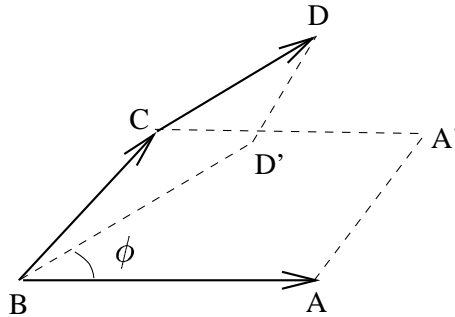


Figure A.61:

Let ϕ is the dihedral angle between the atoms A, B, C, and D. In other words, ϕ is the angle between normals $\hat{\mathbf{n}}_1$ and $\hat{\mathbf{n}}_2$ to the planes containing A, B, and C (ABCA') and B, C, and D (BCDD'), respectively (see Figure A.61). Therefore,

$$\cos \phi = \hat{\mathbf{n}}_1 \cdot \hat{\mathbf{n}}_2$$

where

$$\hat{\mathbf{n}}_1 = \frac{\mathbf{e}_{BA} \times \mathbf{e}_{BC}}{\sin \theta_1}$$

and

$$\hat{\mathbf{n}}_2 = \frac{\mathbf{e}_{CD} \times \mathbf{e}_{CB}}{\sin \theta_2}$$

Here θ_1 is the angle between the vectors \mathbf{R}_{BA} and \mathbf{R}_{BC} and θ_2 is the angle between the vectors \mathbf{R}_{CB} and \mathbf{R}_{CD} . Thus,

$$\cos \phi = \frac{(\mathbf{e}_{BA} \times \mathbf{e}_{BC}) \cdot (\mathbf{e}_{CD} \times \mathbf{e}_{CB})}{\sin \theta_1 \sin \theta_2}$$

Then,

$$\begin{aligned} \nabla_{\mathbf{R}_I} S_\alpha(\mathbf{R}_I) = \nabla_{\mathbf{R}_I} \phi &= -\frac{1}{\sin \phi} \left\{ \frac{1}{\sin \theta_1 \sin \theta_2} \nabla_{\mathbf{R}_I} [(\mathbf{e}_{BA} \times \mathbf{e}_{BC}) \cdot (\mathbf{e}_{CD} \times \mathbf{e}_{CB})] \right. \\ &\quad \left. + [(\mathbf{e}_{BA} \times \mathbf{e}_{BC}) \cdot (\mathbf{e}_{CD} \times \mathbf{e}_{CB})] \nabla_{\mathbf{R}_I} \left[\frac{1}{\sin \theta_1 \sin \theta_2} \right] \right\} \quad \text{A.4} \end{aligned}$$

But

$$\begin{aligned} (\mathbf{e}_{BA} \times \mathbf{e}_{BC}) \cdot (\mathbf{e}_{CD} \times \mathbf{e}_{CB}) &= (\mathbf{e}_{BA} \cdot \mathbf{e}_{CD})(\mathbf{e}_{BC} \cdot \mathbf{e}_{CB}) - (\mathbf{e}_{BA} \cdot \mathbf{e}_{CB})(\mathbf{e}_{BC} \cdot \mathbf{e}_{CD}) \\ &= -(\mathbf{e}_{BA} \cdot \mathbf{e}_{CD})(\mathbf{e}_{BC} \cdot \mathbf{e}_{BC}) - \cos \theta_1 \cos \theta_2 \\ &= -(\mathbf{e}_{BA} \cdot \mathbf{e}_{CD}) - \cos \theta_1 \cos \theta_2 \end{aligned}$$

Therefore

$$\begin{aligned} \nabla_{\mathbf{R}_I} \phi &= \frac{1}{\sin \phi \sin \theta_1 \sin \theta_2} \{ \nabla_{\mathbf{R}_I} (\mathbf{e}_{BA} \cdot \mathbf{e}_{CD}) \\ &\quad - \sin \theta_1 \cos \theta_2 (\nabla_{\mathbf{R}_I} \theta_1) - \sin \theta_2 \cos \theta_1 (\nabla_{\mathbf{R}_I} \theta_2) \\ &\quad - [\cot \theta_1 (\nabla_{\mathbf{R}_I} \theta_1) + \cot \theta_2 (\nabla_{\mathbf{R}_I} \theta_2)] [\cos \theta_1 \cos \theta_2 + (\mathbf{e}_{BA} \cdot \mathbf{e}_{CD})] \} \end{aligned}$$

In the above equation $\nabla_{\mathbf{R}_I} \theta_1$ and $\nabla_{\mathbf{R}_I} \theta_2$ are evaluated using (A.3). $\nabla_{\mathbf{R}_I} (\mathbf{e}_{BA} \cdot \mathbf{e}_{CD})$ is having the following solutions.

If I is atom A,

$$\nabla_{\mathbf{R}_A} (\mathbf{e}_{BA} \cdot \mathbf{e}_{CD}) = \frac{1}{R_{BA}} [\mathbf{e}_{CD} - (\mathbf{e}_{BA} \cdot \mathbf{e}_{CD}) \mathbf{e}_{BA}]$$

If I is atom B,

$$\nabla_{\mathbf{R}_B} (\mathbf{e}_{BA} \cdot \mathbf{e}_{CD}) = \frac{1}{R_{BA}} [-\mathbf{e}_{CD} + (\mathbf{e}_{BA} \cdot \mathbf{e}_{CD}) \mathbf{e}_{BA}]$$

If I is atom C,

$$\nabla_{\mathbf{R}_C} (\mathbf{e}_{BA} \cdot \mathbf{e}_{CD}) = \frac{1}{R_{CD}} [-\mathbf{e}_{BA} + (\mathbf{e}_{BA} \cdot \mathbf{e}_{CD}) \mathbf{e}_{CD}]$$

If I is atom D,

$$\nabla_{\mathbf{R}_D} (\mathbf{e}_{BA} \cdot \mathbf{e}_{CD}) = \frac{1}{R_{CD}} [\mathbf{e}_{BA} - (\mathbf{e}_{BA} \cdot \mathbf{e}_{CD}) \mathbf{e}_{CD}]$$

If $I \neq A, B, C$ or D

$$\nabla_{\mathbf{R}_I} (\mathbf{e}_{BA} \cdot \mathbf{e}_{CD}) = 0$$

A.4 Coordination Number

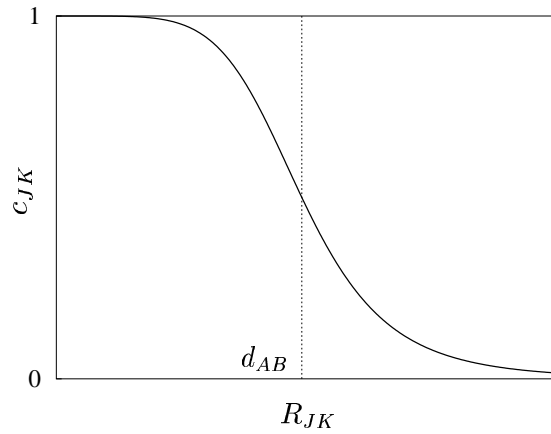


Figure A.62:

Coordination number C_{AB} between atoms of type A and B is defined using the expression [44],

$$C_{AB} = \sum_J \frac{N_A}{N_A} \sum_K \frac{N_B}{N_A} \frac{\left[1 - \left(\frac{R_{JK}}{d_{AB}}\right)^6\right]}{\left[1 - \left(\frac{R_{JK}}{d_{AB}}\right)^{12}\right]} = \sum_J \frac{N_A}{N_A} \sum_K c_{JK} \quad (\text{A.5})$$

where N_A and N_B are the number of atoms of type A and B , respectively and d_{AB} is the cut-off bond distance. Here,

$$c_{JK} = \frac{\left[1 - \left(\frac{R_{JK}}{d_{AB}}\right)^6\right]}{\left[1 - \left(\frac{R_{JK}}{d_{AB}}\right)^{12}\right]}$$

The function c_{JK} decays smoothly around d_{AB} (see Figure A.62).

For S_α as C_{AB} ,

$$\begin{aligned} \nabla_{\mathbf{R}_I} S_\alpha(\mathbf{R}_I) = \nabla_{\mathbf{R}_I} C_{AB}(\mathbf{R}_I) &= \sum_J^{N_A} \frac{1}{N_A} \sum_K^{N_B} \frac{6}{\left[1 - \left(\frac{R_{JK}}{d_{AB}}\right)^{12}\right] d_{AB}} \\ &\quad \left\{ 2 c_{JK} \left(\frac{R_{JK}}{d_{AB}}\right)^{11} - \left(\frac{R_{JK}}{d_{AB}}\right)^5 \right\} (\nabla_{\mathbf{R}_I} R_{JK}) \end{aligned}$$

The derivative $(\nabla_{\mathbf{R}_I} R_{JK})$ is evaluated using (A.1).

References

- [1] D. Frenkel, B. Smit, *Understanding Molecular Simulation - From Algorithms to Applications* (Academic Press, San Diego, 1996).
- [2] B. Ahlswede, K. Jug, *J. Comput. Chem.* **20**, 563 (1999).
- [3] I. N. Levine, *Quantum Chemistry* 5th ed. (Prentice Hall, New Jersey, 2000).
- [4] A. Szabo, N. S. Ostlund, *Modern Quantum Chemistry* (Dover Publications, New York, 1996).
- [5] C. C. J. Roothaan, *Rev. Mod. Phys.* **32**, 179 (1960).
- [6] J. A. Pople, R. K. Nesbet, *J. Chem. Phys.* **22**, 571 (1954).
- [7] D. N. Nanda, K. Jug, *Theor. Chim. Acta* **57**, 95 (1980).
- [8] J. A. Pople, D. L. Beveridge, P. A. Dobosh, *J. Chem. Phys.* **47**, 2026 (1967).
- [9] P.-O. Löwdin, *J. Chem. Phys.* **18**, 365 (1950).
- [10] J. Schulz, R. Iffert, K. Jug, *Int. J. Quantum Chem.* **27**, 461 (1985)
- [11] M. C. Zerner, *Mol. Phys.* **23**, 963 (1972).
- [12] R. S. Mulliken, *J. Chim. Phys.* **46**, 497 (1949).
- [13] K. Jug, G. Geudtner, T. Homann, *J. Comput. Chem.* **21**, 974 (2000).
- [14] T. Bredow, G. Geudtner, K. Jug, *J. Comput. Chem.* **22**, 861 (2001).
- [15] T. Bredow and K. Jug, MSINDO, in *Electronic Encyclopedia of Computational Chemistry*, Eds. P. von R. Schleyer, N. L. Allinger, T. Clark, J. Gasteiger, P. A. Kollman, H. F. Schaefer III, P. R. Schreiner (Wiley, Chichester, UK, 2004).
- [16] C. Pisani, F. Corá, R. Nada, R. Orlando, *Comput. Phys. Commun.* **82**, 139 (1994).
- [17] T. Bredow, G. Geudtner, K. Jug, *J. Comp. Chem.* **22**, 89 (2001).
- [18] F. Janetzko, R. A. Evarestov, T. Bredow, K. Jug, *phys. stat. soli. (b)* **241**, 1032 (2004).

-
- [19] T. Homann, T. Bredow, K. Jug, *Surf. Sci.* **555**, 135 (2004).
- [20] K. Jug, T. Homann, T. Bredow, *J. Phys. Chem. A* **108**, 2966 (2004).
- [21] J. Sauer, *Chem. Rev.* **89**, 199 (1989).
- [22] K. Jug, G. Geudtner, *Chem. Phys. Lett.* **208**, 537 (1993).
- [23] F. Janetzko, T. Bredow, K. Jug, *J. Chem. Phys.* **116**, 8994 (2002).
- [24] M. P. Allen, D. J. Tildesley, *Computer Simulation of Liquids* (Clarendon Press, Oxford, 1987).
- [25] J. M. Haile, *Molecular Dynamics Simulation* (Wiley-Interscience Publication, New York, 1992).
- [26] D. Marx, J. Hutter, *Ab Initio Molecular Dynamics: Theory and Implementation*, in *Modern Methods and Algorithms of Quantum Chemistry*, pp. 301-449, Editor : J. Grotendorst (John von Neumann Institute for Computing, Forschungszentrum Jülich 2000).
- [27] A. Warshel, M. Karplus, *Chem. Phys. Lett.* **32**, 11 (1975);
C. Leforestier, *J. Chem. Phys.* **68**, 4406 (1978).
- [28] R. Car, M. Parrinello, *Phys. Rev. Lett.* **55**, 2471 (1985).
- [29] W. F. van Gunsteren, H. J. C. Berendsen, *Mol. Phys.* **34**, 1311 (1977).
- [30] D. Chandler, *Introduction to Modern Statistical Mechanics* (Oxford University Press, New York 1987);
W. G. Hoover, *Computational Statistical Mechanics, Studies in Modern Thermodynamics 11* (Elsevier Science Publication, Amsterdam 1991);
R. E. Wilde, S. Singh, *Statistical Mechanics: Fundamentals and modern applications* (Wiley-Interscience Publication, New York, 1998).
- [31] W. H. Press, S. A. Teukolsky, W. T. Vetterling, B. P. Flannery, *Numerical Recipes in Fortran 77, Art of Scientific computing, Second Edition, Vol. 1*, (Cambridge University Press 1992).

-
- [32] D. A. McQuarrie, *Statistical Thermodynamics* (Harper and Row publishers, New York 1973).
- [33] P. H. Berens, D. H. J. Mackay, G. M. White, K. R. Wilson, *J. Chem. Phys.* **79**, 2375 (1983).
- [34] S.-T. Lin, M. Blanco, W. A. Goddard, *J. Chem. Phys.* **119**, 11792 (2003).
- [35] H. J. C. Berendsen, J. P. M. Postma, W. F. van Gunsteren, A. DiNola, J. R. Haak, *J. Chem. Phys.* **81**, 3684 (1984).
- [36] S. Kirkpatrick, C. D. Gelatt Jr., M. P. Vecchi, *Science* **220**, 671 (1983).
- [37] S. Nosé, *Mol. Phys.* **52**, 255 (1984).
- [38] S. Nosé, *J. Chem. Phys.* **81**, 511 (1984).
- [39] W. G. Hoover, *Phys. Rev. A* **34**, 2499 (1986).
- [40] G. J. Martyna, M. L. Klein, M. Tuckerman, *J. Chem. Phys.* **97**, 2635 (1992).
- [41] M. Tuckerman, B. J. Berne, G. J. Martyna, *J. Chem. Phys.* **97**, 1990 (1992).
- [42] G. J. Martyna, M. Tuckerman, D. J. Tobias, M. L. Klein, *Mol. Phys.* **87**, 1117 (1996).
- [43] A. Laio, M. Parrinello, *Proc. Natl. Acad. Sci. U. S. A.* **99**, 12562 (2002).
- [44] M. Iannuzzi, A. Laio, M. Parrinello, *Phys. Rev. Lett.* **90**, 238302 (2003).
- [45] G. Geudtner, Ph.D. thesis, University of Hannover, Germany, December 1995.
- [46] D. Fincham, *Comput. Phys. Commun.* **40**, 263 (1986).
- [47] K. Raghavachari, C. M. Rohlfing, *J. Chem. Phys.* **89**, 2219 (1988).
- [48] C. H. Patterson, R. P. Messmer, *Phys. Rev. B* **42**, 7530 (1990).
- [49] C. Zhao, K. Balasubramanian, *J. Chem. Phys.* **116**, 3690 (2002).
- [50] X. Zhu, X. C. Zeng, *J. Chem. Phys.* **118**, 3558 (2003).
- [51] B. Hartke, *Theor. Chem. Acc.* **99**, 241 (1998).

-
- [52] K. Jackson, M. R. Pederson, D. Porezag, Z. Hajnal, T. Frauenheim, Phys. Rev. B **55**, 2549 (1997).
- [53] C. Xiao, F. Hagelberg, W. A. Lester, Jr., Phys. Rev. B **66**, 075425 (2002).
- [54] K. Jug, M. Krack, Int. J. Quantum Chem. **44**, 517 (1992).
- [55] H. Kupka, K. Jug., Z. Phys. D **13**, 301 (1989).
- [56] D. Tománek, M. A. Schlüter, Phys. Rev. B **36**, 1208 (1987).
- [57] A. Sieck, D. Porezag, Th. Frauenheim, M. R. Pederson, K. Jackson, Phys. Rev. A **56**, 4890 (1997).
- [58] E. Kaxiras, K. Jackson, Phys. Rev. Lett. **71**, 727 (1993).
- [59] K. Jug, M. Krack, Chem. Phys. **173**, 439 (1993).
- [60] P. Ballone, W. Andreoni, R. Car, M. Parrinello, Phys. Rev. Lett. **60**, 271 (1988).
- [61] S. A. Maluendes, M. Dupuis, Int. J. Quantum Chem. **42**, 1327 (1992).
- [62] W. Andreoni, G. Pastore, Phys. Rev. B **41**, 10243 (1990).
- [63] L. Mitas, J. C. Grossman, I. Stich, J. Tobik, Phys. Rev. Lett. **84**, 1479 (2000).
- [64] R. S. Berry, in Clusters of Atoms and Molecules, Springer Series in Chemical Physics 52, 187, Ed. H. Haberland (Springer: Berlin-Heidelberg 1994).
- [65] P. T. Dinda, G. V. -Tsinganos, N. Flytzanis, A. D. Mistryotis, Phys. Rev. B **51**, 13697 (1995).
- [66] P. T. Dinda, G. V. -Tsinganos, N. Flytzanis, A. D. Mistryotis, Phys. Lett. A **191**, 339 (1994).
- [67] J. Wang, G. Wang, F. Ding, H. Lee, W. Shen, J. Zhao, Phys. Rev. B **341**, 529 (2001).
- [68] T. Mittelbach, H. -G. Fritsche, H. Müller, Z. Phys. Chem. **187**, 45 (1994).
- [69] E. Kaxiras, Phys. Rev. Lett. **64**, 551 (1990).

- [70] D. A. Jelski, B. Swift, T. T. Rantala, X. Xia, T. F. George, *J. Chem. Phys.* **95**, 8552 (1991).
- [71] D.W. Brenner, B. I. Dunlap, J. A. Harrison, J. W. Mintmire, R. C. Mowrey, D. H. Robertson, C. T. White, *Phys. Rev. B* **44**, 3479 (1991).
- [72] U. Röthlisberger, W. Andreoni, M. Parrinello, *Phys. Rev. Lett.* **72**, 665 (1994).
- [73] J. Pan, M. V. Ramakrishna, *Phys. Rev. B* **50**, 15431 (1994).
- [74] M. Menon, K. R. Subbaswamy, *Phys. Rev. B* **51**, 17952 (1995).
- [75] J. L. Elkind, J. M. Alford, F. D. Weiss, R. T. Laaksonen, R. E. Smalley, *J. Chem. Phys.* **87**, 2397 (1987).
- [76] C. Zybill, *Angew. Chem. Int. Ed. Engl.* **21**, 173 (1992).
- [77] S. Nagase, *Pure Appl. Chem.* **65**, 675 (1993).
- [78] M. C. Piqueras, R. Crespo, E. Orti, D. Tomás, *Chem. Phys. Lett.* **213**, 509 (1993).
- [79] Z. Slanina, S. -L. Lee, K. Kobayashi, S. Nagase, *J. Mol. Struct. (Theochem)* **312**, 175 (1994).
- [80] R. Crespo, M. C. Piqueras, F. Thomás, *Synth. Met.* **77**, 13 (1996).
- [81] J. Leszczynski and I. Yanov, *J. Phys. Chem. A* **103**, 396 (1999).
- [82] Y. L. Li, C. L. Luo, *Acta Physica Sinica* **51**, 2589 (2002).
- [83] B. X. Li, P. L. Cao, B. Song, Z. Z. Ye, *J. Mol. Struct. (Theochem)* **620**, 189 (2003).
- [84] B. X. Li, P. L. Cao, D. L. Que, *Phys. Rev. B* **61**, 1685 (2000).
- [85] F. S. Khan, J. Q. Broughton, *Phys. Rev. B* **43**, 11754 (1991).
- [86] M. Menon, K. R. Subbaswamy, *Chem. Phys. Lett.* **219**, 219 (1994).
- [87] Z. Chen, H. Jiao, G. Seifert, A.H.C. Horn, D. Yu, T. Clarkl W. Thiel, P.V.R. Schleyer, *J. Comput. Chem.* **24**, 948 (2003).

- [88] E. C. Honea, A. Ogura, C. A. Murray, K. Raghavachari, W. O. Sprenger, M. F. Jarrold, W. L. Brown, *Nature (London)* **366**, 42 (1993).
- [89] Q. Ran, R. W. Schmude, Jr., M. Miller, K. A. Gingerich, *Chem. Phys. Lett.* **230**, 337 (1994);
K. A. Gingerich, Q. Ran, R. W. Schmude, Jr., *Chem. Phys. Lett.* **256**, 274 (1996);
G. Meloni, K. A. Gingerich, *J. Chem. Phys.* **115**, 5470 (2001).
- [90] J. P. Perdew, K. Burke, and Y. Wang, *Phys. Rev. B* **54**, 16533 (1996).
- [91] M. J. Frisch, G. W. Trucks, H. B. Schlegel et al., *GAUSSIAN 98*, Gaussian, Inc., Pittsburgh, 1998.
- [92] J. C. Grossman, S. G. Louie, M. L. Cohen, *Phys. Rev. B* **60**, R6941 (1999).
- [93] V. E. Henrich, P. A. Cox, *The Surface Science of Metal Oxides* (Cambridge University Press, Cambridge, 1994).
- [94] J. G. Henry, G. W. Heinke, *Environmental Science and Engineering* (Prentice-Hall, Englewood Cliffs, NJ, 1989).
- [95] V. Nikolov, D. Klissurski, A. Anastasov, *Catal. Rev.-Sci. Eng.* **33**, 319 (1991);
H. K. Matralis, C. Papadopoulou, C. Kordulis, A. A. Elguezabal, V. C. Corberan, *Appl. Catal.* **126**, 365 (1995);
- [96] K. V. Narayana, A. Venugopal, K. S. R. Rao, S. K. Masthan, V. V. Rao, P. K. Rao, *Appl. Catal. A Gen.* **167**, 11 (1998).
- [97] A. Vejux, J. Courtine, *J. Solid State Chem.* **23**, 93 (1978).
- [98] M. Lazzeri, A. Vittadini, A. Selloni, *Phys. Rev. B* **63**, 155409 (2001).
- [99] A. Beltrán, J. R. Sambrano, M. Calatayud, F. R. Sensato, J. Andrés, *Surf. Sci.* **490**, 116 (2001).
- [100] P. M. Oliver, G. W. Watson, E. T. Kelsey, S. C. Parker, *J. Mater. Chem.* **7**, 563 (1997).
- [101] G. C. Bond, S. F. Tahir, *Appl. Catal.* **71**, 1 (1991).

- [102] G. C. Bond, *Appl. Catal. A Gen.* **157**, 91 (1997).
- [103] R. Y. Saleh, I. E. Wachs, S. S. Chan, C. C. Chersich, *J. Catal.* **98**, 102 (1986).
- [104] G. Busca, L. Marchetti, G. Centi, F. Trifiró, *J. Chem. Soc. Faraday Trans.* **81**, 1003 (1985).
- [105] G. Busca, *J. Raman Spectrosc.* **33**, 348 (2002).
- [106] L. G. Pinaeva, O. B. Lapina, V. M. Mastikhin, A. V. Nosov, B. S. Balzhinimaev, *J. Mol. Catal.* **88**, 311 (1994).
- [107] R. Kozłowski, R. F. Pettifer, J. M. Thomas, *J. Phys. Chem.* **87**, 5176 (1983).
- [108] G. Deo, I. E. Wachs, *J. Phys. Chem.* **95**, 5889 (1991).
- [109] D. C. Sayle, C. R. A. Catlow, M.-A. Perrin, P. Nortier, *J. Phys. Chem.* **100**, 8940 (1996).
- [110] M. L. Ferreira, M. Volpe, *J. Mol. Catal. A Chem.* **164**, 281 (2000).
- [111] M. Calatayud, B. Mguig, C. Minot, *Surf. Sci.* **526**, 297 (2003).
- [112] T. Bredow, T. Homann, K. Jug, *Res. Chem. Int.* **30**, 65 (2004).
- [113] T. Homann, T. Bredow, K. Jug, *Surf. Sci.* **555**, 135 (2004).
- [114] K. Jug, T. Homann, T. Bredow, *J. Phys. Chem. A* **108**, 2966 (2004).
- [115] U. Diebold, *Surf. Sci. Rep.* **48**, 53 (2003).
- [116] A. Fahmi, C. Minot, B. Silvi, M. Causá, *Phys. Rev. B* **47**, 11717 (1993).
- [117] C. J. Howard, T. M. Sabine, F. Dickson, *Acta Crystallogr. B* **47**, 462 (1991).
- [118] *CRC Handbook of Chemistry and Physics* 64th ed. (CRC, Boca Raton, FL, 1983).
- [119] R. Hengerer, B. Bolliger, M. Erbudak, M. Grätzel, *Surf. Sci.* **460**, 162 (2000).
- [120] G. S. Herman, Y. Gao, *Thin Solid Films* **397**, 157 (2001).

- [121] W. Hebenstreit, N. Ruzycki, G. S. Herman, Y. Gao, U. Diebold, *Phys. Rev. B* **64**, R16344 (2000).
- [122] G. S. Herman, M. R. Sievers, Y. Gao, *Phys. Rev. Lett.* **84**, 3354 (2000).
- [123] S. S. Chan, I. E. Wachs, L. L. Murrell, L. Wang, W. K. Hall, *J. Phys. Chem.* **88**, 5831 (1984).
- [124] G. Busca, G. Centi, L. Marchetti, F. Trifiró, *Langmuir* **2**, 568 (1986).
- [125] M. A. Larrubia, G. Busca, *Mater. Chem. Phys.* **72**, 337 (2001).
- [126] G. C. Bond, J. C. Vickerman, D. Johnson, M. Grätzel, J. Kiwi, R. Thampi, P. Albers, K. Seibold, *Catal. Today* **20**, 125 (1994).
- [127] J.-M. Herrmann, *Catal. Today* **20**, 135 (1994).
- [128] G. T. Went, L.-J. Leu, A. T. Bell, *J. Catal.* **134**, 479 (1992).
- [129] G. T. Went, L.-J. Leu, S. J. Lombardo, A. T. Bell, *J. Phys. Chem.* **96**, 2235 (1992).
- [130] T. Machej, J. Haber, A. M. Turek, I. E. Wachs, *Appl. Catal.* **70**, 115 (1991).
- [131] M. A. Vuurman, I. E. Wachs, A. M. Hirt, *J. Phys. Chem.* **95**, 9928 (1991).
- [132] C. Fernandez, M. Guelton, Ph. Bodart, M. Rigole, F. Lefebvre, *Catal. Today* **20**, 77 (1994).
- [133] D. A. Bulushev, L. K.-Minsker, F. Rainone, A. Renken, *J. Catal.* **205**, 115 (2002).
- [134] K. Morishige, F. Kanno, S. Ogawara, S. Sasaki, *J. Phys. Chem* **89**, 4404 (1985).
- [135] I. E. Wachs, G. Deo, M. A. Vuurman, H. Hu, D. S. Kim, J.-M. Jehng, *J. Mol. Catal.*, **82**, 443 (1993).
- [136] A. Vittadini, A. Selloni, F. P. Rotzinger, M. Grätzel, *Phys. Rev. Lett.* **81**, 2954 (1998).
- [137] A. Tilocca, A. Selloni, *J. Phys. Chem.* **119**, 7445 (2003).
- [138] A. Fahmi, C. Minot, *Surf. Sci.* **304**, 343 (1994).

- [139] T. Bredow, K. Jug, Surf. Sci. **327**, 398 (1995).
- [140] F. H. Jones, Surf. Sci. Rep. **42**, 75 (2001).
- [141] M. Ramamoorthy, D. Vanderbilt, R. D. King-Smith, Phys. Rev. B **49**, 16721 (1994).
- [142] C. Jech, R. Kelly, J. Phys. Chem. Solids **30** 465 (1969).
- [143] V. E. Henrich, G. Dresselhaus, H. J. Zeiger, Phys. Rev. Lett. **36**, 1335 (1976).
- [144] W. J. Lo, Y. W. Chung, G. A. Somorjai, Surf. Sci. **71** 199 (1978).
- [145] G. B. Hoflund, H. L. Yin, A. L. Grogan, Jr., D. A. Asbury, H. Yoneyama, O. Ikeda, H. Tamura, Langmuir **4**, 346 (1988).
- [146] H. Idriss, M. A. Barteau, Catal. Lett. **26**, 123 (1994).
- [147] V. S. Lusvardi, M. A. Barteau, J. G. Chen, J. Eng, Jr., B. Fruhberger, A. Teplyakov, Surf. Sci. **397**, 237 (1998).
- [148] M. A. Henderson, Surf. Sci. **419**, 174 (1999).
- [149] E. L. D. Hebenstreit, W. Hebenstreit, H. Geisler, C. A. Ventrice Jr., P. T. Sprunger, U. Diebold, Surf. Sci. **466**,
- [150] M. A. Hugenschmidt, L. Gamble, C. T. Campbell, Surf. Sci. **302**, 329 (1994).
- [151] J. A. Rodriguez, T. Jirsak, G. Liu, J. Hrbek, J. Dvorak, A. Maiti, J. Am. Chem. Soc. **123**, 9597 (2001).
- [152] O. B. Ajayi, L. E. Nagel, I. D. Raistrick, R. A. Huggins, J. Phys. Chem. Solids **37**, 167 (1976).
- [153] C. R. A. Catlow, R. James, Proc. R. Soc. London A **384**, 157 (1982).
- [154] G. J. Shen, L. A. Bursill, Proc. R. Soc. London A, **405**, 275 (1986).
- [155] M. Ramamoorthy, R. D. King-Smith, D. Vanderbilt, Phys. Rev. B **49**, 7709 (1994).
- [156] J. Purton, D. W. Bullet, P. M. Oliver, S. C. Parker, Surf. Sci. **336**, 166 (1995).

- [157] W. C. Mackrodt, E. -A. Simson, N. M. Harrison, *Surf. Sci.* **384**, 192 (1997).
- [158] P. J. D. Lindan, N. M. Harrison, M. J. Gillan, J. A. White, *Phys. Rev. B* **55**, 15919 (1997).
- [159] J. Chen, L.-B. Lin, F.-Q. Jing, *J. Phys. Chem. Solids* **62** 1257 (2001).
- [160] T. Bredow, G. Pacchioni, *Chem. Phys. Lett.* **355**, 417 (2002).
- [161] N. Yu, J. W. Halley, *Phys. Rev. B* **51**, 4768 (1995).
- [162] J. A. Rodriguez, J. Hrbek, Z. Chang, J. Dvorak, T. Jirsak, A. Maiti, *Phys. Rev. B* **65**, 235414 (2002).
- [163] E. P. Meagher, G. A. Lager, *Can. Mineral.* **17**, 77 (1979).
- [164] S. P. Bates, G. Kresse, M. J. Gillan, *Surf. Sci.* **385**, 386 (1997).
- [165] G. Charlton, P. B. Hoowes, C. L. Nicklin, P. Steadman, J. S. G. Taylor, C. A. Muryn, S. P. Harte, J. Mercer, R. McGrath, D. Norman, T. S. Turner, G. Thornton, *Phys. Rev. Lett.* **78**, 495 (1997).
- [166] J. Muscat, N. M. Harrison, G. Thornton, *Phys. Rev. B* **59**, 2320 (1999).
- [167] J. Muscat, N. M. Harrison, *Surf. Sci.* **446**, 119 (2000).
- [168] U. Diebold, J. Lehman, T. Mahmoud, M. Kuhn, G. Leonardelli, W. Hebenstriet, M. Schimd, P. Varga, *Surf. Sci.* **411**, 137 (1998).
- [169] M. A. Henderson, *Surf. Sci.* **400**, 203 (1998). L467 (2001).
- [170] P. A. Thiel, T. E. Madey, *Surf. Sci. Rep.* **7**, 211 (1987).
- [171] M. A. Henderson, *Surf. Sci. Rep.* **46**, 1 (2002).
- [172] M. Primet, P. Pichat, M.-V. Mathieu, *J. Phys. Chem.* **75**, 1221 (1971).
- [173] P. Jones, J. A. Hockney, *Trans. Faraday Soc.* **67**, 2669 (1971).
- [174] Y. Suda, T. Morimoto, *Langmuir* **3**, 786 (1987).

- [175] R. L. Kurtz, R. Stockbauer, T. E. Madey, E. Román, J. L. de Segovia, *Surf. Sci.* **218**, 178 (1989).
- [176] M. A. Henderson, *Surf. Sci.* **355**, 151 (1996).
- [177] R. Schaub, P. Thostrup, N. Lopez, E. Lægsgaard, I. Stensgaard, J. K. Nørskov, F. Besenbacher, *Phys. Rev. Lett.* **87**, 266104 (2001).
- [178] I. M. Brookes, C. A. Muryn, G. Thornton, *Phys. Rev. Lett.* **87**, 266103 (2001).
- [179] S. Bourgeois, F. Jomard, M. Perdereau, *Surf. Sci.* **279**, 349 (1992).
- [180] M. A. Henderson, *Langmuir* **12**, 5093 (1996).
- [181] J. Goniakowski, S. B.-Russo, C. Noguera, *Surf. Sci.* **284**, 315 (1993).
- [182] J. Goniakowski, M. J. Gillan, *Surf. Sci.* **350**, 145 (1996).
- [183] P. J. D. Lindan, N. M. Harrison, J. M. Holender, M. J. Gillan, *Chem. Phys. Lett.* **261**, 246 (1996).
- [184] J. Ahdjoudj, A. Markovits, C. Minot, *Catal. Today* **50**, 541 (1999).
- [185] E. V. Stefanovich, T. N. Troung, *Chem. Phys. Lett.* **299**, 623 (1999).
- [186] P. J. D. Lindan, N. M. Harrison, M. J. Gillan, *Phys. Rev. Lett.* **80**, 762 (1998).
- [187] W. Langel, *Surf. Sci.* **496**, 141 (2002).
- [188] C. Zhang, P. J. D. Lindan, *J. Chem. Phys.* **118**, 4620 (2003).
- [189] C. Zhang, P. J. D. Lindan, *J. Chem. Phys.* **119**, 9183 (2003).
- [190] U. Hotje, C. Rose, M. Binnewies, *Solid State Sci.* **5**, 1259 (2003).
- [191] D. Shen, S. Y. Au, G. Han, D. Que, N. Wang, I. K. Sou, *J. Mater. Sci. Lett.* **22**, 483 (2003).
- [192] Y.-Z. Yoo, Z.-W. Jin, T. Chikyow, T. Fukumura, K. Kawasaki, H. Koinuma, *Appl. Phys. Lett.* **81**, 3798 (2002).
- [193] M. Binnewies, S. Locmelis, to be published.

-
- [194] F. Janetzko, K. Jug, *J. Phys. Chem. A* **108**, 5449 (2004).
- [195] H. Schulz, K. H. Thiemann, *Solid State Commun.* **32**, 783 (1979).
- [196] K. Hümmer, *phys. stat. soli. (b)* **56**, 249 (1973).
- [197] W. M. Yim, E. J. Stofko, *J. Electrochem. Soc.: Solid-State Science Technology* **119**, 381 (1972).
- [198] D. Theis, *phys. stat. soli. (b)* **79**, 125 (1977).
- [199] M. Binnewies, E. Milke, *Thermodynamic Data of Elements and Compounds* (Wiley-VCH, Weinheim, 2002).

Curriculum Vitae

Nisanth Narayanan Nair

05. May 1979	Born in Kallara, Kerala, India
1984 - 1988	Bappuji High School, Koothattukulam, Kerala, India
1988 - 1991	DePaul High School, Thottuva, Kerala, India
1991 - 1994	S.M.V.N.S.S.H.S., Kallara, Kerala, India
1994 - 1996	M.G. University, Kottayam, Kerala, India Obtained the Pre-Degree
1996 - 1999	M.G. University, Kottayam, Kerala, India Obtained the Bachelor in Chemistry
1999 - 2001	Indian Institute of Technology, Madras, India Obtained the Master in Chemistry Worked with Prof. Dr. M. S. Gopinathan on the title “Dynamics of coupled van der Pol oscillators”
October 2001 -	Started Ph.D. in Institute for Theoretical Chemistry, University of Hannover under the supervision of Prof. Dr. K. Jug

Publication

1. N. N. Nair, T. Bredow, K. Jug,
Molecular Dynamics Implementation in MSINDO: Study of Silicon Clusters,
J. Comput. Chem. **25**, 1255-1263 (2004).